DESIGN AND STUDY OF SELF-ASSEMBLED FUNCTIONAL ORGANIC AND HYBRID SYSTEMS FOR BIOLOGICAL APPLICATIONS

THESIS SUBMITTED TO THE

COCHIN UNIVERSITY OF SCIENCE AND TECHNOLOGY

IN PARTIAL FULFILLMENT OF THE REQUIREMENTS FOR THE DEGREE OF

DOCTOR OF PHILOSOPHY IN CHEMISTRY

UNDER THE FACULTY OF SCIENCE

By

Dhanya T. J.

Under the Supervision of

Dr. D. Ramaiah

Photosciences and Photonics
Chemical Sciences and Technology Division
**CSIR-National Institute For Interdisciplinary
Science and Technology (CSIR-NIIST)**
Trivandrum 695019, Kerala

2014

Dedicated to my beloved Achan & Amma ….

DECLARATION

I hereby declare that the Ph. D. thesis entitled: "**DESIGN AND STUDY OF SELF-ASSEMBLED FUNCTIONAL ORGANIC AND HYBRID SYSTEMS FOR BIOLOGICAL APPLICATIONS**" is an independent work carried out by me at the Photosciences and Photonics Section, Chemical Sciences and Technology Division of the CSIR-National Institute for Interdisciplinary Science and Technology (CSIR-NIIST), Trivandrum, under the supervision of Dr. D. Ramaiah and the same has not been submitted elsewhere for a degree, diploma or title.

In keeping with the general practice of reporting scientific observations, due acknowledgement has been made wherever the work described is based on the findings of other investigators.
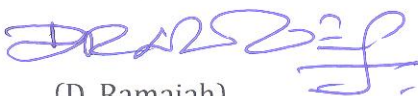
(DHANYA T. J.)

i

October 27, 2014

CERTIFICATE

This is to certify that the work embodied in the thesis entitled: "**DESIGN AND STUDY OF SELF-ASSEMBLED FUNCTIONAL ORGANIC AND HYBRID SYSTEMS FOR BIOLOGICAL APPLICATIONS**" has been carried out by Ms. Dhanya T. J. under my supervision and guidance at the Photosciences and Photonics Section, Chemical Sciences and Technology Division of the CSIR-National Institute for Interdisciplinary Science and Technology (CSIR-NIIST), Trivandrum and the same has not been submitted elsewhere for a degree. All the relevant corrections, modifications and recommendations suggested by the audience and the doctoral committee members during the pre-synopsis seminar of Ms. Dhanya T. J. have also been incorporated in the thesis.

(D. Ramaiah)

Thesis Supervisor

(*Formerly*, Head, Chemical Science and Technology Division CSIR-NIIST, Trivandrum)

ACKNOWLEDGEMENTS

CONTENTS

PREFACE

Molecular self-assembly is a key concept in supramolecular chemistry and which has been proven to be a reliable approach for the synthesis of nanomaterials for a variety of applications. The term self-assembly implies spontaneity, in which an ordered pattern forms itself from a disordered state, which is driven by non-covalent interactions (van der Waals, electrostatic, and hydrophobic interactions, hydrogen and coordination bonds). The focus of self-assembly as a strategy for the synthesis has been confined largely to molecules, because of the importance of manipulating the structure of matter at the molecular scale. It is believed that application of these simple and versatile molecular self-assembly systems will provide us with new opportunities to study some complex and unknown biological phenomena. The molecular engineering through design and self-assembly of biological building blocks is an enabling technology that will likely to play increasingly important role in the future technological applications. In this context, our efforts are to utilize the self-assembly of the proteins for the preparation of nano-bio conjugates and use of novel self-assembled functional organic chromophores for applications in biology and medicine. The present thesis has been divided into four chapters, of which the first chapter gives an overview of the recent developments in the molecular self-assembly with a particular emphasis on nanomaterials and their applications. The overall objectives of the thesis are also briefly described in this chapter.

The second chapter of the thesis describes the development of nano-biohybrid systems, using γ-globulin, a blood plasma protein as a capping, reducing as well as a

templating agent. The γ-globulin having amino and thio groups not only found to reduce the Au(III) ions, but also stabilize the nanoparticles. We have investigated the influence of temperature and pH, in addition to the concentration of the capping agent used for the formation of the nano-bio conjugates. For example, the formation of the narrower size distribution of the nanoparticles was observed with the increase in the concentration of the protein, which supports the fact that γ-globulin acts both as a controller of nucleation as well as stabiliser.

As analyzed through various photophysical, biophysical and microscopic techniques such as TEM, AFM, C-AFM, SEM, DLS, OPM, CD and FTIR, we observed that the initial photoactivation of γ-globulin at pH 12 for 3 h resulted in small protein fibres of *ca*. 20 ± 5 nm in size. Subsequently, these fibres found to assist in the alignment of the colloidal gold nanoparticles of average diameter of *ca*. 2-2.5 nm on the surface of the protein. At this particular irradiation time, the nano-bioconjugate thus formed exhibited negligible surface plasmon resonance absorption but showed an intense photoluminescence at 680 nm. Further irradiation for 24 h, led to the formation of self-assembled long fibres of the protein of *ca*. 2 ± 0.5 μm in diameter and *ca*. 18 μm in length. Interestingly, such a morphological transformation resulted in the sequential knock out of the anchored gold nanoparticles resulting in the clustering of the nanoparticles of size ca. 5-6 nm and observation of surface plasmon resonance band at around 520 nm with the concomitant quenching of luminescence intensity at 680 nm. The observation of light triggered self-assembly of the protein and its effect on controlling the fate of the anchored nanoparticles can be compared with the naturally

occurring process such as photomorphogenesis. Furthermore, our approach offers a way to understand the role played by the self-assembly of the protein in ordering and knock out of the metal nanoparticles and also in the design of nano-biohybrid materials for medicinal and optoelectronic applications.

Investigation of the potential applications of NIR absorbing and water soluble squaraine dyes **1-3** for protein labeling and anti-amyloid agents forms the subject matter of the third chapter of the thesis. These dyes showed good solubility in the aqueous medium and exhibited favorable photophysical properties. The study of their interactions with various proteins revealed that **1-3** showed unique interactions towards serum albumins as well as lysozyme. Detailed investigation of the lysozyme interactions indicated that this protein induces hypochromicity of *ca*. 69%, 71% and 49% in the absorption spectra as well as significant quenching in the fluorescence intensity of the dyes **1-3**, respectively. Half-reciprocal analysis of the absorption data and isothermal titration calorimetric (ITC) analysis of the titration experiments gave a 1:1 stoichiometry for the complexes formed between the lysozyme and squaraine dyes with association constants (K_{ass}) in the range 10^4-10^5 M^{-1}. We have determined the changes in the free energy (ΔG) for the complex formation and the values are found to be -30.78, -32.31 and -28.58 kJmol^{-1}, respectively for the dyes **1**, **2** and **3**. Furthermore, we have observed a strong induced CD (ICD) signal corresponding to the squaraine chromophore in the case of the halogenated squaraine dyes **2** and **3** at 636 and 637 nm confirming the complex formation in these cases. In contrast, the parent dye **1** showed negligible ICD in the presence of lysozyme indicating thereby its different mode of interaction. To understand the nature of interaction of the squaraine dyes **1-3** with

lysozyme, we have investigated the interaction of dyes **1-3** with different amino acids. These results indicated that the dyes **1-3** showed significant interactions with cysteine and glutamic acid which are present in the side chains of lysozyme. In addition the temperature dependent studies have revealed that the interaction of the dye and the lysozyme are irreversible.

Furthermore, we have investigated the interactions of these NIR dyes **1-3** with β-amyloid fibres derived from lysozyme to evaluate their potential as inhibitors of this biologically important protein aggregation. These β-amyloid fibrils were insoluble protein aggregates that have been associated with a range of neurodegenerative diseases, including Huntington, Alzheimer's, Parkinson's, and Creutzfeldt-Jakob diseases. We have synthesized amyloid fibres from lysozyme through its incubation in acidic solution below pH 4 and by allowing to form amyloid fibres at elevated temperature. We have monitored the changes in the absorption and emission spectra of the squaraine dyes **1-3** with the increasing addition of β-amyloid. The titration of the dye **1** with amyloid fibre resulted in *ca*. 74% hypochromicity, while with **2** and **3**, it showed *ca*. 76% and 68% hypochromicity, respectively, with a red shift of *ca*. ~23-28 nm. To quantify the binding affinities of the squaraine dyes **1-3** with β-amyloids, we have carried out the isothermal titration calorimetric (ITC) measurements. With increasing concentration of amyloid at 25 °C, we observed the enthalpy change associated with each injection and it was found to be exothermic in nature. The association constants were determined and are found to be 1.2×10^5, 3.6×10^5 and 3.2×10^5 M^{-1} for the dyes, **1-3**, respectively.

To gain more insights into the amyloid inhibiting nature of the squaraine dyes under investigations, we have carried out thioflavin assay, CD, isothermal titration calorimetry and microscopic analysis. The addition of the dyes **1**-**3** (5μM) led to the complete quenching in the apparent thioflavin fluorescence, thereby indicating the destabilization of β-amyloid fibres in the presence of the squaraine dyes. In addition, the circular dichroism studies have provided the direct evidence for the perturbation of the secondary structure of the amyloid structure and the conversion of its β-sheet rich structure to α-helical rich profile. Further, the inhibition of the amyloid fibres by the squaraine dyes **1**-**3**, has been evidenced though the DLS, TEM AFM and SAED, wherein we observed the complete destabilization of the amyloid fibre and transformation of the fibre into spherical particles of *ca*. 350 nm in the presence of **1**-**3**. These results demonstrate the fact that the squaraine dyes **1**-**3** can act as protein labeling agents as well as the inhibitors of the protein amyloidogenesis.

The last chapter of the thesis describes the synthesis and investigation of self-assembly as well as bio-imaging aspects of a few novel tetraphenylethene conjugates **4**-**6**. These conjugates consist of tetraphenylethene (TPE) as the electron donor (D) and benzothiazole core as the electron acceptor (A) unit. These systems showed two absorption bands in the region 320-335 nm and 425-450 nm, wherein the first band can be attributed to the characteristic absorption of the TPE chromophore, while the latter to the intramolecular charge transfer (ICT) band. Expectedly, these conjugates showed significant solvatochromism and exhibited a hypsochromic shift (negative

solvatochromism) as the solvent polarity increased, and these observations were justified though theoretical studies employing the B3LYP/6-31g* method.

We have investigated the self-assembly properties of these D-A conjugates though variation in the percentage of water in acetonitrile solution due to the formation of nanoaggregates. We have observed a prominent enhancement in the fluorescence intensity, when the water fraction (f_w) was increased to *ca*. 70%, 50% and 95% in acetonitrile solutions of **4**, **5** and **6**, respectively. The time-resolved fluorescence studies of the conjugates by varying the percentage of water f_w in acetonitrile solution showed a double exponential decay. The major component (91%) with enhanced lifetime of 5.66 ns, was attributed to the aggregated species. The short lived component (9%) was with a lifetime of 1.4 ns, which corresponds to the monomeric state. With a view to understand the nature of the self-assemblies formed, we have carried out the temperature and timedependent studies as well as varied ionic strength of the medium. From these experiments, it was clear that the assemblies formed were J-type and were thermodynamically stable. Further the contour map of the observed fluorescence intensity as a function of the fluorescence excitation and emission wavelength confirmed the formation of J-type aggregates in these cases.

To have a better understanding of the type of self-assemblies formed from the TPE conjugates **4**-**6**, we have carried out the morphological analysis through various microscopic techniques such as DLS, SEM and TEM. In the case of the conjugate **4**, when the water fraction was raised to *ca*. 70%, we observed rod shape architectures having ~ 780 nm in diameter and ~ 12 μM in length as evidenced through TEM and SEM analysis.

We have made similar observations with the dodecyl conjugate **5** at *ca*. 50% water fraction in acetonitrile solution. In contrast, the non-alkylated conjugate **6** showed nanoflower architectures at *ca*. 95% water/acetonitrile mixture. On further increasing the water percentage to *ca*. 99%, the self-assembled nanostructures of the conjugates **4-6** were found to be destabilized to give rise to the nanoparticles (NPs) of average size ~10 nm. To gain more understanding of the formation of the nanoarchitectures with the change in the percentage of water fraction, we have carried out electron diffraction (ED) studies. These studies have revealed that at *ca*. 70% and 50% water/acetonitrile mixtures, the aggregates formed from **4** and **5** were found to be highly crystalline and such structures were transformed to amorphous nature as the water fraction was increased to 99%.

To evaluate the potential of the conjugate as bio-imaging agents, we have carried out their *in vitro* cytotoxicity and cellular uptake studies though MTT assay, flow cytometric and confocal laser scanning microscopic techniques. PC-3 human prostate cancer cells were chosen as model cells to demonstrate the ability of these TPE derivatives for *in vitro* cell tracing applications. Evidently, from the concentration dependent MTT studies we have observed that the nanoparticles derived from TPE conjugates **4-6** were found to be nontoxic upto 50 μM concentrations for **4** and **6** while **5** showed the cytocompatible nature upto 25 μM. Through the timedependent flow cytometric analysis with these TPE-NPs we have observed that almost *ca*. 98% labeling of this cell lines within 5 min of incubation at 5 μM concentration. In addition the 3D analysis of the CLSM image confirmed the cell internalization of NPs. The nanoparticles

of these systems were found to have unique cellular uptake and were found to be localized within the cellular cytoplasm. Thus nanoparticle of these conjugates which exhibited efficient emission, large stoke shift, good stability, biocompatibility and excellent cellular imaging properties can have potential applications for tracking cells as well as in cell-based therapies.

In summary we have synthesized novel functional organic chromophores and have studied systematic investigation of self-assembly of these synthetic and biological building blocks under a variety of conditions. These nano-biohybrid systems were synthesized using γ-globulin, a blood plasma protein, wherein the protein acts as a capping, reducing as well as a templating agent. The investigation of interaction of water soluble NIR squaraine dyes with lysozyme indicates that these dyes can act as the protein labeling agents and the efficiency of inhibition of β-amyloid indicate, thereby their potential as anti-amyloid agents. Finally, the novel D-A systems based on tetraphenylethene and benzothiazole exhibited interesting photophysical and self-assembling properties. Thus nanoparticles of these conjugates exhibited superior stability, fluorescence efficiency and good biocompatibility in the aqueous media thereby their potential as cell tracing and imaging applications.

Note: The numbers of various compounds given here correspond to those given under the respective Chapters.

MOLECULAR SELF-ASSEMBLY: ITS VERSATILITY AND APPLICATIONS
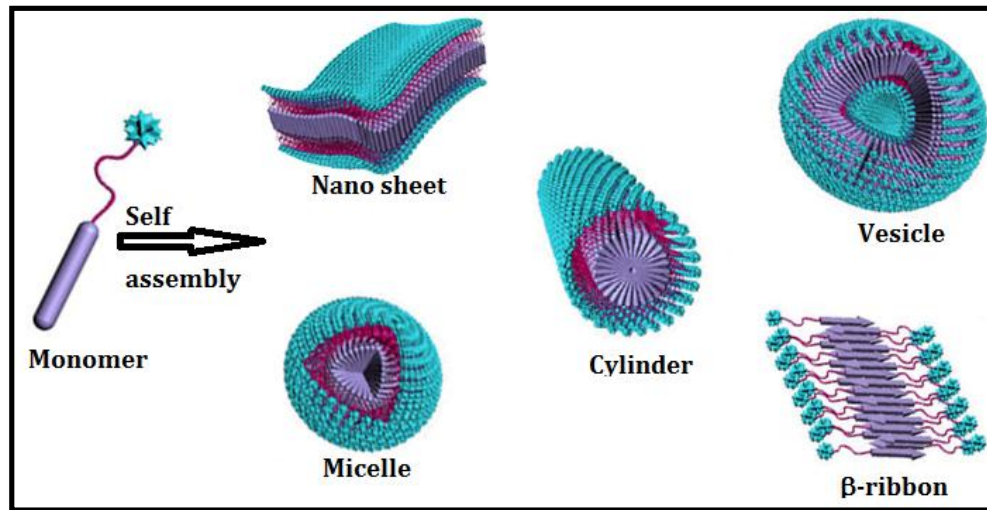
1.1. INTRODUCTION

Molecular self-assembly is the assembly of molecules in to an organized structure with the aid of multiple intermolecular forces including relatively weak non-covalent interactions, such as hydrogen bonding, π-π stacking, electrostatic, van der Waals, coordination and ion-dipole interactions.[1,2] On a molecular scale, the accurate and controlled application of intermolecular forces can lead to new and previously unachievable nanostructures. Hence, the molecular self-assembly is a highly topical and promising field of research in nanotechnology today. With many complex examples in nature, the molecular self-assembly is a widely observed phenomenon that

is yet to be fully understood. Nature's power to efficiently create diverse complex biological functions is based on the non-covalent interactions of covalently pre-fabricated building blocks including bilayered lipid liposomes, protein tertiary structures, DNA double helices, as well as the complex biological process. The molecular self-assembly is ubiquitous in nature and has recently emerged as a new approach in chemical synthesis, nanotechnology, polymer science, materials and engineering. The most illustrative and best understood examples of the molecular self-assembled structures occurring in nature are the tobacco mosaic virus and the formation of collagen (Figure 1.1).
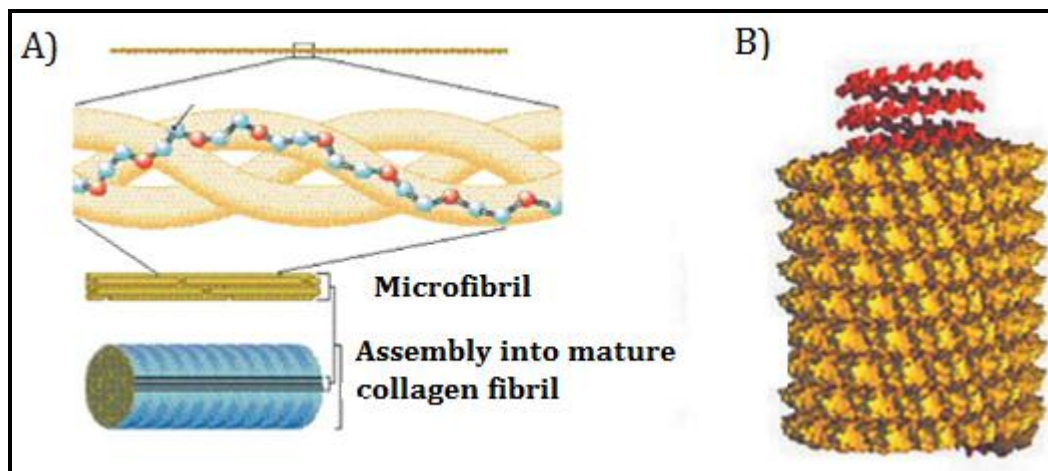
Figure 1.1. A) Hierarchical self-assembly of collagen. B) Schematic structure of the tobacco mosaic virus. [Adapted from the reference 3].

Through the molecular self-assembly it is possible to create a new class of materials at the molecular level. The functional hybrid materials based on this approach are very important from the fundamental as well as technology view points. For example, the non-covalently prepared combinations of organic and

inorganic systems have been of central role to the design of a variety of hybrid materials useful for optoelectronic and biological applications.[2] The optical and morphological properties of these soft materials eventually depend on how these molecules are packed in the assemblies. The self-assembled architectures engineered from organic/ polymer/ biomolecules construct the novel hybrid materials with enhanced thermal, optical, electronic, and mechanical properties. In this chapter, an overview of the recent developments in the field of self-assembled functional materials is presented with a particular emphasis on nanostructures and their applications. Furthermore, the objectives of the present thesis are also briefly described in this chapter.

1.2. SELF-ASSEMBLY PHENOMENON

The self-assembly is a key tool in supramolecular chemistry in which the term 'assembly' connotes 'to put together' and the 'self' implies 'without outside help or on its own'.[1,2] The self-assembly can occur with components from the molecular to planetary scale with the aid of different kinds of interactions provided that appropriate conditions are met. The molecular self-assembly systems lie at the interface between molecular biology, chemistry, polymer science, materials science and engineering.[2,3] The molecular self-assembly has proven to be a reliable approach based on multiple weak intermolecular forces leading to the creation of large, discrete, ordered structures from the relatively simple units. The formation of molecular crystals,[4] colloids,[5] lipid bilayers, and self-assembled monolayers[6] are all

examples of the molecular self-assembly. It is believed that application of these simple and versatile molecular self-assembly systems will provide us with new opportunities to study some complex and previously unknown biological phenomenon.

The molecular engineering through molecular design and self-assembly of the biological building blocks is an enabling technology that will likely to play an increasingly important role in the future technology. This chapter primarily focuses on the recent progress of the molecular self-assembly that is inspired from naturally occurring materials, peptide self-assemblies and also based on synthetic molecules or amphiphiles bearing bioactive moieties. These larger systems also offer a level of control over the characteristics of the components and interactions among them that makes fundamental investigations especially tractable. In this context, the self-assembly of living systems is most important. The astonishing range of complex structures present in the cells offer countless examples of the functional self-assembly.[3] The molecular self-assembly provides routes to a range of ordered structures for example molecular crystals,[4] liquid crystals,[5] semicrystalline[5] and phase-separated polymers.[6] And it is providing one of the general strategies for generating the ensembles of nanostructures. Finally, there is great potential for its use in smart materials, non-fouling properties, electrochemistry, protein binding, DNA assembly, corrosion resistance, biological arrays, cell interactions, and molecular electronics.[7] Thus, the self-assembly is important in a variety of fields including chemistry, physics, biology, materials science and nanoscience.

1.2.1 Types of Self-Assemblies

The term self-assembly implies spontaneity, in which an ordered pattern forms itself from a disordered state. There are mainly two kinds of self-assemblies, *viz*., static (S) and dynamic (D).[8] The static self-assembly denotes a process in which ordered structures are formed when the system reaches an energy minimum and do not dissipate energy. Classic examples are structured block copolymers,[9,10] nanoparticles,[11,12] nanorods,[13] liquid crystals,[14] and hierarchical supramolecular systems.[15] In dynamic self-assembly (D) (Table 1.1), the interactions responsible for the formation of structures or patterns between components only occur if the system is dissipating energy. The components in dynamic self-assembling systems interact with one another in complex (and often nonlinear) ways and their behavior will often be complex.

Among these, the study of dynamic self-assembly is in its infancy while the static type has found various applications. The processes of static and dynamic self-assemblies can be sub-divided into two further variants, templated and biological self-assembly. In a templated self-assembly (T), the interactions between the components and regular features in their environment determine the structures that form. Some examples include, crystallization on the surface, which determine the morphology of the crystal as well as crystallization of colloids in three-dimensional optical fields.[16-18] Thus the biological self-assembly has emerged over times as a hybrid methodology and the characteristic of the biological self-assembly (B) is the variety and complexity of the functions that it produces due to the organization.

Table 1.1. Examples of static (S), dynamic (D), template (T), and biological (B) self assemblies.

Systems	Type	Applications
Atomic, ionic, and molecular crystals	S	Materials, optoelectronics
Phase-separated and ionic layered polymers	S	
Self-assembled monolayers (SAMs)	S/T	Microfabrication, nanoelectronics, sensors
Lipid bilayers and lipid films	S	Biomembranes, emulsions
Liquid crystals	S	Displays
Colloidal crystals	S	Band gap materials, molecular sieves
Macro- and mesoscopic structures	S/D/T	Electronic circuits
Fluidic self-assembly	S/T	Microfabrication
Oscillating and reaction-diffusion reactions	D	Biological oscillations
Bacterial colonies	D/B	

Of the diverse approaches reported for the molecular self-assembly, two strategies have received significant attention. These include, electrostatic self-assembly (or layer-by-layer assembly) and "self-assembled monolayers" (SAMs). The electrostatic self-assembly involves the alternate adsorption of anionic and cationic electrolytes onto a suitable substrate, whereas for SAMs, the basic building blocks (that is, the constituent molecules), and weaker intermolecular bonds such as

van der Waals bonds were utilized to synthesize a defined structure. Figure 1.2 shows the representative examples of dynamic and static self-assembly.
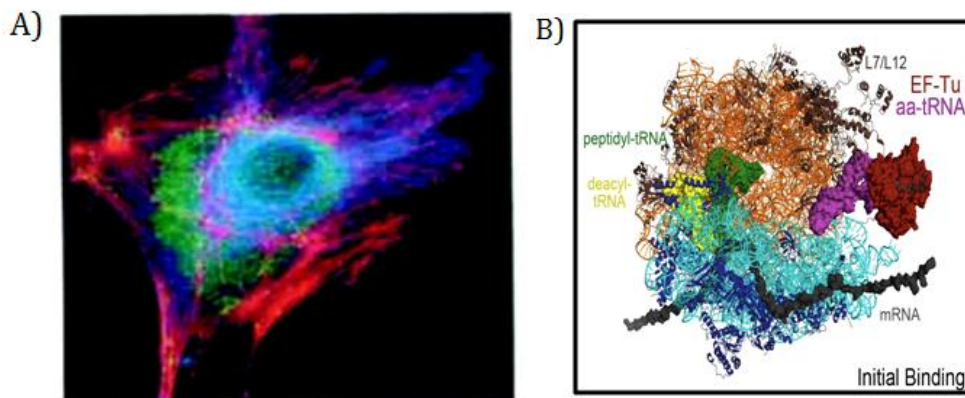
Figure 1.2. Examples of A) dynamic self-assembly, an optical micrograph of a cell with fluorescently labeled cytoskeleton and nucleus and B) static self-assembly, crystal structure of a ribosome. [Adapted from the reference 8].

1.2.2. Non-Covalent Interactions in Self-Assembly

The self-assembly is a process in which components, either separated or linked, which spontaneously form ordered structures. The characteristic properties such as shape, surface, charge, polarizability, magnetic dipole, mass, etc of the individual components determine the interactions among them. The design of components that organize themselves into desired patterns is the key to applications of the self-assembly.[19] In the self-assembly of larger components (meso or macroscopic objects), the interactions can often be selected and tailored, and can include gravitational attraction, external electromagnetic fields, and magnetic, capillary, and entropic interactions, which are not important in the case of the

molecules. The molecular self-assembly involves the non-covalent interactions such as van der Waals, electrostatic, hydrophobic interactions, hydrogen and coordinate bonds. While a covalent bond normally has a homolytic bond dissociation energy that ranges between 100 and 400 kJ mol^{-1}, the non-covalent interactions are generally weak and vary from less than 5 kJ mol^{-1} for van der Waals forces, to approximately 50 kJ mol^{-1} for hydrogen bonding and 250 kJ mol^{-1} for Coulomb interactions (Table 1.2). Our ability to predict the structural features from combinations of such interactions in the self-assembled materials is still in its early stage and, most of the learning is done in retrospect that is, after the discovery of structures and their functions.

Because the self-assembly requires that the components be mobile, it usually takes place in fluid phases or on smooth surfaces. The environment can modify the interactions between the components and the equilibration is usually required to reach the ordered structures. The self-assembly requires that the components either equilibrate between aggregated and non-aggregated states, or adjust their positions relative to one another in an organized state.[8] There are three ranges of sizes of components for which self-assembly is important: molecular, nanoscale (colloids, nanowires, nanospheres, and related structures), and meso to macroscopic (objects with dimensions from microns to centimeters). The rules for self-assembly in each of these ranges are similar but not identical. The new types of self-assembled structures, especially those with potential for application in microelectronics,[20,21] photonics,[22,23] near field optics[24] and the emerging field of nanoscience[25,26] have

gained technological importance.[27-34] In the following headings, we describe the nanostructures that are formed from the self-assembly of various molecular systems as well as their properties and applications.

Table 1.2. Bond energies in kJ mol^{-1} of non-covalent interactions.[2c]

Type of interaction or bonding	Strength (kJ mol^{-1})
Covalent bond	100-400
Coulomb	250
Hydrogen bond	10-65
Ion-dipole	50-200
Dipole-dipole	5-50
π-π	0-50
van der Waals forces	<5
Hydrophobic effects	difficult to assess
Metal-ligand	0-400

1.2.3. Self-Assembly of Peptides and Proteins

The ability of peptides and proteins to adopt specific secondary, tertiary and quaternary structures provides unique opportunities for the design of nanoscale materials.[34] The covalently linked amino acids with specific sequence give rise to

peptides, which can undergo distinctive self-assembly[34-37] and exhibit recognition function.[37,38] Depending on the conformation and stereochemical configuration of the constituent amino acids, these peptides exhibit different structures, such as α-helices and β-sheets. A number of peptide molecular self-assembly systems have been designed and developed. Their systematic analysis has provided insights into the chemical and structural principles of peptide self-assembly, which are simple to design and easy to synthesize. This class of biological materials has considerable potential for a number of applications, including scaffolding for tissue repair and tissue engineering, drug delivery, and biological surface engineering.

The first engineered structures at the nano-scale were the cyclic peptide nanotubes **1**, which were developed by Ghadiri and co-workers (Chart 1.1).[39a] In their elegant work, the concepts of natural peptides were translated into technological applications. The authors have used the concept of alternating D- and L-amino acids in the context of a cyclic peptide to form a planar ring that could be self-assembled, one on top of the other, to form tubular structures of a desired diameter. Another cyclic peptide that was shown to self-assemble into tubular structures is the lanreotide (**2**) growth hormone inhibitor reported by Valery and co-workers (Chart 1.1).[39b] Importantly, this naturally occurring cyclic peptide self-assembled into well-ordered structures at the nano-scale through hydrophobic and aromatic interactions. Similar systems have also been described where these peptide systems exhibited self-assembly to form a gel with regular β-sheet tapes of well-defined structures.[39-42] The self-assembly of peptide nanotubes, which allowed
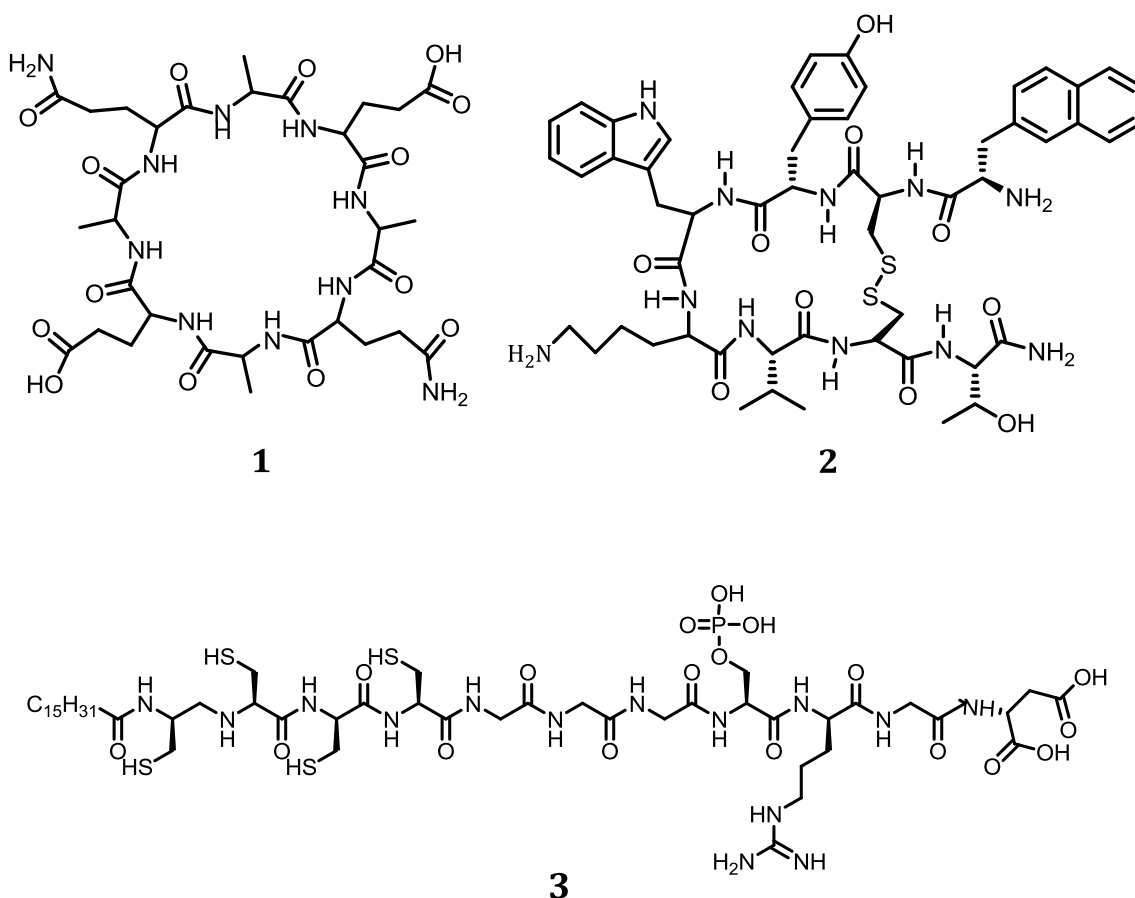
Chart 1.1

ions to pass through and to insert themselves into lipid bilayer membranes were also described.[42] The peptide-amphiphiles (PA), which were attached with hydrophobic tails were found to self-assemble into highly organized nanostructures, which can in principle promote cell adhesion, spreading, migration, growth and differentiation.[43-47] For example, Stupp and co-workers have synthesized a peptide amphiphile (PA) **3**, consisting of different functionalities (Chart 1.1).[48] Upon acidification of the solution, PA spontaneously aggregated into birefringent hydrogels. The cryo-TEM studies have revealed a network of fibers with a diameter

of ~7.6 nm and lengths up to several micrometers. Furthermore, a number of fascinating bio-mimetic peptide and protein structures have been reported in the literature, which exhibited helical coils and di-, tri-, and tetra-helical bundles.[49]

The protein-protein interactions play an important role in metabolic and degradation processes and in the self-assembling of large biological structures.[50] The self-assembly in biology was popularized by the cross-fibril formation, also known as formation of amyloids.[51] There were about 20 different human diseases that are associated with the formation of these 7-10 nm amyloid fibrils. These fibrils show remarkable order, as indicated by X-ray fibre diffraction at 4.6-4.8 Å. They also exhibit a typical β-sheet conformation and strong interactions with thioflavin.[52,53] The cross-fibre consists of peptide chains that align perpendicular to the fibril axis as shown in Figure 1.3.[51] Basically, the amyloid fibres were a bundle of highly
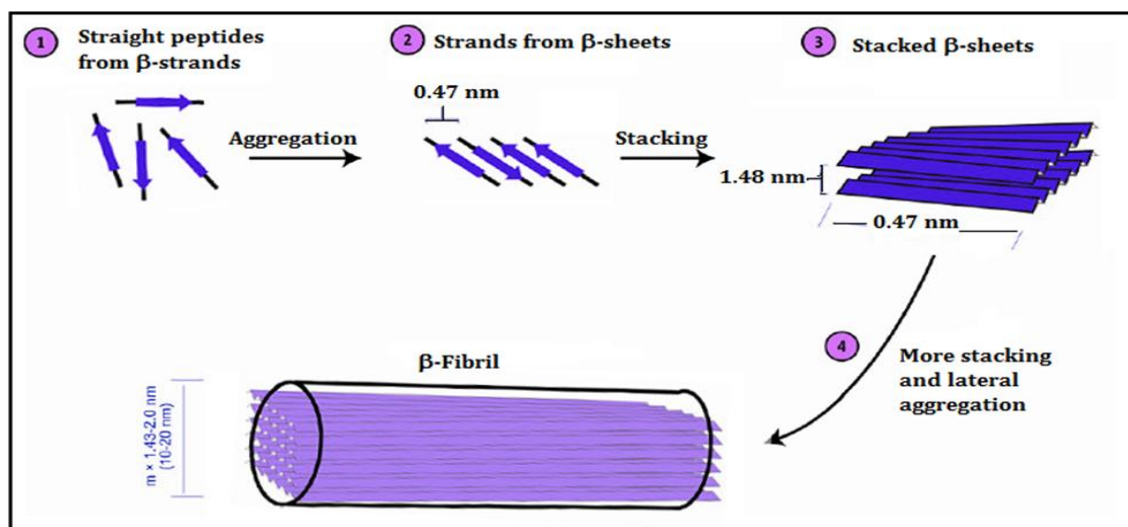
Figure 1.3. Schematic representation of the cross beta structure perpendicular to fibril axis [Adapted from the reference 51].

ordered filaments composed of ladders of β-strands that run perpendicular to the fibre axis and are arranged in hydrogen-bonded β-sheets.[52] The ability to construct biocompatible peptide-based molecular architectures with anisotropic shapes should expand the possibilities for the design of molecular machines for diverse applications in biological and materials science.

Another class of peptide nanostructures was based on the use of short aromatic peptides to form well-ordered nanostructures. The simpler analogues, diphenylalanine (**4**) and diphenylglycine (**5**) peptides, form nanotube and nanospherical structures in the aqueous solution (Figure 1.4).[54a] Other end-termini analogs such as the Fmoc-diphenylalanine forms macroscopic hydrogels with nano-scale order,[54b] whereas the Fmoc-diphenylalanine exhibited fibrils that were very
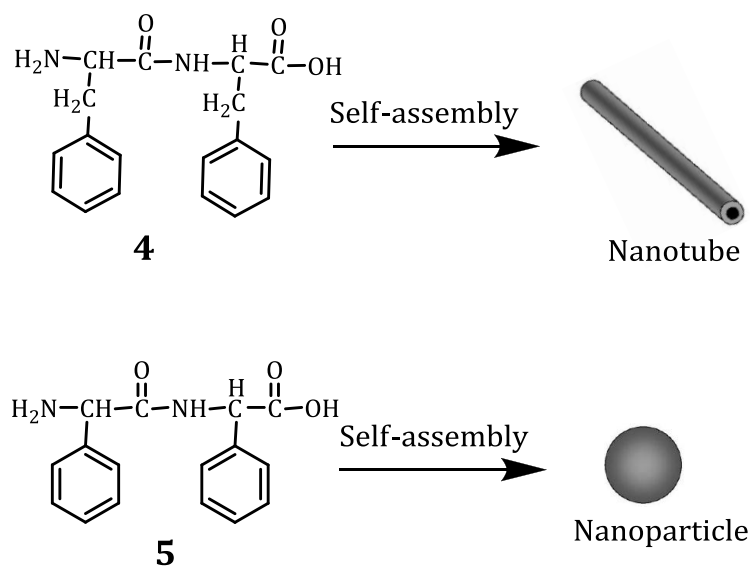
Figure 1.4. Formation of ordered nanostructures by simple aromatic dipeptides, **4** and **5**.

similar to the amyloid fibrils.[54] It was demonstrated that the dipeptide nanostructures were formed by vertical arrays in the form of a "nano-forest" of tubes or could be aligned horizontally upon modification with either magnetic nanoparticles or by the application of an external magnetic field.[54]

1.2.4. Self-Assembly of Polymers and Small Organic Molecules

Over the past decades, the molecular self-assembly has become a powerful tool for making functional and self-assembled organic nanostructures. In 1990s, Whiteside and co-workers have pioneered the concept of self-assembly of nanoscale structures.[54] Similarly, Stupp and co-workers have developed the concept of self-assembly of the functional bulk materials.[55] The influence of the self-assembly strategies in polymeric materials research was reflected in the strong interest on the organization of well-defined block copolymers into defined superlattices and patterns.[56] Most notably the exciting new field of supramolecular polymers[57] was based on the control of non-covalent interactions among monomers and processes of self-assembly to generate ordered 1D structures. In organic nanoscience, the supramolecular chemistry is key in the design of self-assembled monolayers,[58] and nanostructures with diverse shapes and dimensionalities.[59-61] In all these cases, the programmed self-assembly of the π-conjugated oligomers has been achieved using supramolecular design rules.

One of the first examples of the self-assembly of the supramolecular material was reported by the Stupp's group in the form of nanostructure lattices.[55] In 1997, a

triblock molecule labeled as a rod-coil was reported to assemble into mushroom like objects that were fairly monodisperse. Inspired by this earlier work on rod-coil molecules that self-assemble into non-centrosymmetric nanostructures,[55] the authors have designed another molecule **6** (Chart 1.2) with a dendritic block at the end of the rod segment that they refered to as a dendron rod-coil. These molecules assembled into 1D ribbons that were of ~10 nm wide and ~2 nm thickness. Later, synthetically modifying each of the dendron, rod, and coil segments revealed the importance of each portion on the self-assembly behavior.[55c] Around the same time, complementary approaches to 1D nanostructures with potential electronic function have also been proposed.[56]
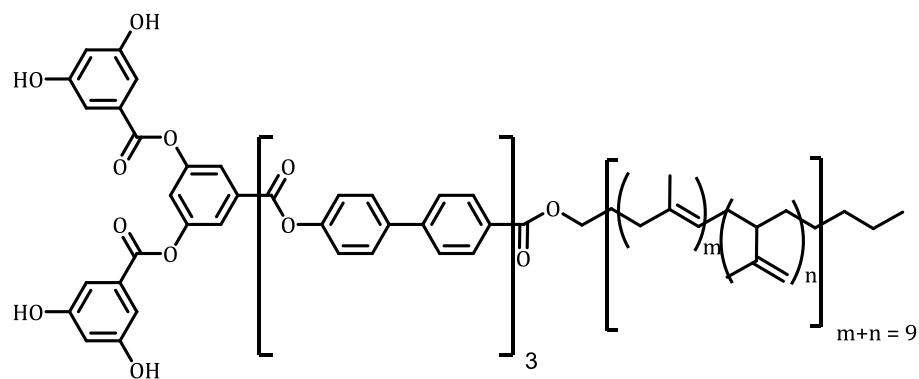
6

Chart 1.2

For example, Meijer's group found that molecules functionalized at each end with ureidopyrimidinones **7** (Chart 1.3), assemble through self-complementary hydrogen bonding into supramolecular polymers that display effective mechanical properties similar to the covalent polymers at room temperatures.[56] This structures
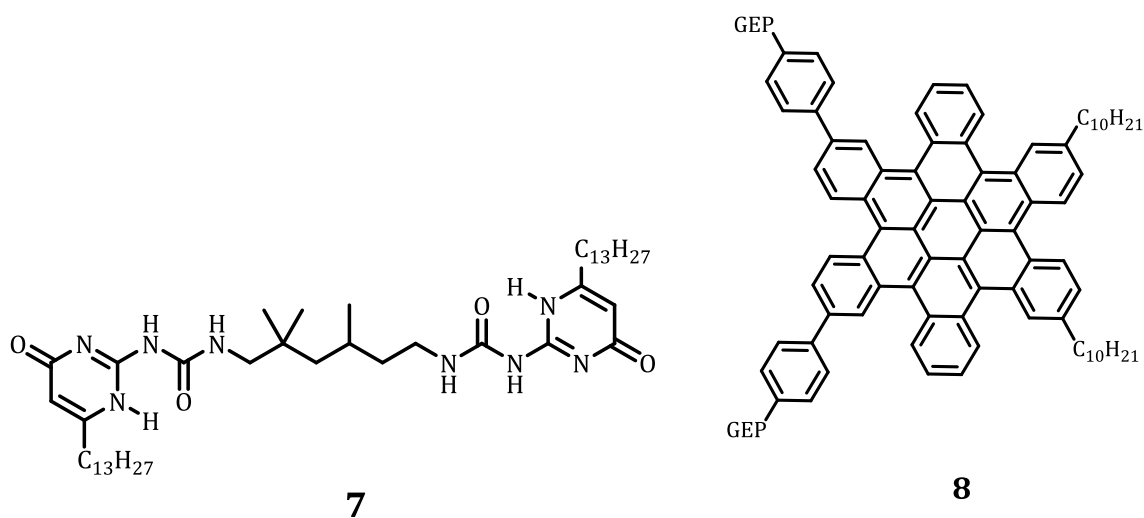
Chart 1.3

were also incorporated with conjugated aromatic oligo(phenylene vinylene) groups to form different nanoarchitectures.[56b,c] Importantly, 1D structures have been reported based on disk-shaped aromatics like hexabenzocoronene, which exhibited strong π-π stacking interactions and required no additional interactions for the assembly.[57] For example, Hill and co-workers have reported hexabenzocoronene **8** (Chart 1.3), with ethylene glycol tails on one side and alkyl tails on the other. These systems exhibited self-assembly to form a hollow tube.[57] A solution of these graphitic tubes can be drawn into macroscopic fibers with anisotropic conductivity along the fiber's long axis. This family of molecularly engineered graphite with a one-dimensional tubular shape and a chemically accessible surface constitutes an important step towards molecular electronics.[57]

Recently, Stupp and co-workers have reported a hairpin-shaped molecule based on thiophene-capped diketopyrrolopyrrole units and the self-assembly motif

trans-diamidocyclohexane **9** (Chart 1.4).[58] The authors have demonstrated that the self-assembly of **9** involving hydrogen bonding and π–π stacking interactions, led to long supramolecular electron donor nanowires. The authors have observed that the stepwise cooling process with minimal stirring of solutions was necessary to create robust wires through the self-assembly process.

Würthner and co-workers have also shown a strong pathway dependence in hairpin-shaped molecules bearing merocyanine dyes **10** (Chart 1.5).[59] Accordingly, the authors have described the kinetically controlled self-assembly of merocyanine **10** into helical nanorods. A series of bis(merocyanine) dyes bearing alkyl substituents of different chain lengths and branching revealed that the small structural changes of the monomeric building block can have a considerable impact on the stability and structure of the nano structures formed. In addition, porphyrins, phthalocyanines, and perylenes were also investigated as molecular materials that possess unique electronic, magnetic and photophysical properties. These systems formed highly ordered aggregates with interesting morphology in solution such as micelles, vesicles, sheets, rods, tapes etc. For example, Wang[62] and co-workers have reported nanotubes from the porphyrin derivative **11**. This system exhibited the self-assembly in the aqueous solution involving ionic interactions (Chart 1.5).

Perylene bisimides (PBI) are one of the well studied classes of dyes for optoelectronic applications because of their promising optical properties such as the strong absorption in the visible range, high fluorescence quantum yields as well as their high stability towards photooxidation. Shinkai and co-workers[63] have reported
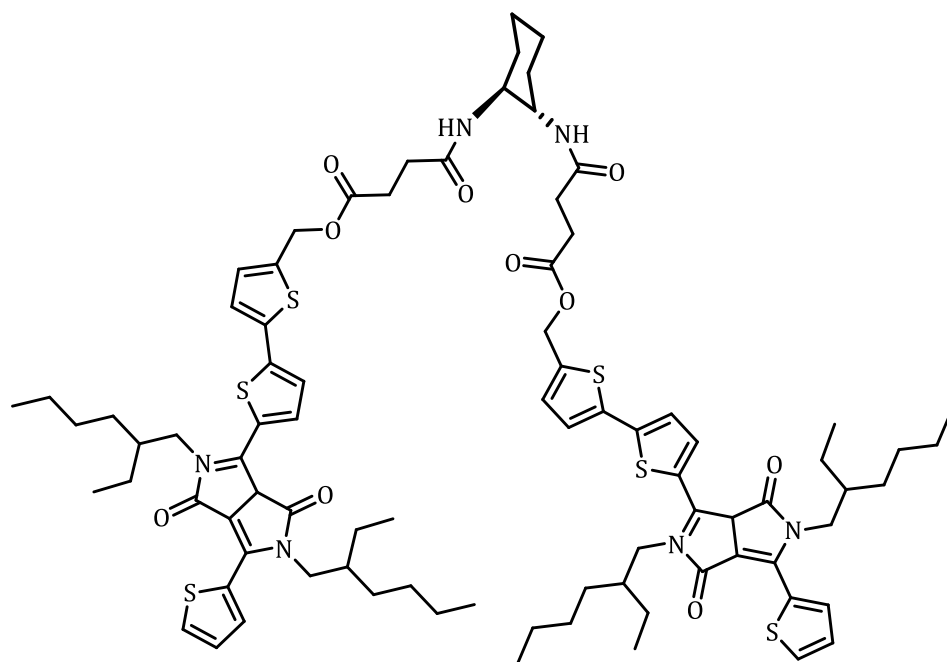
9

Chart 1.4
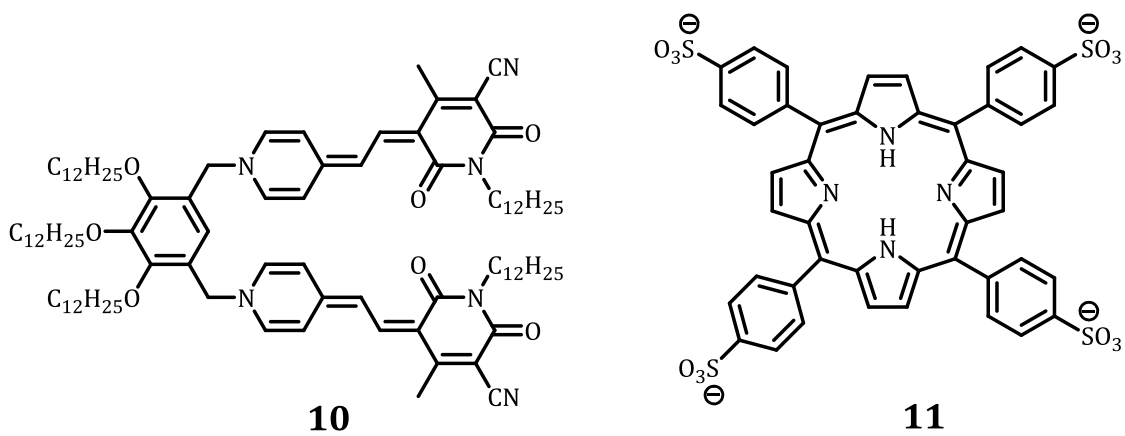
10

11

Chart 1.5

the first cholesterol functionalized perylene bisimide organogelator **12** (Chart 1.6), which exhibited cascade of energy and electron transfer processes.[63] SEM studies have suggested the formation of well-defined fibrous aggregates through π-π stacking and intermolecular hydrogen bonding between the constituent PBI molecules. The gelator also showed efficient electron transfer in organic solar cells upon mixing with p-type organic semiconductors. The authors have demonstrated that a new visible light-harvesting system that can be designed utilizing a superstructure created in an organogel medium. These nano-materials based on molecular assemblies can be applied as model systems for light-emitting diodes, signal amplifiers, fluorescence sensors, energy filters, and other photonic devices.

12

13
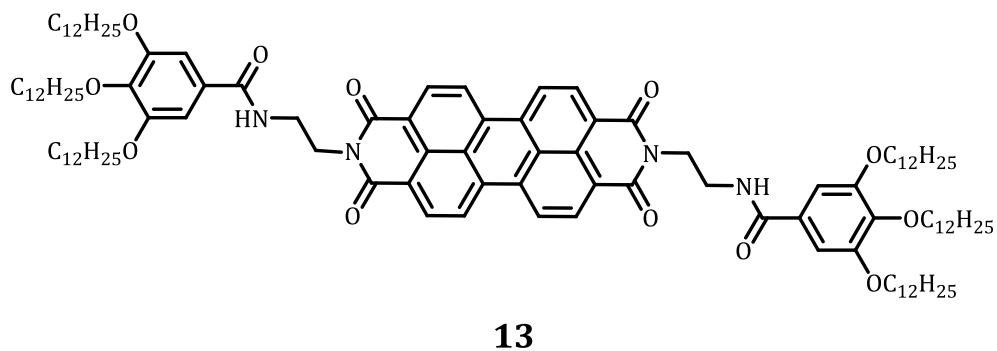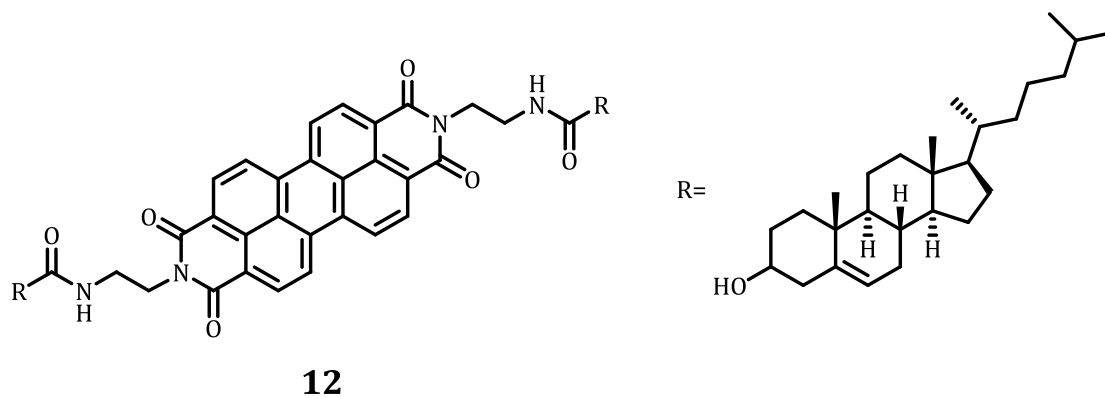
Chart 1.6

In another work, Würthner and co-workers have employed the perylene bisimide dye **13** (Chart 1.6), which exhibited gelation in a broad variety of organic solvents to afford well-defined nano and mesoscopic helical fibres and bundles.[64] Such well-organized fibers and bundles were composed of extended π-stacks of the electron poor dye **13**, which can have application as mobile n-type charge carriers. Shinkai and co-workers have reported the gelation of naphthalene diimide, **14** (Chart 1.7). The UV-vis absorption spectra of these derivatives showed charge-transfer band at 600 nm upon adding increasing amounts of the dihydroxy-naphathalene (**15**) in the gel matrix of **14**.[65] SEM analysis showed the presence of long 1D fibrous networks of **14**, which transformed into a 2D sheet like structure by the addition of **15**.

14   **15**
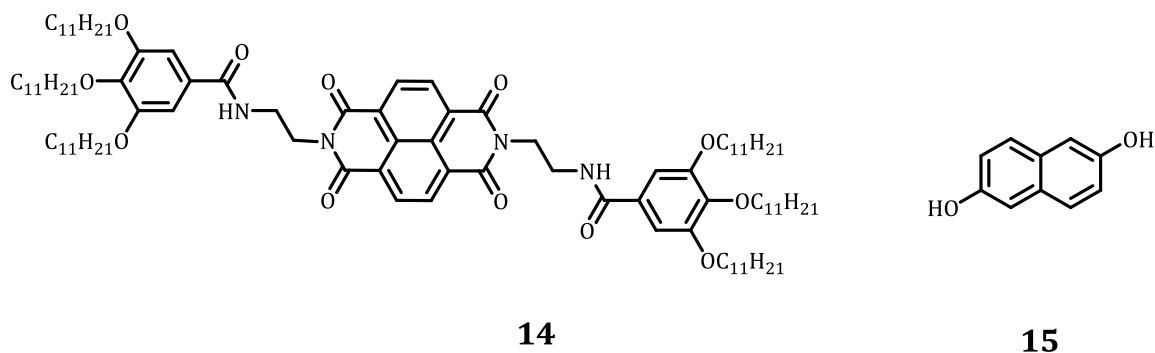
Chart 1.7

1.3. APPLICATION OF SELF-ASSEMBLED STRUCTURES

The self-assembly paradigm in chemistry, physics and biology has emerged scientifically over the past two decades to a point of sophistication that one can

begin to exploit its numerous attributes in nanofabrication. The self-assembled nanostructures are interesting because they offer new properties like conductivity and stiffness, and the broad range of fluorescent emission of CdSe quantum dots. These structures form bridge between classical and biological branches of materials science, and thereby "materials-by-design". The nanomaterials can, in principle, be made using both top-down and bottom-up techniques. The self-assembly involving these two techniques allows materials to be designed with hierarchical order and complexity that mimics those seen in the biological systems.

Nanotechnology based device in its broadest terms refers to a device with dimensions in the range of 1 to 100 nm, while the nanofabrication involves the manipulation of matter at the nanoscopic length scale to provide by design structures and patterns with purposeful function.[1b] In the framework of nanofabrication by bottom-up synthetic chemistry, the self-assembly has provided a powerful way of making materials and organizing them into functional constructs designed for a specific purpose. The self-assembly, as a fundamental building principle, teaches that the matter of all kinds, exemplified by atoms and molecules, colloids and polymers, can undergo spontaneous organization to a higher level of structural complexity, driven by a map of forces operating over multiple length scales.[1b] With unique sequence-specific self-assembly and recognition properties, the peptides and proteins play critical roles in controlling the biomineralization of inorganic nanostructures in natural systems. These properties render them particularly useful molecules for the fabrication of new materials and devices.[66]

In this context, substantial effort has been devoted to organizing nanoparticles (NPs) in one, two and three dimensions. The ability to create NP networks, arrays and composites, however, depends on our ability to fully understand and control the assembly process of these materials. Incorporation of both "bottom-up" (e.g., self-assembly) and "top-down" techniques (e.g., lithography) in patterning and controlling spatial assembly of NPs and their composites is a growing field of research. The synergy between these two approaches provides new directions for the creation of functional materials and devices.[67] Of all the nanomaterials, gold based nanomaterials have attracted particular interest owing to their ease of synthesis and functionalization, chemical stability, low inherent toxicity (biocompatibility), and tuneable optical and electronic properties (absorption, fluorescence and conductivity).[68] A number of efforts have been made in the field of biopolymer (proteins and DNA) mediated assembly of gold NPs (AuNPs) as well as their applications in sensors and devices (Figure 1.5).[67] The protein or peptide scaffold in AuNP-protein composites can serve three purposes like assembling the NPs into composite material, serving as a matrix that induces ordering and anisotropic orientation in clusters and on surfaces, and acting as a functional element (e.g. possess an electronic property).

The assembly of inorganic nanoparticles using self-assembled peptide scaffolds generally involves several independent steps including peptide assembly, nanoparticle synthesis, nanoparticle functionalization with surface ligands suitable for interacting with the peptide-based template, and finally mixture of the template
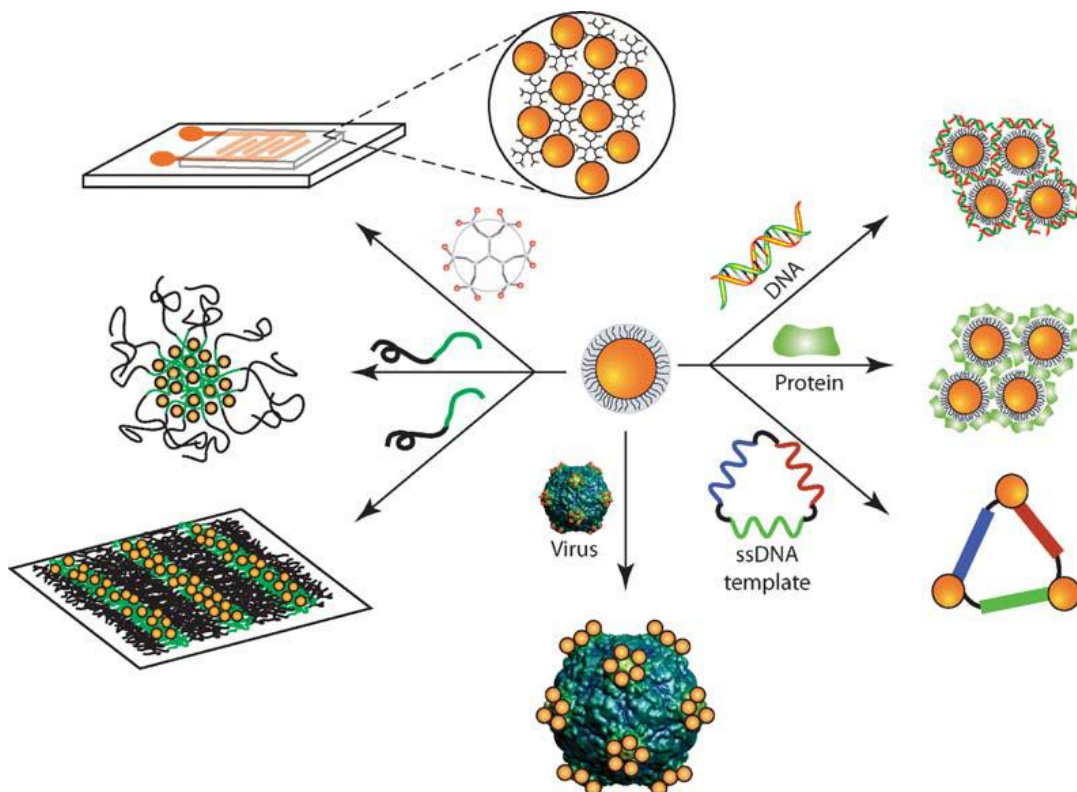
Figure 1.5. Different types of biomolecule templated assembly of AuNPs. [Adapted from reference 67].

structures with the functionalized nanoparticles to effect assembly of the nanoparticles. Pochan and co-workers have prepared sheets of gold nanoparticles (Figure 1.6), in which the assembled, non-twisted laminated β-sheet peptide fibrils acted as templates, and negatively charged gold nanoparticles intercalated within the fibril laminates. The formation of the aggregates was induced by the electrostatic interactions with the positively charged lysine side chains of the fibrils and negatively charged nanoparticles. The intercalation of gold nanoparticles was enhanced when the the interfilament spacing increased from 2.5 nm to 3.9 nm.[68]
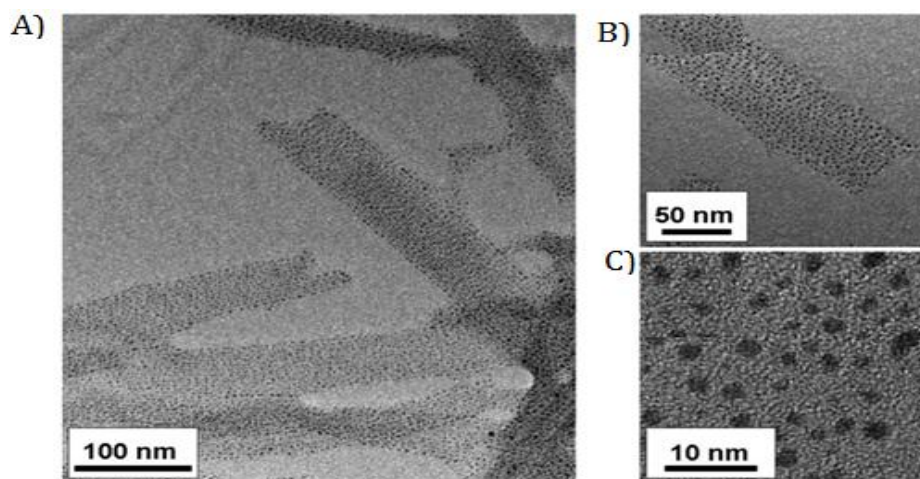
Figure 1.6. A) Bright-field transmission electron microscopy (BF-TEM) image showing peptide fibril-gold nanoparticle assemblies, B) BF-TEM showing aligned gold nanoparticle arrays, and C) High resolution TEM showing size dispersity of gold nanoparticles immobilized within the peptide fibril template. [Adapted from reference 68].

Rosi and co-workers have demonstrated that both the peptide self-assembly and peptide-based biomineralization of gold nanoparticles could be combined into one process.[69] The authors have first selected the water-soluble peptide AYSSGAPPMPPF, which had been identified by Naik *et al.*, and was known to bind to both gold and silver surfaces. Moreover, this peptide was able to mineralize chloroauric acid to form monodisperse spherical gold nanoparticles in the presence of HEPES buffer.[70] The authors have observed that the self-assembly process and the Au-based biomineralization of gold nanoparticles were successfully coupled into one simultaneous process to form structurally complex and highly ordered left handed double helices of gold nanoparticles.[69]

Hutchinson and co-workers have demonstrated the use of DNA scaffolds to pattern closely spaced gold nanoparticle assemblies of lines, ribbons and junctions on surfaces (Figure 1.7). The nanoparticles thus formed close-packed linear assemblies along the DNA scaffold and showed extended linear structures that often reached nearly 1 μm in length. Furthermore, two-dimensional, ribbon-like structures were also observed, resulting from the cross-linking of DNA scaffolds by the polyvalent gold nanoparticles.[71]
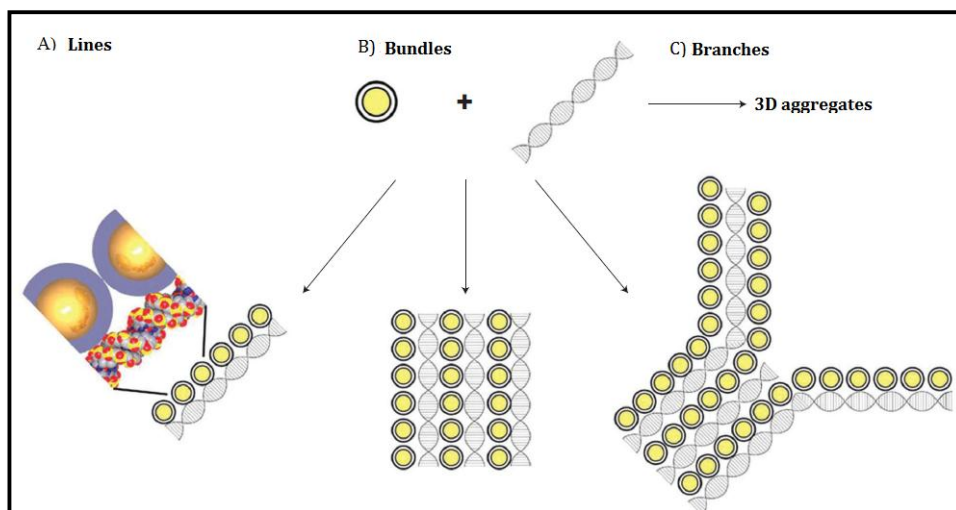
Figure 1.7. Nanoassemblies of gold nanoparticles formed during solution phase assembly. Electrostatic assembly of cationic nanoparticles onto the anionic backbone of DNA produces a wide range of structures including A) linear arrays, B) ribbons, and C) branched assemblies. [Adapted from reference 71].

Encapsulation of noble-metal nanoparticles within dielectric matrices has been used to develop fast optoelectric response systems near the surface plasmon resonance (SPR) frequency.[72] The light energy can thus be transported through nanoparticles whose sizes were substantially smaller than the wavelength of

corresponding light.[73] Paik *et al.*, have successfully constructed anisotropic AuNP chains within a dielectric protein matrix capable of exhibiting photoconductivity near the SPR frequency by taking advantage of molecular propensity of α-synuclein to form the protein fibrillar suprastructures (Figure 1.8).[74] Their strategy employed a facile unit assembly procedure of novel self-interactive building blocks made of amyloidogenic α-synuclein encapsulating AuNPs to construct the high-order nanostructures, representing a typical bottom-up approach to fabricate a functional large structures of noble-metal nanoparticles.
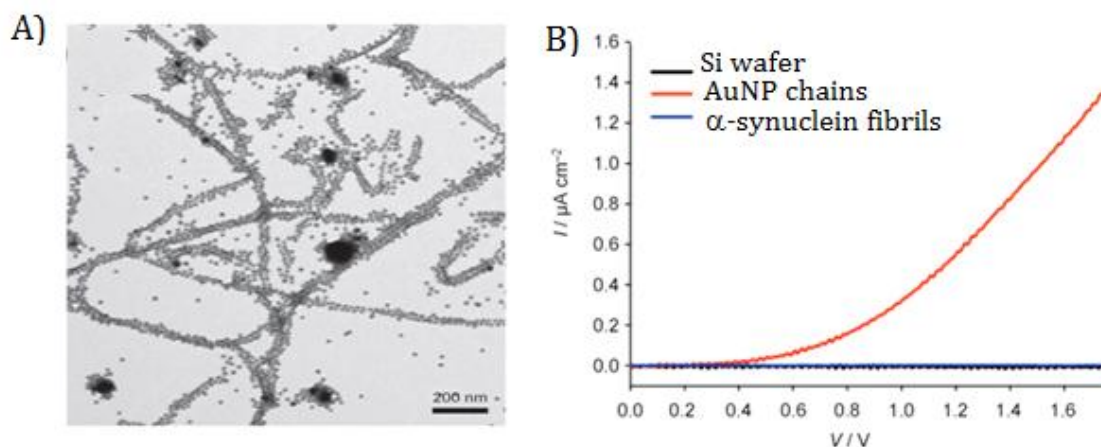
Figure 1.8. A) TEM image of the pH induced AuNP chains. B) *I-V* response which revealed a nonlinear *I-V* curve in which the current increased linearly to the applied voltage only from 1.2 V after a non-responding lag phase. [Adapted from reference 74].

Soft materials derived from organic molecules, through non-covalent interactions are extremely sensitive to the surrounding media and they exhibit reversible properties due to the dynamic nature of the non-covalent forces. As a

result, such soft materials are of great interest in chemistry, biology and material science. The chromophores based assemblies are of particular interest due to their inherent optical and electronic properties, which find application in organic electronics, light harvesting, as well as biological sensors. Therefore, design of chemosensors based on fluorescent molecules has been a subject of great interest to chemists. Among the diverse methods, the most common signal transduction schemes utilize optical or electrical properties. To produce a functional sensor, a highly sensitive optical transduction method such as fluorescence is of great advantage, where the analyte binding produces a reduction (turn-off), enhancement (turn-on), or wavelength shift in the emission. Recently, the molecular assemblies of π-systems have been investigated for their use in the sensing of analytes.[75]

Zang and co-workers have fabricated nanofibres from a strongly fluorescent n-type organic semiconductor material and have employed for efficient fluorescent sensing of gaseous amines.[76] The extended 1D molecular arrangement obtained for **16** (Figure 1.9A) was likely dominated by the π-π interactions between perylene backbones in cooperation with the hydrophobic interactions between the side chains having appropriate size (Figure 1.9B). These red fluorescence of nanofibers (Figure 1.9C) with quantum yield of *ca*. 15% showed quenching when exposed to aniline vapors. Such a porous and emissive nanofibres were found to be efficient in probing gaseous molecules with high sensitivity and fast time response. The emission intensity of the film monitored upon exposing to a saturated vapor of aniline (880 ppm) showed a decay lifetime of only 0.32 ns. The observed efficient

quenching has been attributed to the photoinduced electron transfer process having favorable energy difference between HOMO of aniline and **16**.

A)

16
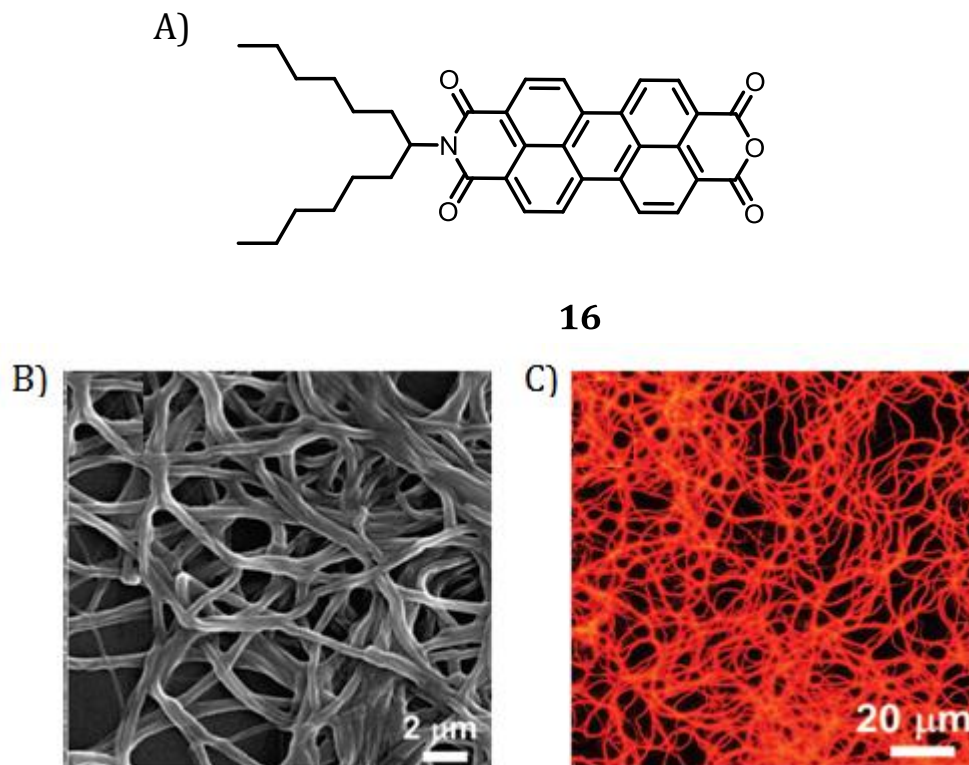
Figure 1.9. A) Chemical structure of **16**. B) SEM image of a nanofibril film deposited on a glass slide. C) Fluorescence optical microscopy image of a nanofibril film. [Adapted from reference 76].

Most of the organic dyes were intrinsically emissive but normally exhibit quenched emission at the higher concentrations due to the formation of their aggregates (self-quenching).[77] Therefore, the fluorophores exhibiting aggregation-induced emission (AIE) have been increasingly attracting much attention because such effective systems can have potential optoelectronic applications.[78] Importantly, the AIE molecules were endowed to exhibit the fluorescence "turn-on" switching in

response to the self-assembly, which makes them potential optical probes. Despite these advantages, only a few AIE examples have so far been reported which found use as probes for DNA,[79] protein[80] and heparin[81] and as a chiral recognition host.[82] Shinkai and co-workers have demonstrated that the AIE-based guanidinium bioprobe **17** (Chart 1.8), exhibited the nonlinear fluorescence response accompanying the self-assembly of TPE in the presence of ATP.[83]

17
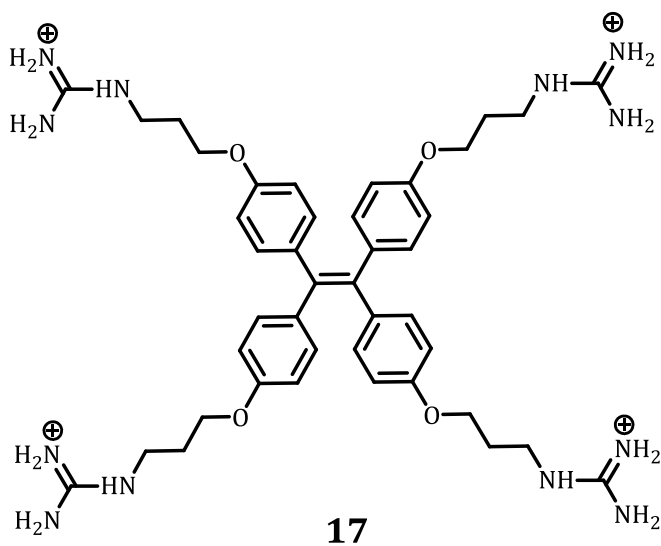
Chart 1.8

Recently, the self-assembly of nanopartcles have attracted attention in nanoformulations that showed many therapeutic advantages over conventional formulations. Liang *et al.*,[84] developed traceable nano-formulations to closely monitor the drug delivery. They have developed a new drug delivery system (DDS) using tetraphenylethene **18**, to fabricate a self-assembled micelle with aggregation-induced emission (AIE micelle). AIE mechanism makes the nano-carriers visible for

high-quality imaging and the switching on and off of the AIE was intrinsically controlled by the assembly and disassembly of the micelles. This was tested for doxorubicin (DOX) delivery and intracellular imaging applications. For DOX-loaded micelles (TPED), the DOX content was reached as much as 15.3% by weight, and the anticancer efficiency was found to be higher than that observed for free DOX. At the same time, the high-quality imaging was obtained to trace the intracellular delivery of the TPED (Figure 1.10) using this system.

A)

B)

18
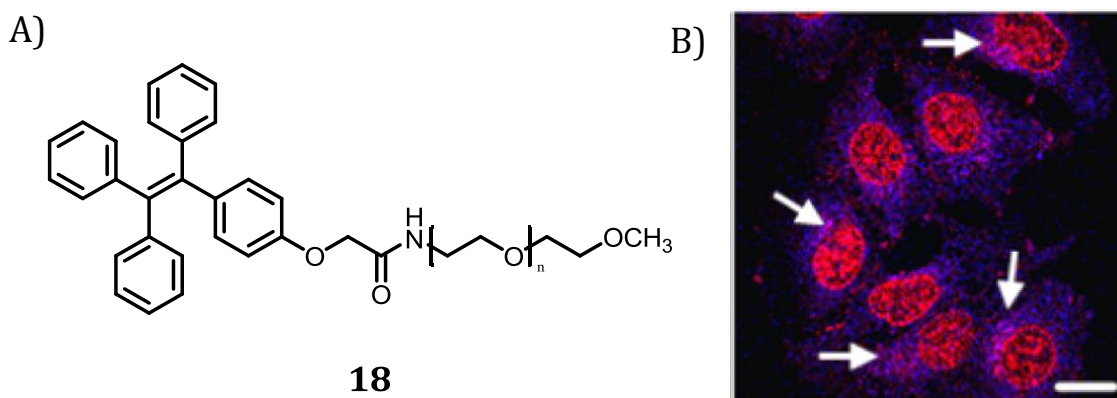
Figure 1.10. A) Chemical structure of **18.** B) CLSM images of the distribution of DOX-loaded micelles. MCF-7 breast cancer cells were incubated with TPED (TPE–mPEG 75 µM and DOX 5.0 µM) for 4 h. Scale bars are 20 µm. [Adapted from reference 84].

With a view to develop organic and supramolecular assemblies for biological applications, Betsy *et al*.,[85] have developed novel amphiphilic porphyrin systems containing the pyridine pincer systems and have investigated their photophysical and morphological transformations under different conditions. One of these systems, for example **19**, exhibited vesicular structures in methanol, while in water

it showed time-dependent nanofibers, nano-networks and sheet-like structures (Chart 1.9). Interestingly, the authors have demonstrated that the vesicular structures formed in methanol can be utilized to encapsulate a hydrophilic guest molecule HPTS (8-hydroxypyrene-1,3,6-trisulfonate), which on demand can be released into the aqueous medium by varying the solvent polarity and time interval.

19
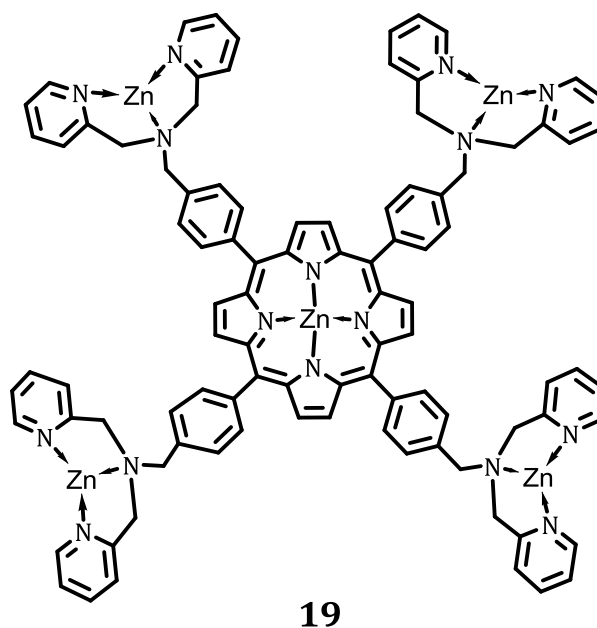
Chart 1.9

Recently, Anees and co-workers have demonstrated the versatility of an organic dye nanoparticle for the sensing of serum albumin proteins (SAP) in a pool of other biomolecules.[86] The squaraine dye **20** in its native molecular form was reactive to a variety of thiol containing molecules. However, when the dye self-assembled to form nanoparticles, only SAP could selectively interact with the dye thereby opening the access for a thiol attack. Thus, the dormant fluorescence moiety

present in the squaraine dye **20** (Chart 1.10), gets activated latently, allowing the specific sensing of SAP by a "turn-on" green fluorescence mechanism. The selective covalent modification of SAP was achieved only with the self-assembled system and not with the monomeric dye. The enhanced selectivity of the squaraine nanoparticles allowed the authors to use them for the quantitative estimation of HSA in human blood samples. The described self-assembly approach using a small organic NIR dye having a dormant fluorophore, which was latently activatable through a nucleophilic attack was a model example for empowering a small molecular fluorophore to a reaction specific nanosensor by self-assembly.
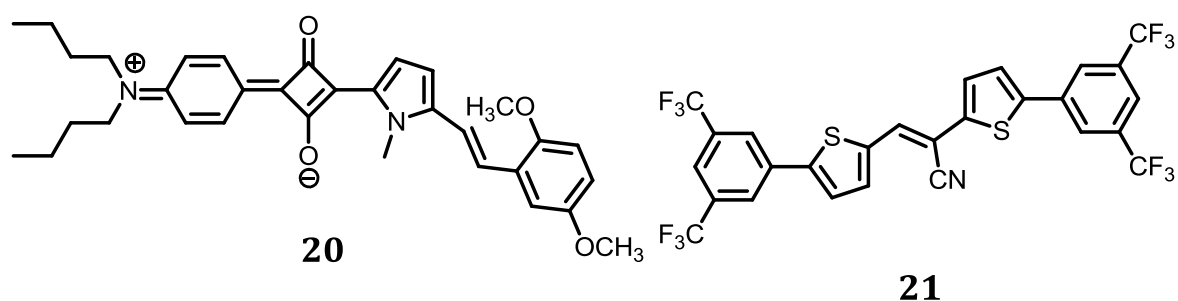
Chart 1.10

Insights on the self-assembly of π-conjugated oligomers leading to nano-sized architectures, controlled size and shape are important in organic electronic devices due to their unique electronic properties. In this context, approaches for the preparation of 1D fibres of organic molecules have attracted the attention of chemists since these 1D structures are expected to have good electronic conductivity and high charge-carrier mobility, required for a variety of electronic applications. At the molecular level, conjugated systems represent the simplest

models of molecular wires, which together with their complementary functions either as molecular switches or logical gates.[87]

For example, Park and co-workers have reported the semiconducting one dimensional nanowires (1D NWs) from the fused thiophene derivative **21** (Chart 1.10).[87] Detailed UV-Vis, AFM and XRD analyses have revealed the strong self-assembling capability of these systems that led to the formation of 1D NWs exhibiting a drastic fluorescence emission enhancement upon the formation of NW aggregates. Further, the conducting probe-atomic force microscopy (CP-AFM) and space charge limited current (SCLC) measurements have revealed that the well-ordered 1D NWs exhibit good current flow along the crystals with an effective carrier mobility of up to $3.1 \text{ cm}^2 \text{ V}^{-1} \text{ s}^{-1}$.

Aida and co-workers have made significant contribution to the self-assembly of hexa-*peri*-hexabenzocoronene (HBC) derivatives. For example, they have reported the formation of nanotubes of an amphiphilic derivative **22** (Chart 1.11), from THF solution. These nanotubes showed an aspect ratio greater than 1000 and exhibited 14 nm width.[61] The walls of the tubes consisted of helical arrays of π-stacked coronenes covered by hydrophilic glycol chains. Interestingly, an individual nanotube could be positioned across Pt nanogap electrodes (180 nm) on a SiO_2 substrate. The tube was essentially insulating, however, after oxidation with nitrosonium tetrafluoroborate ($NOBF_4$), it showed an *I-V* profile with an ohmic behaviour having a resistance of 2.5 MΩ at 285 K. This value was comparable to the inorganic semiconductor nanotubes reported in the literature.

22
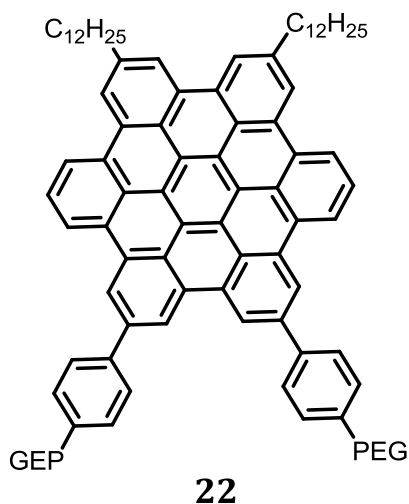
Chart 1.11

As described above the self-assembled functional materials have attracted much attention in recent years and are being explored for a variety of applications. The elucidation of the assembly from the molecular level to small and large supramolecular nanosystems constitutes a bridge between molecules and their morphologies and functions, and thus provides a guideline for the design of advanced molecular materials. As can be deduced from this chapter, it is possible not only to study material properties at the supramolecular level, but also to tune their macroscopic properties for potential applications.

1.4. OBJECTIVES OF THE PRESENT INVESTIGATION

The molecular self-assembly is a key concept in supramolecular chemistry and which has been proven to be a reliable approach towards the synthesis of a variety of versatile nanomaterials. These self-assembled soft nanomaterials have been exploited in a wide range of areas from chemistry and biology to material

science. In this context, one of our objectives has been to synthesize the self-assembled nanostructures using biological and synthetic building blocks. We have synthesized biocompatible nano-biohybrid systems, using γ-globulin, a blood plasma protein as a capping, reducing as well as a templating agent. Our approach offered a way to understand the role played by the self-assembly of the protein in ordering and knocking out of the metal nanoparticles and also in the design of nano-biohybrid materials for medicinal and optoelectronic applications. Another objective has been the development systems based on water soluble near infrared absorbing squaraine dyes as protein labeling as well as anti-amyloid agents, wherein the amyloid fibres were believed to be involved in several disorders, such as Alzheimer's disease, cystic fibrosis, and prion diseases. The synthesized dyes showed efficient interactions with lysozyme and also acted as effective inhibitors of the amyloid fibres derived from lysozyme. Yet another objective of the thesis has been the synthesis and investigation of photophysical and self-assembly properties of novel electron donor and acceptor conjugates based on tetraphenylethene and benzothiazole chromophores. The nanoparticles derived from these conjugates exhibited high stability, fluorescence emission and good biocompatibility in the aqueous medium, thereby demonstrating their potential in cell tracing and imaging applications.

1.5. REFERENCES

1. a) A. A. Johannes, W. Elemans, A. E. Rowan and R. J. M. Nolte, *J. Mater. Chem.*, **2003**, *13*, 2661; b) G. A. Ozin, K. Hou, B. V. Lotsch, L. Cademartiri, D. P. Puzzo, F. Scotognella, A. Ghadimi and J. Thomson, *Mater. Today,* **2009**, *12*, 12.

2. a) J. M. Lehn, *Chemica Scripta.*, **1988**; *28*, 237; b) J. M. Lehn, *Science*, **2002**, *295*, 2400; c) D. S. Lawrence, T. Jiang and M. Levett, *Chem. Rev.*, **1995**, *95*, 2229; d) J. M. Lehn, *Angew. Chem., Int. Ed.*, **1990**, *29*, 1304.

3. D. J. Prockop and A. Fertala, *J. Struct. Biol.*, **1998**, *122*, 111.

4. B. Alberts, D. Bray, J. Lewis, M. Raff, K. Roberts and J. D. Watson, *Molecular Biology of the Cell,* Garland, New York, **1994**.

5. G. M. Whitesides and M. Boncheva, *Proc. Natl. Acad. Sci. U.S.A.*, **2002**, *99,* 4769.

6. D. Philip and J. F. Stoddart, *Angew. Chem.Int. Ed.*, **1996**, *35***,** 1155.

7. J. M. Lehn and P. Ball, *The New Chemistry*, Cambridge Univ. Press, Cambridge, **2000**.

8. G. M. Whitesides and B. Grzybowski, *Science*, **2002**, *295*, 2418.

9. a) G. R. Desiraju, *Crystal Engineering: The Design of Organic Solids*, Elsevier, New York, **1989**; b) D. F. Evans and H. Wennerstrom, *The Colloidal Domain: Where Physics, Chemistry, Biology, and Technology Meet*, Wiley, New York, **1999**.

10. M. N. Jones and D. Chapman, *Micelles, Monolayers, and Biomembranes*, Wiley, New York, **1995**.

11.   A. Kumar, N. A. Abbott, E. Kim, H. A. Biebuyck and G. M. Whitesides, *Acc. Chem. Res.*, **1995**, *28*, 219.

12.   K. E. Schwiebert, D. N. Chin, J. C. MacDonald and G. M. Whitesides, *J. Am. Chem. Soc.*, **1996**, *118*, 4018.

13.   M. L. Schmidt, A. Fechtenkotter, K. Mullen, E. Moons, R. H. Friend and J. D. Mackenzie, *Science*, **2001**, *293*, 1119.

14.   C. D. Rosa, C. Park, E. L. Thomas and B. Lotz, *Nature*, **2000**, *405*, 433.

15.   G. M. Whitesides, *Sci. Am.*, **1995**, *273*, 146.

16.   F. S. Bates, M. A. Hillmyer, T. P. Lodge, C. M. Bates, K. T. Delaney and G. H. Fredrickson, *Science*, **2012**, *336*, 434.

17.   A. V. Ruzette and L. Leibler, *Nat. Mater.*, **2005**, *4*, 19.

18.   Y. Xia, T. D. Nguyen, M. Yang, B. Lee, A. Santos, P. Podsiadlo, Z. Tang, S. C. Glotzer and N. A. Kotov, *Nat. Nanotechnol.*, **2011**, *6*, 580.

19.   E. V. Shevchenko, D. V. Talapin, N. A. Kotov, S. Obrien and C. B. Murray, *Nature*, **2006**, *439*, 55.

20.   K. Liu, N. Zhao and E. Kumacheva, *Chem. Soc. Rev.*, **2011**, *40*, 656.

21.   T. Kato, N. Mizoshita and K. Kishimoto, *Angew. Chem., Int. Ed.*, **2006**, *45*, 38.

22.   O. Ikkala and G. T. Brinke, *Science,* **2002**, *295*, 2407.

23.   J. Aizenberg, A. J. Black and G. M. Whitesides, *Nature*, **1999**, *398*, 495.

24.   A. Blaaderen, R. Ruel and P. Wiltzius, *Nature*, **1997**, *385*, 321.

25.   M. M. Burns, J. M. Fournier and J. A. Golovchenko, *Science*, **1991**, *252*, 1049.

26. L. Isaacs, D. N. Chin, N. Bowden, Y. Xia and G. M. Whitesides, *Supramolecular Technology*, Wiley, New York, **1999**.

27. H. Sirringhaus, T. Kawase, R. H. Friend, T. Shimoda, M. Indrasekaran, W. Wu and E. P. Woo, *Science,* **2000,** *290***,** 2123.

28. J. A. Rogers, Z. Bao, K. Baldwin, A. Dodabalapur, B. Crone, V. R. Raju, V. Kuck, H. Katz, K. Amundson, J. Ewing and P. Drzaic, *Proc. Natl. Acad. Sci. U.S.A.*, **2001**, *98***,** 4835.

29. a) S. A. Jenekhe and L. X. Chen, *Science*, **1999**, *283***,** 372; b) Y. Xia, B. Gates, Y. Yin and Y. Lu, *Adv. Mater.,* **2000**, *12***,** 693.

30. M. H. Wu and G. M. Whitesides, *Appl. Phys. Lett.*, **2001**, *78***,** 2273.

31. C. M. Lieber, *Sci. Am.,* **2001**, *285*, 58.

32. V. I. Klimov, A. A. Mikhailovski, S. Xu, A. Malko, J. A. Hollingsworth, C.A. Leatherdale, H. J. Eisler and M. G. Bawendi, *Science,* **2000**, *290***,** 314.

33. S. H. Sun, C. B. Murray, D. Weller, L. Folks and A. Moser, *Science*, **2000**, *287*, 1989.

34. a) A. Klug, *Angew. Chem.*, **1983**, *95*, 34; b) I. W. Hamley, *Angew. Chem.*, *Int. Ed.*, **2007**, *46*, 8128.

35. S.G. Zhang, *Nat. Biotechnol.*, **2003**, *21*, 1171.

36. H. M. Konig and A. F. M. Kilbinger, *Angew. Chem. Int. Ed.*, **2007**, *46*, 8334.

37. M. Sarikaya, C. Tamerler and A. K. Y. Jen, *Nat. Mater.*, **2003**, *2*, 577.

38. U. Hersel, C. Dahmen and H. Kessler, *Biomaterials*, **2003**, *24*, 4385.

39.   a) M. R. Ghadiri, J. R. Granja, R. A. Milligan, D. E. McRee and N. Khazanovich, *Nature*, **1993**, *366*, 324; b) C. Valery, M. Paternostre, B. Robert, T. G. Krzywicki, T. Narayanan, J. C. Dedieu, G. Keller, M. L. Torres, R. C. Cheikh, P. Calvo and F. Artzner, *Proc. Natl. Acad. Sci. U. S. A.*, **2003**, *100*, 10258.

40.   A. Aggeli, M. Bell and N. Boden*, J. Mater. Chem.*, **1997**, *7*, 1135.

41.   A. Aggeli, I. A. Nyrkova and M. Bell, *Proc. Natl. Acad. Sci. U. S. A.*, **2001**, *98*, 11857.

42.   M. R. Ghadiri, J. R. Granja and L. K. Buehler, *Nature*, **1994**, *369*, 34.

43.   Y. C. Yu, P. Berndt and M. Tirrell, *J. Am. Chem. Soc.*, **1996**, *118*, 12515.

44.   M. L. Deng, D. F. Yu and Y. B. Hou, *J. Phys. Chem. B,* **2009**, *113*, 8539.

45.   X. B. Zhao, F. Pan and H. Xu, *Chem. Soc. Rev.*, **2010**, *39*, 3480.

46.   P. Berndt, G. B. Fields and M. Tirrell, *J. Am. Chem. Soc.*, **1995**, *117*, 9515.

47.   a) K. C. Lee, P. A. Carlson and A. S. Goldstein, *Langmuir*, **1999**, *15*, 5500; b) J. H. Wook, S.E. Paramonov and J.D. Hartgerink, *Soft Matter*, **2006**, *2*, 177.

48.   J. D. Hartgerink, E. Beniash and S. I. Stupp, *Proc. Natl. Acad. Sci. U. S. A.*, **2002**, *99*, 5133.

49.   a) E. K. O'Shea, R. Rutkowski and P. S .Kim, *Science*, **1989**, *243*, 538; b) M. H. Hecht, J. S. Richardson and D. C. Richardson, *Science*, **1990**, *249*, 884.

50.   a) K. Rajagopal and J. P. Schneider, *Curr. Opin. Struct. Biol.*, **2004**, *14*, 480; b) E. Gazit, *Chem. Soc. Rev.*, **2006**, *36*, 1263.

51.   a) R. Pellarin and A. Caflisch, *J. Mol. Biol.,* **2006**, *36,* 882; b) A. T. Petkova, R. D. Leapman, Z. Guo, W. Yau, M.P. Mattson and R. Tycko, *Science*, **2005**, *307*, 262.

52.   M. Calero and M. Gasset, *Mol. Biol.*, **2005**, *299*, 129.

53.   F. E. Cohen, K. M. Pan, Z. Huang, M. Baldwin, R. J. Flelterick and S. B. Pruisner, *Science*, **1994**, *264*, 530.

54.   a) M. Reches and E. Gazit, *Nano Lett.*, **2004**, *4*, 581; b) A. Mahler, M. Reches, M. Rechter, S. Cohen and E. Gazit, *Adv.Mater.*, **2006**, *18*, 1365; c) G. Whitesides, J. P. Mathias and C. T. Seto, *Science*, **1991**, 2*5*4, 1312.

55.   S. I. Stupp, V. Lebonheur, K. Walker, L. S. Li, K. E. Huggins, M. Kese and A. Amstutz, *Science*, **1997**, *276*, 384.

56.   a) S. R. P Meijer, F. H. Beijer, L. Brunsveld, B. J. Folmer, J. H. Hirschberg, R. F. Lange, J. K. Lowe and E. W. Meijer, *Science*, **1997**, *278*, 1601; b) J. Wu, W. Pisula and K. Len, *Chem. Rev.*, **2007**, *107*, 718.

57.   Y. Yamamoto, T. Fukushima, W. Jin, A. Kosaka, T. Hara, T. Nakamura, A. Saeki, S. Seki, S. Tagawa and T. Aida*, Adv. Mater.*, **2006**, *18*, 1297.

58.   A. R. Carretero, T. Aytun, C. J. Bruns, C. J. Newcomb, W. W. Tsai and S. I. Stupp, J*. Mater. Chem. A*, **2013**, *1*, 11674.

59.   a) A. Lohr, M. Lysetska and F. Würthner, *Angew. Chem., Int. Ed.*, **2005**, *44*, 5071; b) A. Lohr, T. Gress, M. Deppisch, M. Knoll, F. Würthner, *Synthesis*, **2007**, *2011*, 3073.

60.   A. P. H. J. Schenning, P. Jonkheijm, E. Peeters and E. W.Meijer, *J. Am. Chem. Soc.,* **2001**, *123*, 409.

61.   J. Hill, W. Jin, A. Kosaka, T. Fukushima, H. Ichihara, T. Shimomura, K. Ito, T. Hashizume, N. Ishii and T. Aida, *Science*, **2004**, *304*, 1481.

62.   Z. Wang, C. J. Medforth and J. A. Shelnutt, *J. Am. Chem. Soc.*, **2004**, *126*, 954.

63.   a) K. Sugiyasu, N. Fujita and S. Shinkai, *Angew. Chem. Int. Ed.*, **2004**, *43,* 1229; b) K. Sugiyasu, S. Kawano, N. Fujita and S. Shinkai, *Chem. Mater.,* **2008**, *20*, 2863.

64.   X. Q. Li, V. Stepanenko, Z. Chen, P. Prins, L. D. A. Siebbeles and F. Würthner, *Chem. Commun.*, **2006**, 3871.

65.   P. Mukhopadhyay, Y. Iwashita, M. Shirakawa, S. I. Kawano, N. Fujita and S. Shinkai, *Angew. Chem., Int. Ed.*, **2006**, *45*, 1592.

66.   C.L. Chen and N.L. Rosi, *Angew. Chem., Int. Ed.*, **2010**, *49*, 1924.

67.   a) O. Yuval, S. Bappaditya and V. M. Rotello, *Chem. Soc. Rev.*, **2008**, *37*, 1814; b) S. Eustis and M. A. El-Sayed, *Chem. Soc. Rev.*, **2006**, *35*, 209.

68.   M. S. Lamm, N. Sharma, K. Rajagopal, F. L. Beyer, J. P. Schneider and D. J. Pochan, *Adv. Mater.*, **2008**, *20*, 447.

69.   C. L. Chen, P. J. Zhang and N. L. Rosi, *J. Am. Chem. Soc.*, **2008**, *130*, 13555.

70.   R. R. Naik, S. J. Stringer, G. Agarwal, S. E. Jones and M. O. Stone, *Nat. Mater.*, **2002**, *1*, 169; b) J. M. Slocik, M. O. Stone and R. R. Naik, *Small,* **2005**, *1*, 1048.

71.   M. G. Warner and J. E. Hutchison, *Nat. Mater.*, **2003**, *2*, 272.

72.   M. S. Hu, H. L. Chen, C. H. Shen, L. S. Hong, B. R. Huang, K. H. Chen and L. C. Chen, *Nat. Mater.*, **2006**, *5*, 102.

73.   M. Quinten, A. Leitner, J. R. Krenn and F. R. Aussenegg, *Opt. Lett.*, **1998**, *23*, 1331.

74.   D. Lee, Y. J. Choe, Y. S. Choi, G. Bhak, J. Lee and S. R. Paik, *Angew. Chem., Int. Ed.*, **2011**, *50*, 1332.

75.   L. C. Palmer and S. I. Stupp, *Acc. Chem. Res.*, **2008**, *41*, 1674.

76.   Y. K. Che, X. M. Yang, S. Loser and L. Zang, *Nano Lett.*, **2008**, *8*, 2219.

77.   J. R. Lakowicz, *Principles of Fluorescence Spectroscopy*, Kluwer Academic/Plenum Publishers, New York, **1999**.

78.   a) Y. Hong, J. W. Y. Lam and B. Z. Tang, *Chem. Soc. Rev.*, **2011**, *40*, 5361; b) J. Wu, W. Liu, J. Ge, H. Zhang and P. Wang, *Chem. Soc. Rev.*, **2011**, *40*, 3483.

79.   Y. Hong, H. Xiong, J. W. Y. Lam, M. Haubler, J. Liu, Y. Yu, Y. Zhong, H. H. Y. Sung, I. D. Williams, K. S. Wong and B. Z. Tang, *Chem. Eur. J.*, **2010**, *16*, 1232.

80.   H. Tong, Y. Hong, Y. Dong, M. Haubler, Z. Li, J. W. Y. Lam, Y. Dong, H. H. Y. Sung, I. D. Williams and B. Z. Tang, *J. Phys.Chem. B*, **2007**, *111*, 11817.

81.   M. Wang, D. Zhang, G. Zhang and D. Zhu, *Chem. Commun.*, **2008**, 4469.

82.   D. M. Li and Y. S. Zheng, *Chem. Commun.*, **2011**, *47*, 10139.

83.   T. Noguchi, T. Shiraki, A. Dawn, Y. Tsuchiya, L. T. N. Lien, T. Yamamoto and S. Shinkai, *Chem. Commun.*, **2012** ,*48*, 8090.

84.   C. Zhang, S. Jin, S. Li, X. Xue, J. Liu, Y. Huang, Y. Jiang, W. Q. Chen, G. Zou, and X.-J. Liang, *ACS Appl. Mater. Interfaces,* **2014**, *6*, 5212.

85.   B. Marydasan, A. K. Nair and D. Ramaiah, *RSC Advances,* **2013**, *3*, 3815.

86.   P. Anees, S. Sreejith and A. Ajayaghosh, *J. Am. Chem. Soc.*, **2014**, *136*, 13233.

87.   a) J. M. Lehn, *Angew. Chem.*, *Int. Ed.*, **1988**, *27*, 89; b) A. Aviram, *J. Am. Chem. Soc.*, **1988**, *110*, 5687.

SYNTHESIS, PHOTOPHYSICAL AND MORPHOLOGICAL ASPECTS OF PROTEIN-GOLD NANOPARTICLES
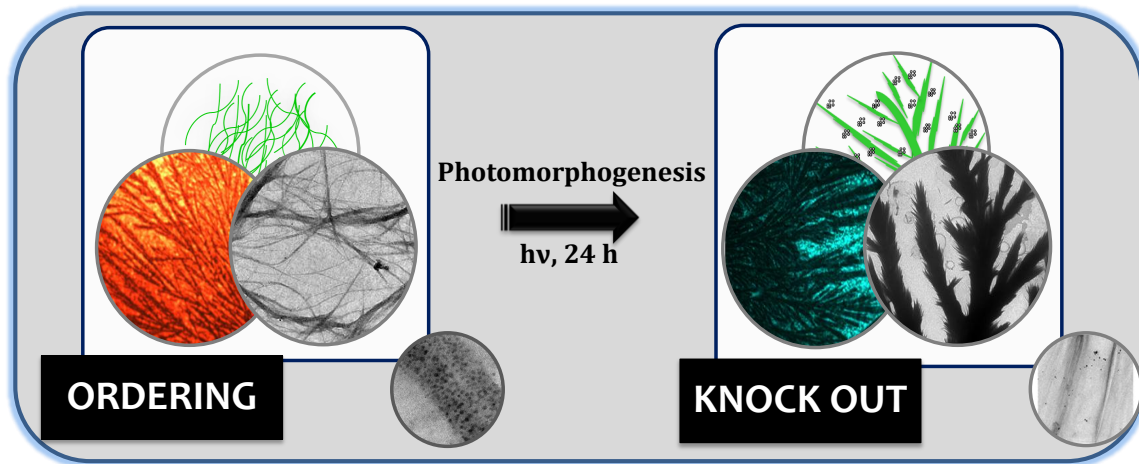
2.1. ABSTRACT

With an objective of developing nano-bioconjugates, we have synthesized monodisperse protein-gold nanoparticles (AuNPs), wherein γ-globulin, a blood plasma protein acted as a capping, reducing as well as a templating agent. As analyzed through various photophysical, biophysical and microscopic techniques such as transmission electron microscope (TEM), atomic force microscope (AFM), conductive AFM (C-AFM), scanning electron microscope (SEM), dynamic light scattering (DLS), optical polarization microscopy (OPM), circular dichroism (CD), and fourier transform infrared spectroscopy (FTIR), we observed that the initial photoactivation of γ-globulin at pH 12 for 3 h resulted in small protein fibres of

ca. 20 ± 5 nm in size. Subsequently, these fibres found to assist in the alignment of the colloidal gold nanoparticles of average diameter of *ca.* 2-2.5 nm on the surface of protein. At this particular irradiation time, the nano-bioconjugate thus formed, exhibited negligible surface plasmon resonance (SPR) absorption, but showed an intense photoluminescence at 680 nm. Further, irradiation of the solution for 24 h led to the formation of self-assembled long fibres of the protein of *ca.* 2 ± 0.5 μm in diameter and *ca.* 18 μm in length. Interestingly, such a morphological transformation resulted in the sequential knock out of the anchored gold nanoparticles resulting in the clustering of the nanoparticles of size *ca.* 5-6 nm and observation of the surface plasmon resonance band at 520 nm, with the concomitant quenching of luminescence intensity at 680 nm. The observation of light triggered self-assembly of the protein and its effect on controlling the fate of the anchored nanoparticles can be compared with the naturally occurring process such as photomorphogenesis. Furthermore, our approach offers a way to understand the role played by the self-assembly of the protein in ordering and knock out of metal nanoparticles and also in designing of nano-biohybrid materials for medicinal and optoelectronic applications.

2. 2. INTRODUCTION

Integration of biotechnology and nanotechnology during the last decade led to the development of hybrid nanostructures, which can have potential applications in photonics, electronics, medicine and catalysis.[1] These new nano-biohybrids

incorporate the properties of both biomaterials and nanoparticles (NP) and both of which can in principle undergo self-assembly to form 1D, 2D and 3D architectures.[2] Among the various synthetic strategies reported, the top-down and bottom-up approaches are being actively explored for the assembling of complex nanostructures.[3] These self-assembly processes are critical for the "bottom-up" construction of nanostructures, which enable the fabrication of three-dimensional structures on the nano- and micrometer length scale.[4] The use of biological systems as templates for creating such nanoarchitectures is being recently explored as a feasible bottom up approach because of the advantages like simplicity, ease of shape control and time effectiveness.[5] The nature is a beautiful example, wherein bacteria, viruses, DNA, and proteins are regularly involved in the creation of unique nanoassemblies to achieve and maximize efficacy of various biological processes.[6]

Despite the remarkable advancements of nanoscience in recent years, relatively little is known about the effects of nanoscale objects on biological systems and their potential applications.[7] The understanding of the interaction of the proteins with nanoparticles is still of great concern for their successful use in nanomedicine, nanotoxicology and nanophotonics.[7] Acquiring of knowledge on the three-dimensional structure of the protein is important for understanding its functions. The proteins are nitrogen-containing macromolecules, which are one of the basic units of life systems. These macromolecules are made up of amino acids as the monomeric units and are joined by peptide linkages.[8] Interactions of the

nanoparticles with the proteins, may alter the protein conformation, or perturb the its normal function, and thereby induce unexpected biological reactions.[7]

Of the various biological building blocks, the peptides/proteins and their unique property of self-assembly, have attracted a lot of attention in recent years as platforms for the bottom-up approach in the design of the nanoarchitechtures.[9] For example, Wang and co-workers have demonstrated that T1 peptide RGYFWAGDYNYF, undergoes self-assembly to form nanofibers with lengths of up to several micrometers and average diameters of 10 nm.[10] By using the similar strategy, Pochan and co-workers have synthesized sheets of gold nanoparticles. In these cases, the non-twisted laminated β-sheet peptide fibrils acted as a template, and which induced the gold nanoparticles to undergo intercalation within fibril laminates.[11] The formation of the aggregates of nanoparticles were induced due to the electrostatic interactions between the positively charged lysine side chains of the fibrils and the charged nanoparticles. The assembly driven by electrostatic interactions between the nanoparticles and peptide scaffolds were very effective for the creation of supramolecular architectures of small negatively charged nanoparticles (<6 nm).[10,11] However, their wide applications were limited by the size of the nanoparticles, since the larger nanoparticles were known to normally bind randomly to the fibril surfaces.[12]

Moreover, there were also reports wherein the modifications in the protein fibre can be catalyzed by the interaction with nanophase materials leading to the growth of the extended assemblies.[13] Thus, the process of protein self-assembly has

been studied extensively and was widely established that such a process has been found to be sensitive to the external stimuli like pH, light, pressure and temperature.[14] By having control over the process of self-assembly of the proteins, it is possible to generate systems that can be effectively utilized as template/scaffolds for the synthesis of the ordered nanostructures. Moreover, the realm of usefulness of the well defined nanoscale properties of the metal nanostructures can be significantly enhanced by harnessing interparticle properties.[15] Thus, the synthesis of controllable ordered nanoparticle assemblies has been challenging in the context of their potential applications in the development of nanoscale electronic and optical devices.[14-16] The conformational changes occurring in the protein upon self-assembling processes is, often, crucial for its various functions. A large number of efforts have been devoted to the fabrication of the nanoparticle assemblies,[17] whose peculiar recognition mechanisms to-date remain elusive. However, there are important scientific and practical issues that need additional attention to further improve these methods and also to determine, which applications are best targeted with superstructures constructed by using these biological building blocks.

Among the various biomolecules for functionalization of the nanoparticles, we chose γ-globulin, since it belongs to a class of blood plasma proteins and is considered as antibody that helps to fight infections and diseases.[18] Herein, we describe the synthesis of monodisperse gold nanoparticles employing γ-globulin as a capping, reducing as well as templating agent. We observed pH, light and concentration dependent morphologies as analyzed through photophysical,

biophysical and microscopic techniques such as atomic force microscopy (AFM), transmission electron microscopy (TEM), scanning electron microscopy (SEM) and optical electron microscopy (OPM). Interestingly, the initially UV irradiation triggered self-assembly of γ-globulin found to control the anchoring of the nanoparticles, whereas on further irradiation led to the formation of long fibres, which eventually knocked out the ordered nanoparticles from the protein matrix. Interestingly, we observed that the protein γ-globulin acts as a capping, reducing as well as templating agent for ordering of these nanoparticles. Uniquely, this approach offers a way to understand the role played by the self-assembly of the protein in sequential ordering and knock out of the metal nanoparticles and also in the design of novel nano-biohybrid materials for medicinal and optoelectronic applications.

2.3. RESULTS AND DISCUSSION

2.3.1. Synthesis of Protein Functionalized Gold Nanoparticles

Synthesis of the protein functionalized biocompatible gold nanoparticles (AuNPs) involved the reaction of the aqueous solution of hydrogen tetrachloroaurate hydrate ($HAuCl_4$) with γ-globulin. The formation of the gold nanoparticles, thus formed, was found to depend on various external factors such as the reaction temperature and pH, in addition to the concentration of the capping agent used. These factors significantly altered the reduction and capping capability of the protein and hence the reduction kinetics, the nucleation and crystal growth and thereby, the formation of stable monodisperse gold nanoparticles. To study the

effect of concentration on the formation of the gold nanoparticles, we have varied the protein concentration (w/v = 0.1, 0.2 and 0.5%) and carried out the reaction with HAuCl$_4$. The variation in the protein concentration led to the formation of the nanoparticles with different sizes. It is well-known that the optical properties of the metal nanoparticles are strongly size and shape dependent.[4,5] Under these conditions, we observed the formation of size and shape dependent surface plasmon resonance (SPR). The formation of the surface plasmon resonance band was a clear indication that the γ-globulin can act as both reducing agent as well as a capping agent, thereby indicating the formation of stable gold nanoparticles. For example, at *ca.* 0.1% (w/v) of γ-globulin, we observed the formation of AuNPs having the surface
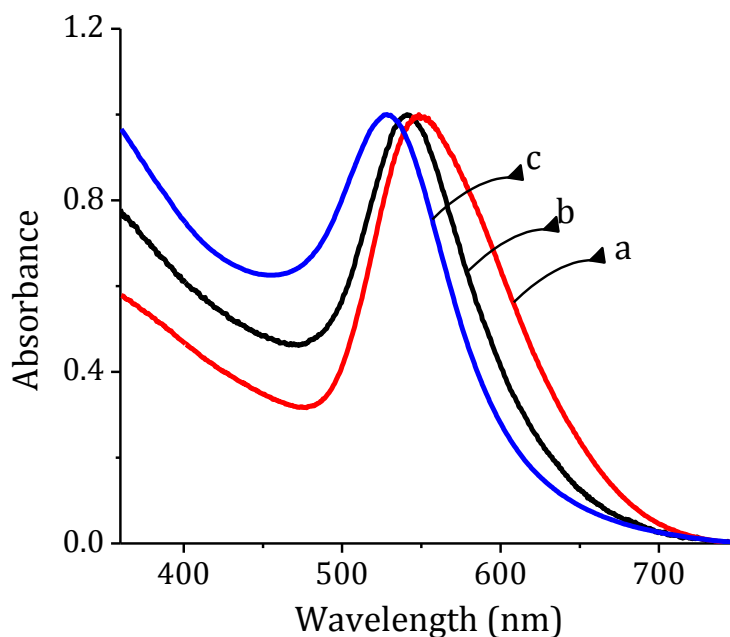
Figure 2.1. Changes in the surface plasmon resonance of γ-globulin-Au nanoparticles (AuNPs) synthesized at 60 °C from a solution containing a) 0.1%, b) 0.2% and c) 0.5% (w/v) of γ-globulin and HAuCl$_4$ (2 mM).

plasmon band at 548 nm (Figure 2.1), whereas at protein concentrations *ca*. 0.2% and 0.5% (w/v), we observed a blue shifted SPR bands at 540 and 528 nm, respectively. This blue shift in the absorption was attributed to the eventual narrowing of the size by varying the globulin concentration. However, the gold nanoparticles thus formed under these conditions were found to be highly polydisperse in nature.

To understand the changes observed in the surface plasmon resonace properties of γ-globulin-AuNPs at 60 °C, we have analyzed the samples through dynamic light scattering (DLS) and microscopic techniques such as TEM, AFM and SEM. At lower concentrations of γ-globulin (*ca*. 0.1-0.2% w/v) and pH 7, we observed predominantly a mixture of aggregated structures (Figure 2.2A) such as spherical, plate-like and irregular trigonal, hexagonal and polygonal shapes as confirmed through TEM (Figure 2.2C) and DLS analysis (Figure 2.3). The γ-globulin capped nanoparticles formed under these conditions showed an average diameter of
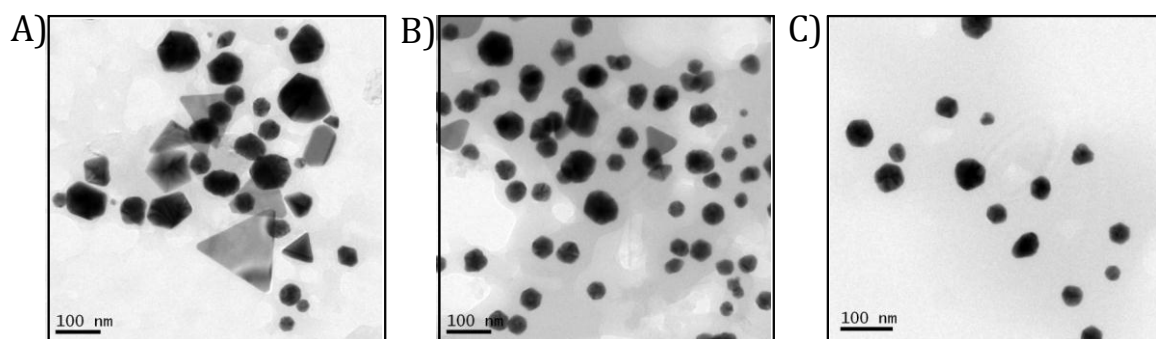
Figure 2.2. TEM images of the γ-globulin Au nanoparticles (AuNPs) synthesized at various protein concentrations (w/v) and HAuCl$_4$ (2 mM) by heating at 60 °C A) 0.1%, B) 0.2%, and C) 0.5%.

ca. 72 nm. Moreover, the size and stability of AuNPs showed negligible changes with the further increase in concentration of the protein after *ca.* 0.5% (w/v) of γ-globulin. The results of these initial characterization studies have led us to select *ca.* 0.5% (w/v) of γ-globulin for further studies to improve their monodispersity by adopting different methods like photoirradiation and changing the pH of the reaction mixture.
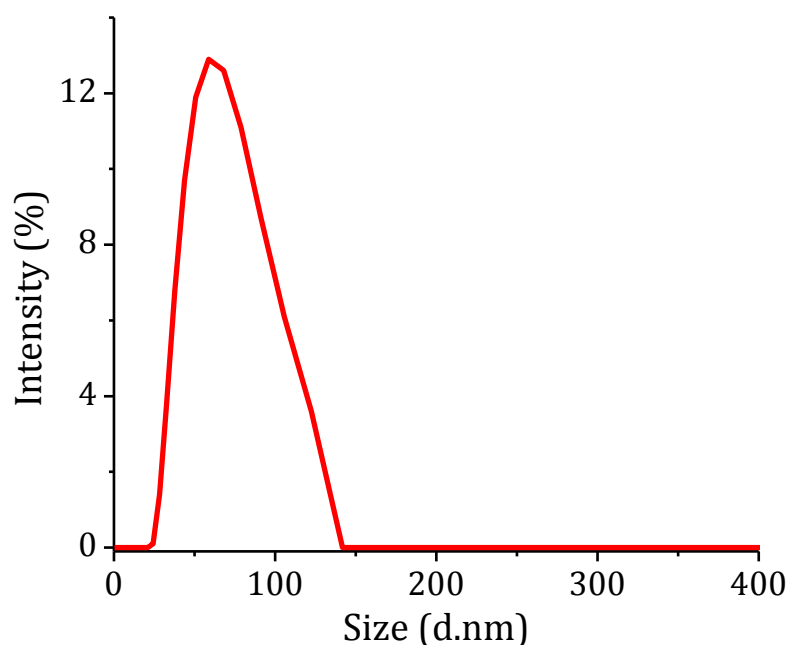

Figure 2.3. Dynamic light scattering data of 0.5% γ-globulin Au nanoparticles synthesized at 60 °C.

2.3.2. Effect of pH and Irradiation on Bioconjugate Formation

To synthesize monodisperse nanoparticles, we have employed irradiation technique and varied the irradiation time (*ca.* 1-24 h) as well as pH of the solution (*ca.* 7-12). When an aqueous solution of HAuCl$_4$ was irradiated for 1 h with a light

source of 350 nm in presence of *ca.* 0.5% of γ-globulin at pH 7, we observed the formation of the surface plasmon resonance (SPR) band centred at around 526 nm, corresponding to the nanoparticles. However, after 24 h of irradiation under these conditions, there was an increase in the intensity, but we could not observe any significant shift in the position of SPR band at 526 nm (Figure 2.4). This spectral observation indicated that the nanoparticles thus formed even after 24 h irradiation were stable and homogeneous. Of the various conditions investigated, interestingly, we observed the formation of homogeneous size distribution of *ca.* 27 nm of AuNPs (Figure 2.5) only under the irradiation conditions.
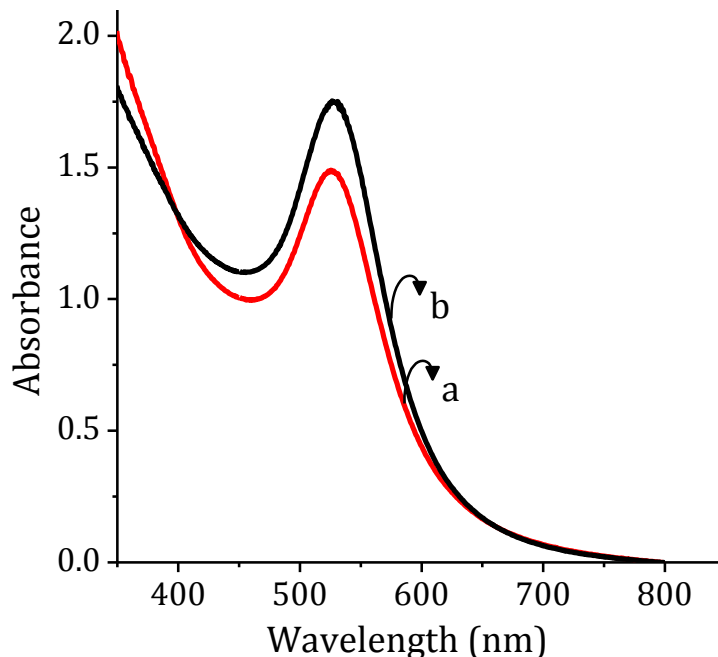

Figure 2.4. Surface plasmon resonance of 0.5% (w/v) γ-globulin-Au nanoparticles (AuNPs) synthesized by irradiation with 350 nm in presence of HAuCl$_4$ (2 mM) after a) 1 h irradiation b) 24 h irradiation.

These protein concentration dependent studies indicate that γ-globulin having amino and thiol groups[12] not only found to reduce the Au(III) ions, but also stabilize the nanoparticles. Moreover, the formation of the narrower size distribution of the nanoparticles under these conditions with the increase in the concentration of the protein supports the fact that γ-globulin acts both as a controller of nucleation as well as stabilizer as reported in the case of chitosan based gold nanoparticles.[19] Furthermore, our results indicated that though γ-globulin was able to reduce Au(III) ions as well as stabilize the nanoparticles, but the homogeneous size distribution of AuNPs was observed only upon irradiation, which demonstrate the importance of light excitation in the formation of the nanoparticles as reported in the literature.[20,21] In contrast, when the pH of the solution was increased to 12 and irradiated for *ca.* 1-3 h, we observed negligible formation of the
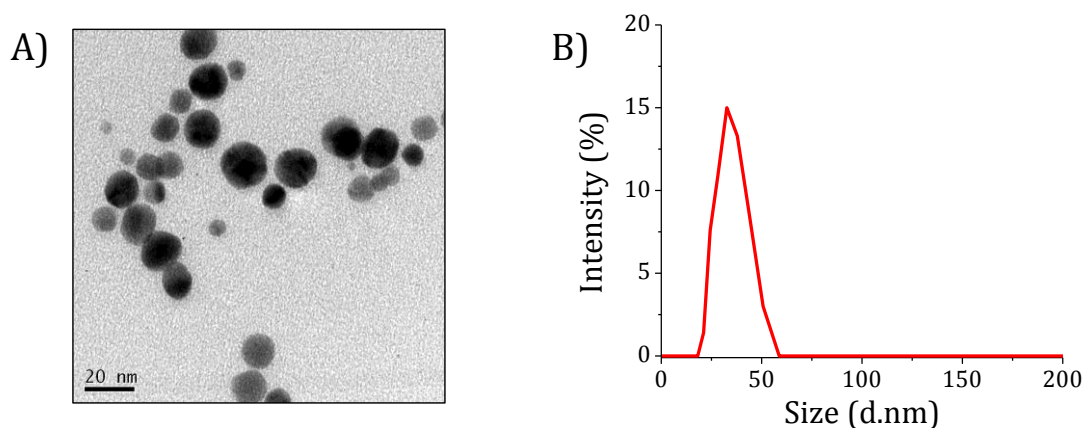

Figure 2.5. A) TEM images of 0.5% γ-globulin capped gold nanoparticle by irradiation at pH 7 with a light source of 350 nm B) DLS data of 0.5% γ-Globulin capped gold nanoparticles.

surface plasmon band. However, when the irradiation time was increased further for 12 h, we observed the evolution of the surface plasmon resonance band centered at around 520 nm and which became prominent after 24 h irradiation (Figure 2.6). In the emission spectrum, on the other hand, we initially observed intense red emission having maximum at *ca.* 680 nm along with a less prominent band at 450 nm after 3 h of irradiation (Figure 2.7). With increase in the irradiation time, we could observe quenching in the fluorescence intensity at *ca.* 680 nm. Inset of Figure 2.7 shows visual observation of fluorescence changes after irradiation of 24 h. In addition, we observed a visual color change of the solution from pale yellow to deep brown with the increase in irradiation time from *ca.* 3 to 24 h (Figure 2.8).
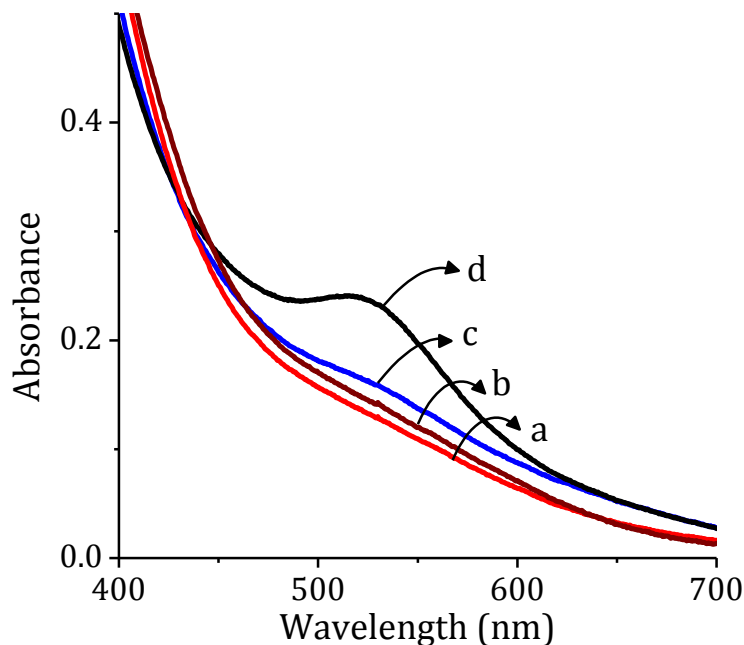
Figure 2.6. Irradiation time-dependent changes in the absorption spectra of the solution containing HAuCl$_4$ and 0.5% (w/v) of γ-globulin. Irradiation time, a) 3, b) 6, c) 12 and d) 24 h.
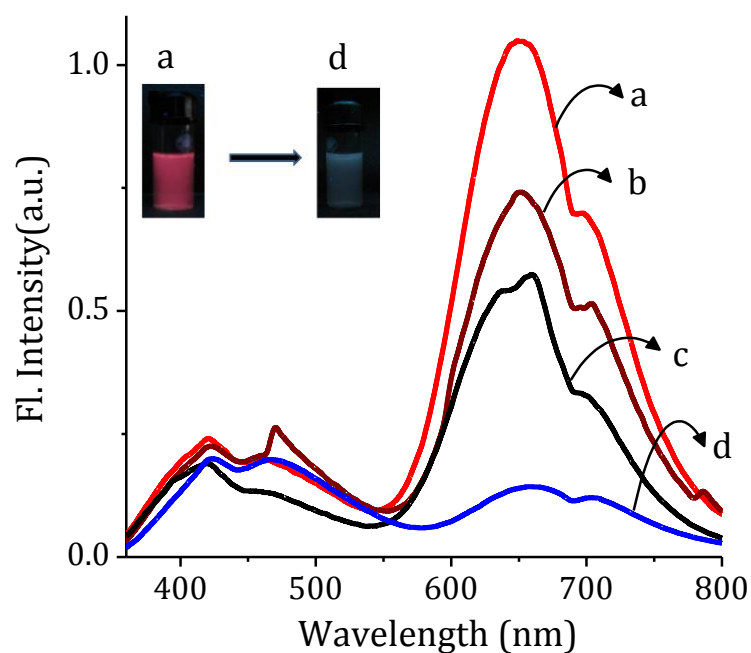
Figure 2.7. Irradiation time-dependent changes in fluorescence of HAuCl₄ solution containing 0.5% (w/v) of γ-globulin. Irradiation time, a) 3, b) 6, c) 12 and d) 24 h. Inset shows visual observation of fluorescence changes after irradiation time, a) 3 and d) 24 h. (λ_{ex} 350nm).
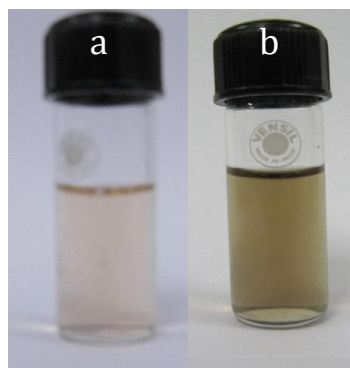
Figure 2.8. Visual observation of irradiation time-dependent changes in the color of HAuCl₄ solution containing 0.5% (w/v) of γ-globulin after irradiation time, a) 3 and b) 24 h.

Further, we have carried out the control experiments using γ-globulin alone under similar conditions. When γ-globulin alone was irradiated in the absence of HAuCl$_4$ under similar experimental conditions, it showed negligible absorption in the surface plasmon resonance region but exhibited only blue emission having maximum *ca.* 450 nm (Figure 2.9) as reported in the case of serum albumins.[25] Figure 2.10 shows the optical polarization microscopy (OPM) images monitoring the changes in the emission of γ-globulin-AuNPs at different stages of γ-globulin and HAuCl$_4$ (2 mM), upon irradiation using 360 nm excitation. We observed an intense red emission after the irradiation period of *ca.* 3-6 h of a solution containing 0.5% (w/v), which was supported by the emission observed at 680 nm (Figure 2.7). On
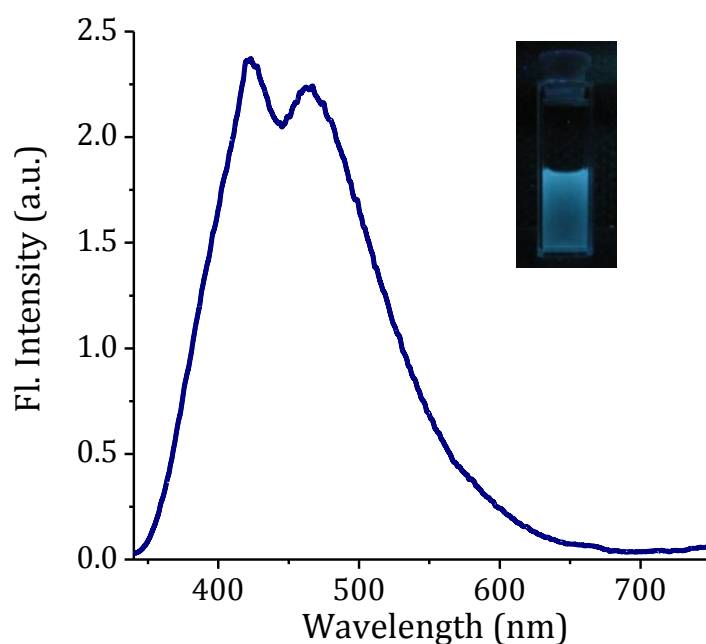
Figure 2.9. Fluorescence spectra of the γ-globulin protein fibres after the irradiation for 24 h using 350 nm light source in the absence of AuNPs. Inset shows the visual fluorescence of the protein alone.

further irradiation for a period of *ca.* 12 h, we observed the weakening of the red emission as shown in Figure 2.10B. When the solution was irradiated additionally for a period of *ca.* 24 h, interestingly, we observed the emission change from red to blue (Figure 2.10C). The results of the optical polarization microscopy were in accordance with the observations made in the steady-state and time-dependent fluorescence measurements for γ-globulin-AuNPs during the progress of irradiation.
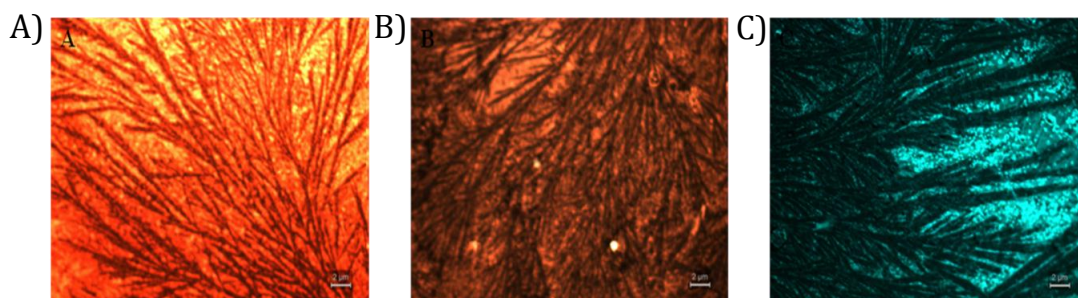
Figure 2.10. Time-dependent optical polarisation microscopic (OPM) images showing the emission changes during irradiation of a solution containing 0.5% (w/v) of γ-globulin plus HAuCl$_4$ (2 mM) at pH 12. Irradiation time, A) 6 B) 12 and C) 24 h. Excitation wavelength, 360 nm. Scale bars: (A), (B), and (C) 2 μm.

2.3.3. Morphological Analysis of Self-Assembled Bioconjugates

To have a better understanding of the irradiation time-dependent changes in the photophysical properties, we analyzed the time-dependent morphological changes of the solution containing *ca.* 0.5% (w/v) of γ-globulin and HAuCl$_4$ at pH 12 through TEM analysis. After the initial period of irradiation for *ca.* 3 h, we observed the ordering of AuNPs having an average diameter of *ca.* 2 ± 0.5 nm into the one

dimensional array within the protein fibre size of *ca.* 20 ± 5 nm (Figure 2.11). With the further increase in irradiation time, we observed the growth of t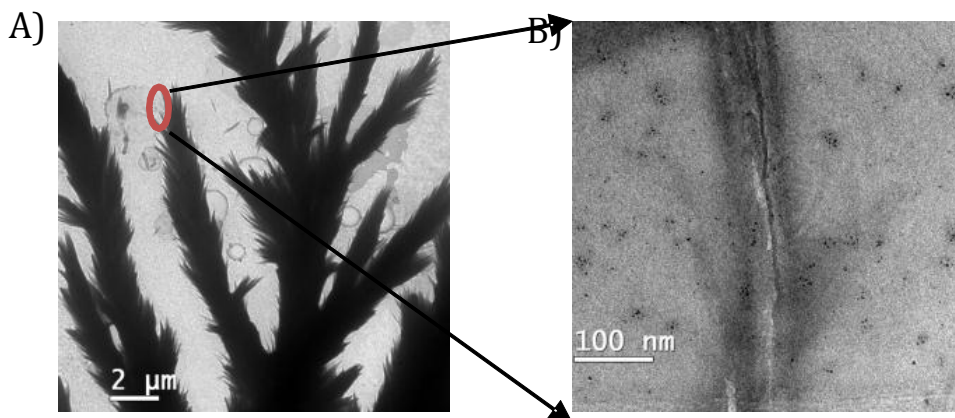he protein fibres into formation of longer fibres. At *ca.* 24 h of irradiation, we observed the fibres having dimensions of micrometers of *ca.* 18 ± 2 μm in length and *ca.* 2 ± 0.5 μm in diameter (Figure 2.12). Simultaneously, destruction of the ordered nanoparticles was observed, which sequentially knocked out of the fibre and clustered with an average size of *ca.* 5 ± 1 nm (Figure 2.12B).
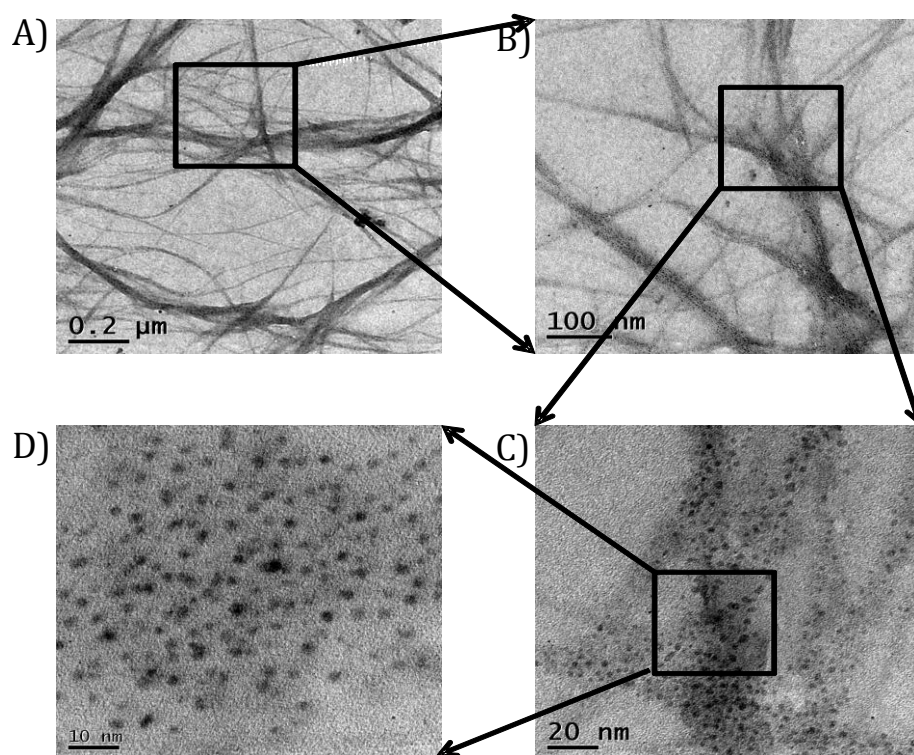
Figure 2.11. Transmission electron microscopic (TEM) images of A) 0.5% (w/v) of γ-globulin capped gold nanoparticles formed on the self-assembled protein fibres by irradiation at 350 nm for *ca.* 3 h. Magnified images (B, C and D) of the area marked by the black box in panel A, B and C respectively.

The negligible formation of the surface plasmon band during the initial irradiation times of less than 12 h could be attributed to the formation of smaller nanoparticles of size *ca.* 2-2.5 nm as evidenced through TEM analysis. The evolution of the surface plasmon resonance band centred at around 520 nm with the increase in the irradiation time further supports the fact that initially formed nanoparticles

Figure 2.12. A) Transmission electron microscopic (TEM) images showing the formation of long protein fibres and sequential knockout of gold nanoparticles after 24 h irradiation of a solution containing 0.5% (w/v) of γ-globulin plus $HAuCl_4$ (2 mM) at pH 12 with a light source of 350 nm. B) Magnified image of the marked oval area of the panel A.

transform into bigger particles of size around 5 nm, since the observation of surface plasmon resonance band is a signature of the metal nanoparticle.[22] The initial observation of an intense red emission having maximum at *ca.* 680 nm along with a less prominent band at 450 nm confirms the fact that the size of the arrayed gold nanoparticles was very small and of the order of *ca.* 2-2.5 nm. However, when the irradiation period was increased to 24 h, the emission at 680 nm was found to be

significantly quenched, albeit with negligible changes in the emission intensity at 450 nm.

From the microscopic data, it was clear that when the 0.5% γ-globulin containing gold salt solution at pH 12 irradiated for 3 h resulted in fibrillar network of the protein with arrayed gold nanoparticles. The time-dependent microscopic investigations showed that the increase in the irradiation resulted in hierarchical assembly of the fibrillar network of the protein with arrayed gold nanoparticles leading to the formation of micrometer long fibre, wherein pH of the solution was found to play a crucial role in the protein aggregation. These observations clearly indicate that the emission at 680 nm was mainly due to the fact that in the initial state, the particles bound to the fibres were very small (<5 nm) having negligible surface resonance plasmon band but possess prominent red emission.[23,24] While during the fibrillar growth of the protein, the particles get clustered with evolution of the surface resonance plasmon band and prominent quenching of emission intensity at 680 nm. These changes in the photophysical properties observed were coherent with the time dependent changes observed in the alignment of the ordered nanoparticles and self-assembly of the protein. Moreover, when we have done the morphological analysis of the γ-globulin alone in the absence of $HAuCl_4$ under similar experimental conditions, we could observe the formation of the protein nano fibres. Furthermore, with the increase in irradiation time, we observed the transformation of the initially formed short self-assembled γ-globulin fibres to the long fibres as evidenced through TEM analysis (Figure 2.13).
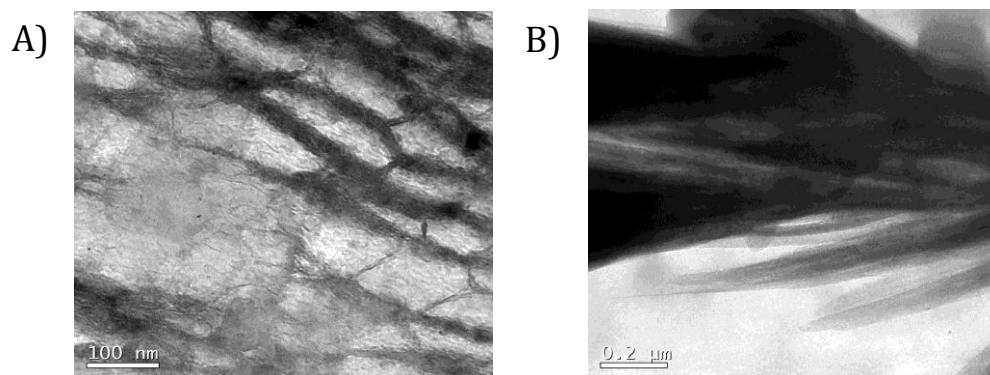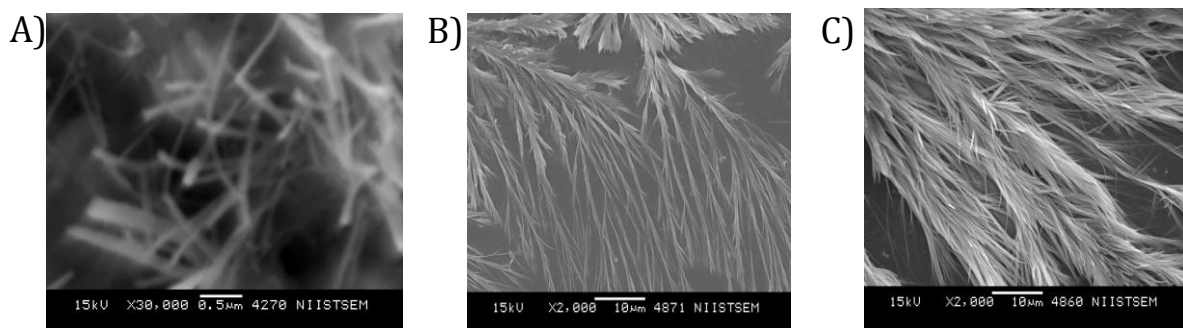
Figure 2.13. TEM images of the protein fibres in the absence of AuNPs, after A) 6 h and B) 24 h irradiation with 350 nm light source.

To further evidence the morphological transformations, we have employed other microscopic techniques and analyzed the samples under different conditions. Figure 2.14 shows the AFM images of 0.5% (w/v) γ-globulin-AuNPs irradiated for *ca.* 3-24 h at pH 12. As in the case of TEM analysis, the AFM analysis of samples after an irradiation period of 3 h, we observed the formation of small protein fibres of *ca.* 20 ± 5 nm. Further irradiation of these small protein fibres resulted in their self-assembly and finally, we observed well developed micrometer long protein fibres of *ca.* 18 ± 2 μm. Similar results were obtained from SEM analysis, wherein we initially observed the small fibres, which bundled to form micrometer length long protein fibres after longer periods of irradiation (Figure 2.15). Unfortunately, the initially formed regular small fibril like structures of the γ-globulin with ordered array of gold nanoparticles couldn't be clearly visualized in the AFM and SEM images since the average size of these nanoparticles was between 2-2.5 nm.
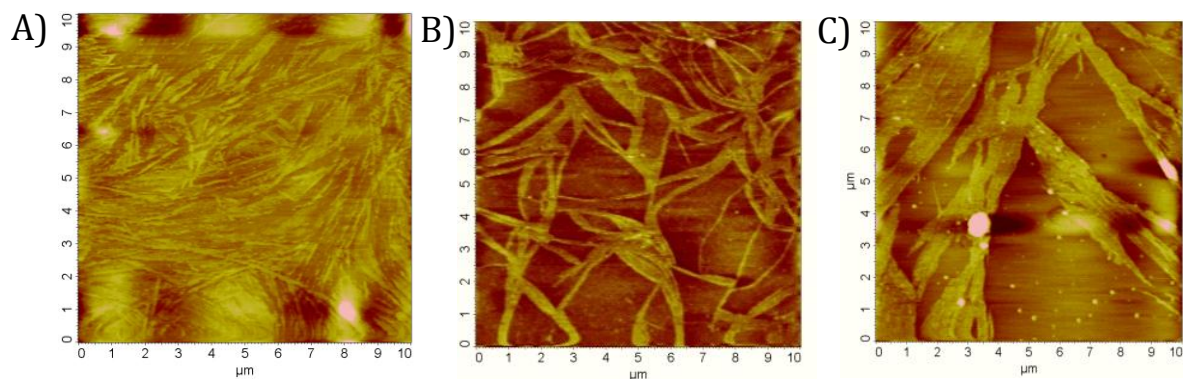
Figure 2.14. Atomic force microscopic (AFM) images showing the different stages of the growth of the protein fibres after irradiation of a solution containing 0.5% (w/v) of γ-globulin plus $HAuCl_4$ (2 mM) at pH 12 with a light source of 350 nm. Irradiation time, A) 3 B) 12 and C) 24 h.

Figure 2.15. Scanning electron microscopy (SEM) images showing the different stages of the growth of the protein fibres after irradiation of a solution containing 0.5% (w/v) of γ-globulin plus $HAuCl_4$ (2 mM) at pH 12 with a light source of 350 nm. Irradiation time, A) 3 B) 12 and C) 24 h.

2.3.4. Conductive AFM (C-AFM) Study of the Bioconjugates

To understand conducting properties, the electrical transport characteristics of these fibres with and without the alignment of nanoparticles were measured using conductive probe atomic force microscopy (C-AFM). Since the gold

nanoparticles were encapsulated within the protein matrix, the interparticle distance was found to be close enough to transfer electrons through the protein matrix. The *I-V* responses at different positions of the image was measured and the representative *I-V* curves are shown in Figure 2.16. From this figure, it was clear that
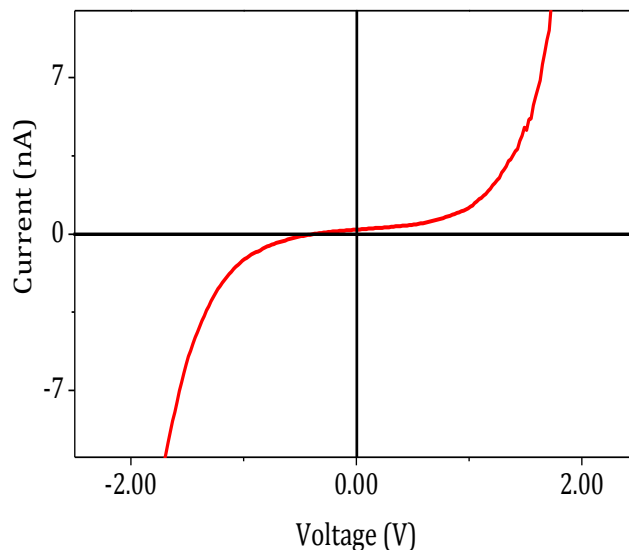
Figure 2.16. *I-V* curve obtained after irradiation for a period of 3 h of 0.5% (w/v) of γ-globulin plus $HAuCl_4$ (2 mM) at pH 12 with a light source of 350 nm obtained from the aqueous solution dropcasted on HOPG substrate.

during the initial period of irradiation, where the nanoparticles were aligned, the fibres exhibited conductivity in the range of semiconductors. This result clearly demonstrates the fact that the AuNPs aligned within the protein fibrils were able to mediate the transfer of electrons liberated by the enhanced third-order nonlinear susceptibility of AuNPs near their SPR frequency. After irradiation for longer hours (24 h), these fibres behaved almost like an insulator (Figure 2.17). This conductivity measurements gave further evidence for the ordering of nanoparticles on the

protein fibre in the initial state of photoactivation since light can be transported through the aligned nanoparticles of substantially smaller sizes.[6f,24c-d] The insulator behaviour of the *I-V* responses after 24 h irradiation also supports the fact that the nanoparticles thus were clustered out of the long fibres after longer periods of irradiation as characterized through microscopic techniques.
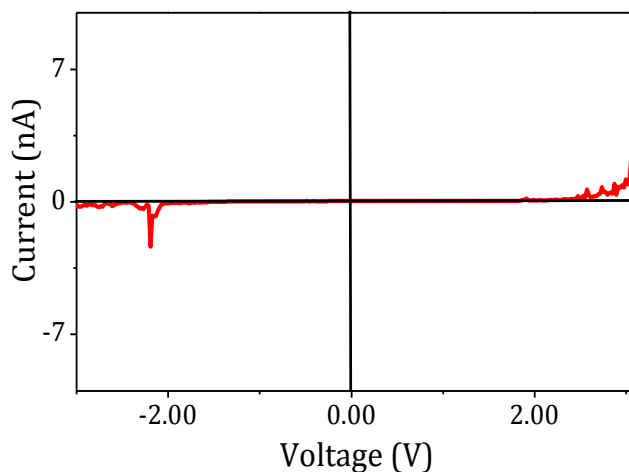
Figure 2.17. *I-V* curve obtained after irradiation for a period of 24 h of 0.5% (w/v) of γ-globulin plus $HAuCl_4$ (2 mM) at pH 12 with a light source of 350 nm obtained from the aqueous solution dropcasted on HOPG substrate.

2.3.5. Conformational Analysis of the Bioconjugates

With an aim to understand the protein conformational changes, we have investigated the chiroptic properties of γ-globulin-AuNPs system during different irradiation time intervals through circular dichroism (CD) spectroscopy. The CD experiments were performed at 25 °C and all the spectra were recorded between 190 and 350 nm at a rate of 50 nm/min. The CD spectrum of 0.5% (w/v) of γ-

globulin alone in the native state exhibited the characteristic CD response with a negative ellipticity at 218 nm (Figure 2.18).[26] However, after the irradiation for 24 h, we observed a red shift of *ca.* 18 nm and the protein displayed a negative CD signal at 236 nm. In contrast, when a solution of 0.5% (w/v) of γ-globulin containing 2 mM of $HAuCl_4$ at pH 12 was irradiated for 3 h, we observed both negative and positive CD signals at around 232 and 250 nm, respectively (Figure 2.19). On further irradiation for 12 h, we observed the decrease in intensity of *ca.* 66% and 27%, respectively, of both the negative and positive CD signals. Furthermore, after irradiation for 24 h, the CD spectrum of the solution showed a blue shift of *ca.* 5 nm of the negative signal, while the positive signal showed *ca.* 80% decrease in the
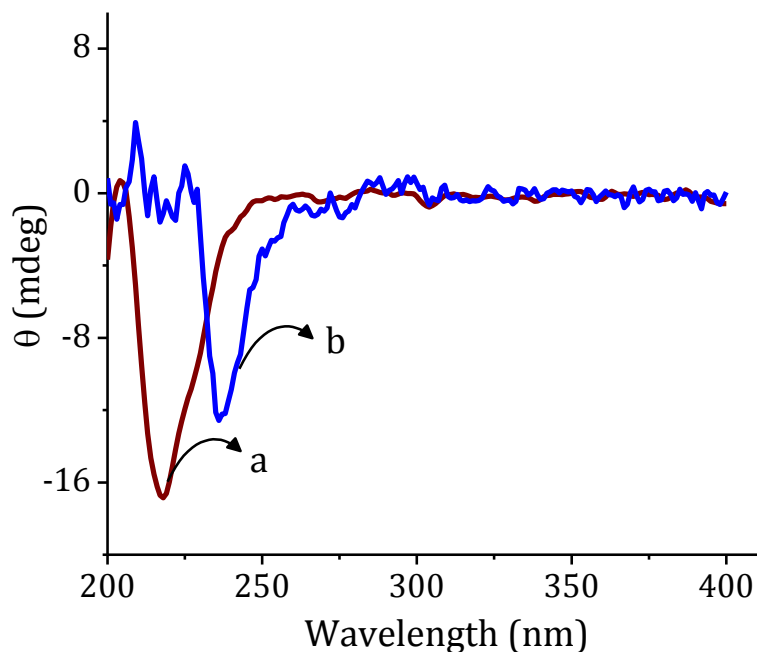
Figure 2.18. CD spectral changes of 0.5% (w/v) of γ-globulin in aqueous medium a) before irradiation and b) after irradiation for a period of 24 h.

intensity. The observed red shifted far UV-CD signal could be assigned to the antiparallel β-sheet structure on the basis of literature reports,[27,28] while the positive CD signal around 250 nm could be likely due to tertiary folding of the polypeptide chain.[29]
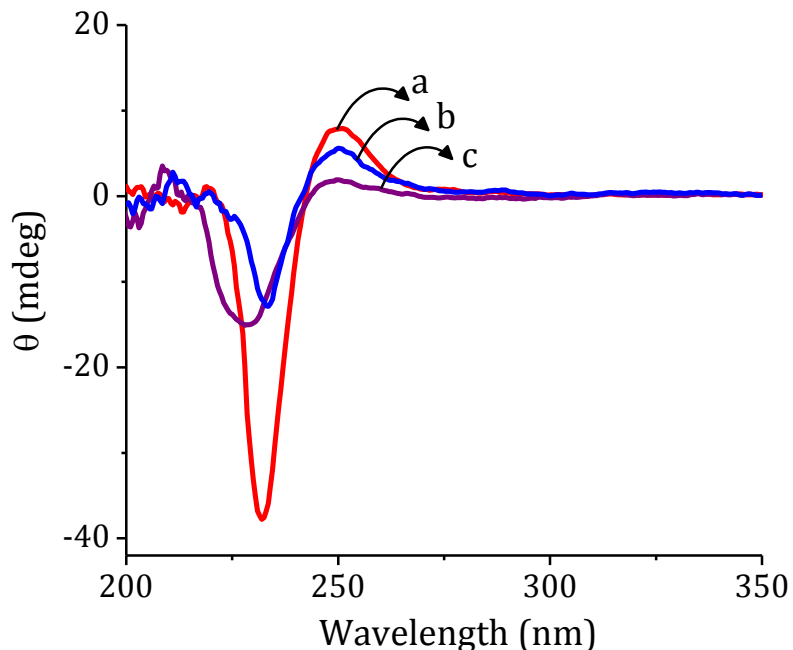
Figure 2.19. CD spectral changes during the protein fibre growth after photoirradiation of 0.5% γ-globulin capped gold nanoparticles in aqueous medium for a period of a) 3 b) 12 and c) 24 h with a light source of 350 nm.

Additional information for the observation of the protein conformational changes was obtained through fourier transform infrared (FTIR) spectroscopy. The FTIR spectrum of the solution containing 0.5% (w/v) of γ-globulin alone exhibited characteristic protein amide I and amide II bands at 1639 cm^{-1} and 1549 cm^{-1}, respectively. In contrast, when the protein alone was irradiated for 24 h, we

observed a red shift of *ca.* 58 cm^{-1} in the case of the amide I peak (1697 cm^{-1}), while

the amide II band showed a blue shift of *ca.* 3 cm^{-1} (1546 cm^{-1}). The FTIR analysis of

a solution containing 0.5% (w/v) of γ-globulin and HAuCl$_4$ showed smilar spectrum

as that of the protein alone in the dark. However, after irradiation of this solution for

3 h, we observed the amide I band at *ca.* 1698 cm^{-1} with a bathochromic shift of *ca.*

59 cm^{-1}, while the weak amide II band appeared at *ca.* 1545 cm^{-1} with a blue shift of

ca. 4 cm^{-1}. On further irradiation for 24 h, we observed both the amide bands I and II

at 1648 and 1501 cm^{-1}, respectively, thereby confirming the protein conformational

changes in accordance with the obseravations made through time-dependent

fluoroscence, CD and microscopic techniques. These results confirmed the fact that

there are secondary structure perturbations in the protein due to the array of gold

nanoparticles. The observation of an intense band for amide I region at 1639 cm^{-1}

Table 2.1. Data summarizing FTIR spectroscopic changes during the protein
fibrillar growth.

Protein irradiation conditions*	Amide I	Amide II
Protein alone at pH 12	1639 cm^{-1}	1549 cm^{-1}
Protein alone at pH 12 after 24 h irradiation	1697 cm^{-1}	1546 cm^{-1}
0.5 GLAN* after 3 h irradiation	1698 cm^{-1}	1545 cm^{-1}
0.5 GLAN* after 24 h irradiation	1648 cm^{-1}	1561 cm^{-1}

 *0.5 GLAN = 0.5 % γ-globulin gold nanoparticle conjugate, λ_{ex} = 350 nm.

for the protein alone indicate that the native globulin is in the β-sheet-rich conformation,[29] but on irradiation and in the presence of nanoparticles, it transformed to antiparallel β-sheet conformation as evidenced through the characteristic peak at 1698 cm^{-1} and literature reports.[29] The conformational change was further evidenced by the FTIR analysis of the solution, which was irradiated for 24 h, wherein we observed the shift of the amide I band to 1648 cm^{-1}, indicating thereby the reversal of the conformation to the β-sheet. These results clearly demonstrate that the self-assembly of the protein proceed through the conformational rearrangement from β-sheet to antiparallel β-sheet and random coiled conformations, which act as template for the ordering and annihilation of nanoparticles during the irradiation conditions.

A schematic representation showing the irradiation induced assembly of the AuNPs at pH *ca.* 12 could be clearly understood from Figure 2.20. The initial photoactivation of the γ-globulin in the presence of HAuCl$_4$ resulted in the nucleation of the gold nanoparticles. Further photoactivation of the solution for 3 h led to the formation of the protein fibres of *ca.* 20 ± 5 nm*,* which interestingly assisted the alignment of the colloidal gold nanoparticles of average diameter of *ca.* 2-2.5 nm. As evidenced through various microscopic and spectroscopic analysis, the further photoactivation of the solution for 24 h resulted in the growth of the initially self-assembled small protein fibres into micrometer long fibres of *ca.* 18 ± 2 μm. Such transformation resulted in the knock out of the aligned nanoparticles from the surface of the protein fibre and clustering of the nanoparticles outside the self
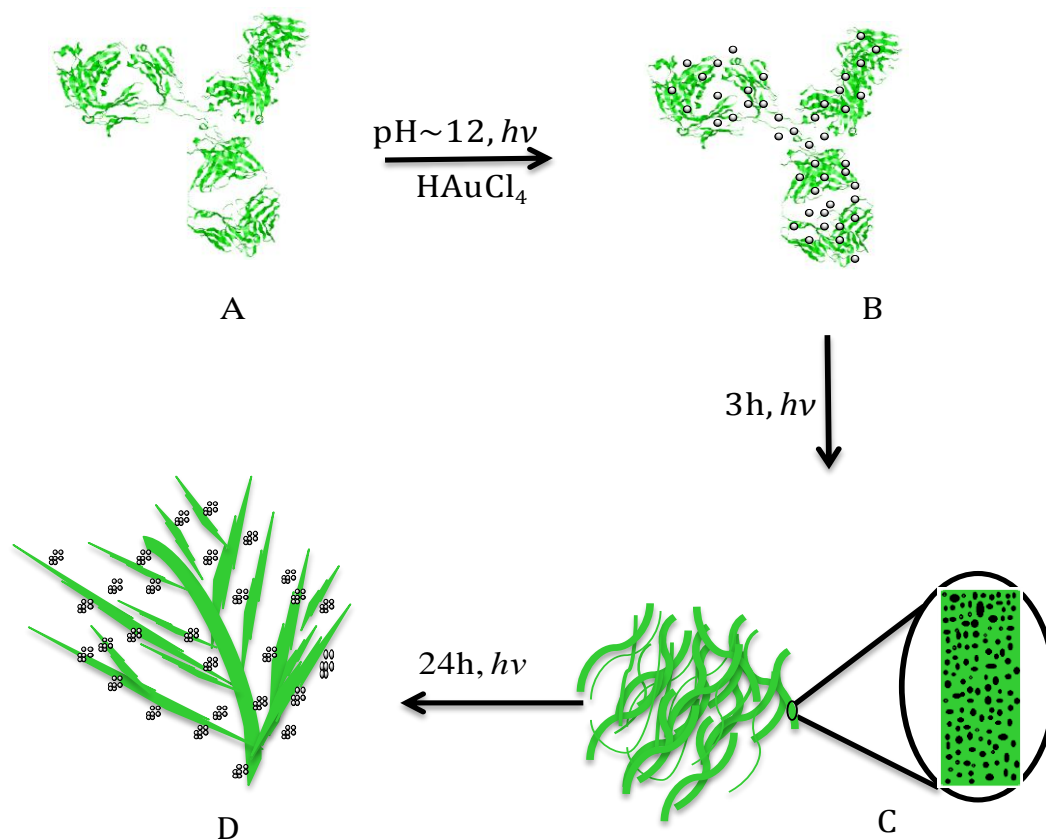
Figure 2.20. Schematic illustration of the hierarchical assembly process in the fibril formation A) protein (γ-globulin), B) nucleation & growth of AuNPs, C) alignment of the nanoparticles over the self assembled γ-globulin protein fibre and D) knocking out of the aligned nanoparticle from the γ-globulin fibre.

assembled protein fibre. The ascertained morphological changes that occurred during the photoactivation process can be likened to the naturally occurring photomorphogenesis. The entire process of photomorphogenesis proposed, consists of three successive phenomena *viz.,* generation, ordering, and sequential knock out of AuNPs from the γ-globulin protein fibre and which were predominantly controlled by the irradiation time dependent conformational changes of the protein.

2.4. CONCLUSION

In summary, the monodisperse biocompatible γ-globulin capped gold nanoparticles have been synthesized, wherein the protein acted as a capping, reducing as well as templating agent. Interestingly, γ-globulin when irradiated at pH 12 resulted in the self-assembly of the protein, which eventually grown into extended protein fibres of micrometer in length. We have further observed that the hierarchical assembly process plays a crucial role in aligning the nanoparticles and growth of the protein fibres causes the sequential knock out of the gold nanoparticles. Moreover, the observation of light triggered self-assembly of the protein and its effect on controlling the fate of the anchored nanoparticles can be compared with the naturally occurring process such as photomorphogenesis. Uniquely, our approach offers a way to understand the role played by the self-assembly of the protein, in particular γ-globulin in sequential ordering and knock out of the gold nanoparticles and also in the design of nano-biohybrid materials for medicinal and optoelectronic applications.

2.5. EXPERIMENTAL SECTION

2.5.1. General Techniques

The electronic absorption spectra were recorded on Shimadzu UV-3101 or -2401 PC UV/Vis/NIR scanning spectrophotometer. The fluorescence spectra were recorded on a SPEX-Fluorolog F112X spectrofluorimeter. IR spectra were recorded on a Perkin–Elmer Model 882 IR spectrometer. The pH measurements were carried

out using ELICO Model L1-120 digital pH meter, which was calibrated using standard buffer solutions of pH 4 and 9.2. CD spectra were obtained on a JASCO-J-810 Circular Dichroism Spectropolarimeter. Irradiation experiments were carried out using Rayonet Photochemical Reactor (RPR 350 nm). All experiments were carried out at room temperature (25 ± 10 °C), unless otherwise mentioned.

2.5.1.1. Transmission Electron Microscopy (TEM): TEM analysis was performed on JEOL 100 kV high resolution transmission electron microscope. A drop of nanoparticle solution was placed on the top of carbon-coated Cu grid. The grids were mounted on reverse tweezers and the samples were dried by a vacuum pump under reduced pressure for 1 h at room temperature. The accelerating voltage of the transmission electron microscope was 100 kV and the beam current was 65 A. Samples were imaged using a Hamamatsu ORCA CCD camera.

2.5.1.2. Scanning Electron Microscopy (SEM): SEM studies were carried out using ZEISS EVO MA and LS series scanning electron microscope. The operating range was between 100-230V at 50-60Hz single phase with a consumption of 2.5 kVA. The aqueous solution of the nanoparticle was drop casted directly on the top of the aluminium grid and the solvent was allowed to evaporate at ambient conditions. The obtained sample was coated with copper in order to attain the easy passage flow of electrons.

2.5.1.3. Atomic Force Microscopy (AFM): The AFM images were recorded under ambient conditions using a NTEGRA (NT-MDT) and operated with the use of tapping mode regime. Micro-fabricated TiN cantilever tips (NSG10) with a

resonance frequency of 299 kHz and a spring constant of 20-80 Nm^{-1} were used. AFM section analysis was done offline. Samples for the imaging were prepared by drop casting the solution of nanoparticle on freshly cleaved mica surfaces at the required concentrations and at ambient conditions.

2.5.1.4. Conductive Atomic Force Microscopy (C-AFM): The conductive atomic force studies have been done by using tapping mode to image protein-nano particle conjugate with a resonance frequency of 299 kHz and a spring constant of 20-80 Nm^{-1}. Micro-fabricated diamond coating was doped with nitrogen cantilever tips (DSP11) and employed an operator-activated external circuit to switch to contact mode for point contact electrical characterization of the selected positions. After completion of the measurement, we have deactivated the external circuit to prevent the damage of the protein fibres. Samples for imaging and electrical properties were prepared by drop casting the sample on HOPG at required concentrations at ambient conditions.

2.5.1.5. Dynamic Light Scattering Experiments (DLS): The DLS study of the nanoparticle solutions were carried out on a Nano Zeta Sizer, Malvern instruments. The samples were prepared in water at required concentrations. The light scattering experiments were performed under low polydipersity index by using glass cuvettes. The hydrodynamic diameters and polydisperse indices of the nanoparticles were determined using a Malvern Zeta Nano-ZS system.

2.5.1.6. Optical Polarized Microcopy (OPM): The optical polarized microcopy was performed using NikonHFX35A Optiphot-2 polarized-light optical

microscope, equipped with a Linkam THMS 600. For this analysis, the samples of nanoparticles were prepared in water. We drop casted the samples on a fresh glass plates and evaporate at ambient conditions with an excitation wavelength of 360 nm. The morphological transformations were followed, monitored and the images were taken using a CCD camera attached to NikonHFX35A.

2.5.2. Materials

Tetrachloroaurate hydrate ($HAuCl_4$), and γ-globulin were purchased from Sigma Aldrich and were used as such without further purification. Doubly distilled water was used for all the studies.

2.5.3. Synthesis of Gold Nanoparticles

2.5.3.1. Thermal Synthesis of Gold Nanoparticles in Presence of γ-Globulin: Aqueous solution of hydrogen tetrachloroaurate hydrate (2 mM) was mixed with different concentrations of γ-globulin (w/v = 0.1, 0.2 and 0.5%) and was heated at 60 °C for 4 h (GLAu). The reaction was cooled to room temperature, filtered and ultra-centrifuged to remove the unbound proteins. The nanoparticles synthesized were further characterized through AFM, SEM, TEM and DLS analyses.

2.5.3.2. Synthesis of Gold Nanoparticles in Presence of γ-Globulin by Irradiation: Aqueous solution of hydrogen tetrachloroaurate hydrate (2 mM) was mixed with different concentrations of γ-globulin (w/v = 0.1, 0.2 and 0.5%) and subjected to irradiation (3 h-24 h) in quartz tubes using a Rayonet Photochemical

Reactor (RPR 350 nm). The resulting colloidal solutions were characterized using AFM, SEM, TEM and DLS analyses.

2.5.3.3. Synthesis of Gold nanoparticles by Irradiation and Changing the pH: In a typical experiment, 2 mM aqueous solution of hydrogen tetrachloroaurate hydrate (99.999%) was mixed with 0.5% (w/v) of γ-globulin. NaOH solution (0.5 mL, 1 M) was added drop-wise to the above mixture after 2 min with vigorous stirring and the mixture was irradiated using Rayonet Photochemical Reactor by using a light source of 350 nm. The color of the solution changed from light yellow to brown. The nanoparticles on the protein fibres synthesized were further characterized through AFM, SEM, TEM and OPM analyses at different time intervals.

2.6. REFERENCES

1.   a) R. Baron, B. Willner and I. Willner, *Chem. Commun.*, **2007**, 323; b) K. Boeneman, J. R. Deschamps, S. B. White, D. E. Prasuhn, J. B. Blanco-Canosa, P. E. Dawson, M. H. Stewart, K. Susumu, E. R. Goldman, M. Ancona and I. L. Medintz, *ACS Nano*, **2010**, *4*, 7253; c) C. Tamerler and M. Sarikaya, *ACS Nano*, **2009**, *3*, 1606; d) D. H. M. Dam, J. Lee, P. Sisco, D. Co, M. Zhang, M. R. Wasielewski and T. W. Odom, *ACS Nano,* **2012**, *6*, 3318.

2.   a) F. Westerlund and T. Bjornholm, *Curr. Op. Colloid Interface Sci.*, **2009**, *14*, 126; b) T. Suteewong, H. Sai, J. Lee, M. Bradbury, T. Hyeon, S. M. Gruner and U. Wiesner, *J. Mater. Chem.*, **2010**, *20*, 7807; c*)* P. V. Kamat, *J. Phys. Chem. B*, **2002**, *106*, 7729.

3.   a) L. Liu, W. Lee, R. Scholz, E. Pippel and U. Gosele, *Angew. Chem., Int. Ed.*, **2008**, *47*, 7004; b) K. Ariga, T. Mori and J. P. Hill, *Chem. Sci.*, **2011**, *2*, 195; c) Z. X. Lu, L. F. Wood, D. E. Ohman and M. M. Collinson, *Chem. Commun.*, **2009**, 4200.

4.   a) Z. Y. Tang and N. A. Kotov, *Adv. Mater.*, **2005**, *17*, 951; b) S. Kinge, M. C. Calama and D. N. Reinhoudt, *Chem. Phys. Chem.*, **2008**, *9*, 20; c) L. C. Palmer and S. I. Stupp, *Acc. Chem. Res.*, **2008**, *41*, 1674; d) Y. W. Kwon, C. H. Lee, D. H. Choi and J. I. Jin, *J. Mater. Chem.*, **2009**, *19*, 1353.

5.   a) C. Zhang, M. Su, Y. He, X. Zhao, P. A. Fang, A. E. Ribbe, W. Jiang and C. D. Mao, *Proc. Natl. Acad. Sci.*, **2008**, *105*, 10665; b) C. L. Chen and N. L. Rosi, *Angew. Chem. Int. Ed.*, **2010**, *49*, 1924; c) S. Sofia, S. S. Yajaira, S. M. Sonny and A. B. Carl, *Chem. Mater.*, **2008**, *20*, 821; d) G. J. Leggett, *Nanoscale*, **2012**, *4*, 1840.

6.   a) G. Shemer, O. Krichevski, G. Markovich, T. Molotsky, I. Lubitz and A. B. Kotlyar, *J. Am. Chem. Soc.*, **2006**, *128*, 11006; b) R. A. McMillan, J. N. Howard, J. Zaluzec, H. K. Kagawa, R. Mogul, Y. F. Li, C. D. Paavola and J. D. Trent, *J. Am. Chem. Soc.*, **2005**, *127*, 2800; c) R. P. Blakemore, *Annu. Rev. Microbiol.* **1982**, *36*, 217; d) E. Bauerlein, *Angew. Chem., Int. Ed.*, **2003**, *42*, 614.

7.   a) M. Sarikaya, C. Tamerler, A. K. Y. Jen, K. Schulten and F. Baneyx, *Nat. Mater.* **2003**, *2*, 577; b) I. Lynch and K. A. Dawson, *Nano Today*, **2008**, *3*, 40; c) J. Klein, *Proc. Natl. Acad. Sci. U.S.A.*, **2007**, *104*, 2029.

8.   a) C. Branden, and J. Tooze, Garland Publishing, Inc., New York, **1991**; b) J.S. Richardson, *Adv. Prot. Chem.*, **1981**, *34*, 167; c) D. A. Dougherty, *Curr. Opin.*

Chem. Biol., **2000**, 4, 645; d) J.P. Greenstein and M. Winitz, *Chemistry of the amino acids*, 3 Vols, John Wiley & Sons, New York, **1961**.

9. a) R. Rica and H. Matsui, *Chem. Soc. Rev.*, **2010**, *39*, 3499; b) M. Sachiko, U. Shinobu and M. Hisakazu, *Mol. BioSyst.*, **2005**, *1*, 146; c) K. T. Nam, Y. J. Lee, E. M. Krauland, S. T. Kottmann and A. M. Belcher, *ACS Nano*, **2008**, *2*, 1480; d) M. Li, E. Dujardinb and S. Mann, *Chem. Commun.*, **2005**, 4952.

10. X. Y. Fu, Y.Wang, L. X. Huang, Y. L. Sha, L. L. Gui, L. H. Lai and Y. Q. Tang, *Adv. Mater.*, **2003**, *15*, 902

11. M. S. Lamm, N. Sharma, K. Rajagopal, F. L. Beyer, J. P. Schneider and D. J. Pochan, *Adv. Mater.*, **2008**, *20*, 447.

12. a) N. Sharma, A. Top, K. L. Kiick and D. J. Pochan, *Angew. Chem.*, **2009**, *121*, 7212; b) L. S. Li and S. I. Stupp, *Angew. Chem.*, **2005**, *117*, 1867; c) C. L. Chen and N.L. Rosi, *Angew. Chem.*, *Int. Ed.*, **2010**, *49*, 1924.

13. a) D. Zhang, O. Neumann, H. Wang, V. M. Yuwono, A. Barhoumi, M. Perham, J. D. Hartgerink, P. Wittung-Stafshede and N. J. Halas, *Nano Lett.*, **2009**, *9*, 666; b) S. Bolisetty, J. J. Vallooran, J. Adamcik, S. Handschin, F. Gramm and R. Mezzenga, *J. Colloid Interface Sci.*, **2011**, *361*, 90; c) M. Mahmoudi, H. R. Kalhor, S. Laurent and I. Lynch, *Nanoscale*, **2013**, *5*, 2570.

14. a) M. G. Ryadnov and D. N. Woolfson, *J. Am. Chem. Soc.*, **2004**, *126*, 7454; b) T. O. Yeates and J. E. Padilla, *Curr. Opin. Struct. Biol.*, **2002**, *12*, 464; c) C. M. Niemeyer, *Angew. Chem. Int. Ed.*, **2001**, *40*, 4128; d) J- M. Jung, G. Savin, M. Pouzot, C. Schmitt and R. Mezzenga, *Biomacromolecules*, **2008**, *9*, 2477; e) A.

Altunbas, N. Sharma, M. S. Lamm, C. Yan, R. P. Nagarkar, J. P. Schneider and D. J. Pochan, *ACS Nano*, **2010**, *4*, 181.

15. a) S. Srivastava and N. A. Kotov, *Soft Matter*, **2009**, *5*, 1146; b) J. Yuan, Y. Xub and A. H. E. Muller, *Chem. Soc. Rev.*, **2011**, *40*, 640; c) C. M. Niemeyer, *Angew. Chem. Int. Ed.*, **2003**, *42*, 5766; c) B.Zhang, W. Zhao and D. Wang, *Chem. Sci*. **2012**, *3*, 2252.

16. a) Y. Ofir, B. Samanta and V. M. Rotello, *Chem. Soc. Rev.*, **2008**, *37*, 1814; b) E. Katz and I. Willner, *Angew. Chem. Int. Ed,* **2004**, *43*, 6042; c) S. G. Penn, L. He and M. J. Natan, *Curr. Opin. Chem. Biol.*, **2003**, *7*, 609.

17. a) P. Alivisatos, *Nat. Biotechnol.*, **2004**, *22*, 47; b) M. Grzelczak, J. Vermant, E. M. Furst and L. M. Liz-Marźan, *ACS Nano*, **2010**, *4*, 3591; c) S. I. Lim and C. J. Zhong, *Acc. Chem. Res.*, **2009**, *42*, 798; d) N. Sharma, A. Top, K. L. Kiick and D. J. Pochan, *Angew. Chem. Int. Ed.*, **2009**, *48*, 7078; e) L. Hu, Y. Sun and Y. Wu *Nanoscale*, **2013**, *5*, 3103.

18. S. Dubiski, A. Dubiska, D. Skalba and A. Kelus, *Immunology*, **1961**, *4*, 236.

19. H. Huang and X. Yang, *Biomacromolecules*, **2004**, *5*, 2340.

20. J. Polte, T. T. Ahner, F. Delissen, S. Sokolov, F. Emmerling, A. F. Thunemann and R. Kraehnert, *J. Am. Chem. Soc.*, **2010**, *132*, 1296.

21. H. Qian, Y. Zhu and R. Jin, *Proc. Natl. Acad. Sci. U.S.A.*, **2012**, *109*, 696.

22. a) C. Burda, X. Chen, R. Narayanan and M. A. El-Sayed, *Chem. Rev.*, **2005**, *105*, 1025; b) Y. Negishi, K. Nobusada and T. Tsukuda, *J. Am. Chem. Soc.,* **2005**, *127*, 5261.

23. a) K. Chaudhari, P. L. Xavier and T. Pradeep, *ACS Nano*, **2011**, *5*, 8816; b) C. Zhou, C. Sun, M. Yu, Y. Qin, J. Wang, M. Kim and J. Zheng, *J. Phys. Chem. C,* **2010**, *114*, 7727; c) M. Quinten, A. Leitner, J. R. Krenn and F. R. Aussenegg, *Opt. Lett.*, **1998**, *23*, 1331; d) L. Yujing, G. Stefanic, J. Rathousky, O. Hayden, T. Bein and D. Fattakhova-Rohlfing, *Chem. Sci.*, **2012**, *3*, 2367; e) C. Feldmann, *Nanoscale*, **2011**,*3*, 1947.

24. a) D. G. Wickens, A. G. Norden, J. Lunec and T. L. Dormandy, *Biochim. Biophys. Acta,* **1983**, *742*, 607; b) A. F. Jones and J. Lunec, *Br. J. Cancer*, **1987**, *55*, 60.

25. A. Vermeer, M. Bremer and W. Noede, *Biochim. Biophys. Acta*, **1998**, *1*, 1425.

26. a) M. G. Ryadnov and D. N. Woolfson, *J. Am. Chem. Soc.*, **2005**, *127*, 12407; b) G. Liu, A. Prabhakar, D. Aucoin, M. Simon, S. Sparks, K. J. Robbins, A. Sheen, S. A. Petty and N. D. Lazo, *J. Am. Chem. Soc.*, **2010**, *132*, 18223.

27. H. A. Lashuel, S. R. LaBrenz, L. Woo, L. C. Serpell and J. W. Kelly, *J. Am. Chem. Soc.*, **2000**, *122*, 5262.

28. S. M. Kelly and N. C. Price, *Current Protein and Peptide Science*, **2000**, *1*, 349.

29. S. Chakraborty, P. Joshi, V. Shanker, Z. A. Ansari, S. P. Singh and P. Chakrabarti, *Langmuir*, **2011**, *27*, 7722.

STUDY OF INTERACTION OF SQUARAINES WITH PROTEINS AND THEIR USE AS ANTI-AMYLOID AGENTS
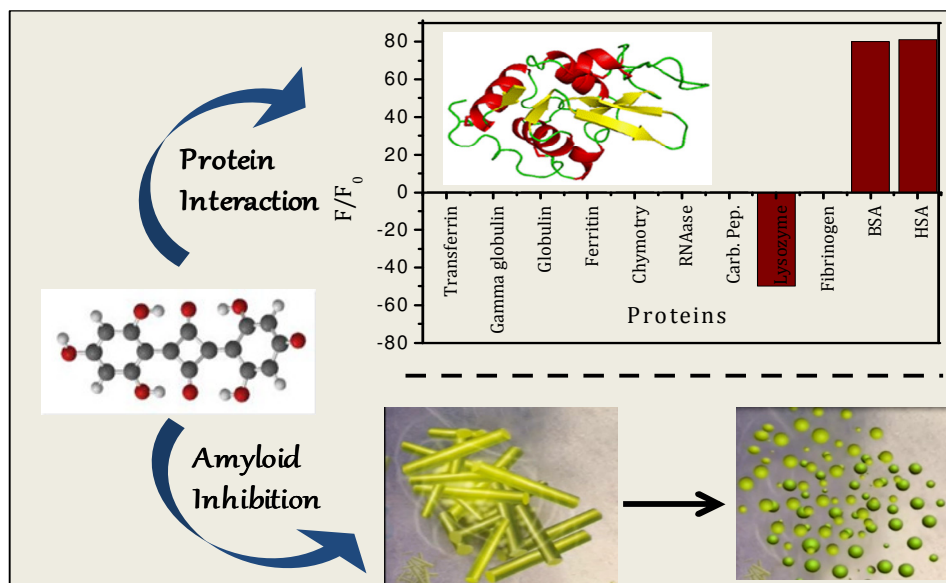
3.1. ABSTRACT

With a view to develop novel protein labeling agents, we have investigated the interactions of polyhydroxyl substituted squaraine dyes **1**-**3** with lysozyme and its amyloids through various photophysical and biophysical techniques. These dyes showed good solubility in the aqueous medium and exhibited favorable photophysical properties. The study of their interactions with various proteins revealed that the dyes **1**-**3** exhibited unique interactions with lysozyme in addition to serum albumins. For example, the addition of lysozyme to a solution of the dye **1**

resulted in a hypochromicity of *ca.* 69% in the absorption spectra as well as significant quenching in the fluorescence intensity. Similar observation of hypochromicity of *ca.* 71% and *ca.* 49% was made with the dyes **2** and **3**, respectively. The half-reciprocal analysis of the absorption data and isothermal titration calorimetric (ITC) measurements gave a 1:1 stoichiometry for the complex formed between lysozyme and squaraine dyes with association constants (K_{ass}) in the range *ca.* 10^4-10^5 M^{-1}. We have determined the changes in the free energy (ΔG) for the complexation with the dyes **1**-**3** and the values are found to be -30.78, -32.31 and -28.58 kJ mol^{-1}, respectively. Furthermore, we observed a strong induced CD (ICD) signal corresponding to the squaraine chromophore in the case of the dyes **2** and **3** at 636 and 637 nm, confirming the complex formation. In contrast, the parent dye **1** showed negligible ICD. To investigate the potential of these dyes as anti-amyloid agents, we have investigated their interactions with amyloid fibers derived from lysozyme under different conditions. The titration of the dye **1** with amyloid fibers resulted in *ca.* 74% hypochromicity, while the halogenated dyes **2** and **3** showed hypochromicity *of ca.* 76% and *ca.* 68%, respectively. To quantify the binding affinities of the squaraine dyes **1**-**3** with amyloids, we have determined the association constants through isothermal calorimetry. We obtained the values in the range *ca.* 1.2-3.6 × 10^5 M^{-1}. Uniquely, the inhibition of the amyloid fibers by **1**-**3**, was confirmed through thioflavin assay, ITC, CD, AFM, TEM as well as SAED experiments. These results indicate that the squaraine dyes **1**-**3**, under investigation, can act as efficient protein labeling agents as well as anti-amyloid agents.

3.2. INTRODUCTION

The proteins are nitrogen-containing organic compounds that are the basic units of living systems. These macromolecules contain amino acid monomeric units, which are joined by peptide linkages.[1] A protein, often has, multiple stable conformations, and can undergo conformational changes when they bind to other proteins and substrates.[2] The proteins are classified into primary, secondary, tertiary, and quaternary structures and these structures determine their different functions. The order of amino acids in the protein molecule determines its primary structure.[3] The secondary structure of the protein results from folding of the polypeptide chains having maximum number of hydrogen bonds. The most common secondary structures are the α-helix, β-conformation, and β-turns. The tertiary structure of the protein on the other hand is formed by the twisting of α-helices into specific shapes and these structures are stabilized by multiple weak interactions like hydrophobic interactions, hydrogen bonding and ionic interactions. When two or more protein molecules consisting of separate polypeptide chains interact with each other result in a quaternary structure. Based on their functions, the proteins can be classified into different groups. Some of these include enzymes, hormones, transport, structural, motor, receptors, signaling and storage proteins.

The study of protein-ligand interactions has been emerged as an active area of research. The proteins are dynamic molecules whose functions depend on its interactions with other molecules.[2-5] Major forces for the protein ligand binding are

a) Primary structure
b) Secondary structure
c) Tertiary structure
d) Quarternary structure
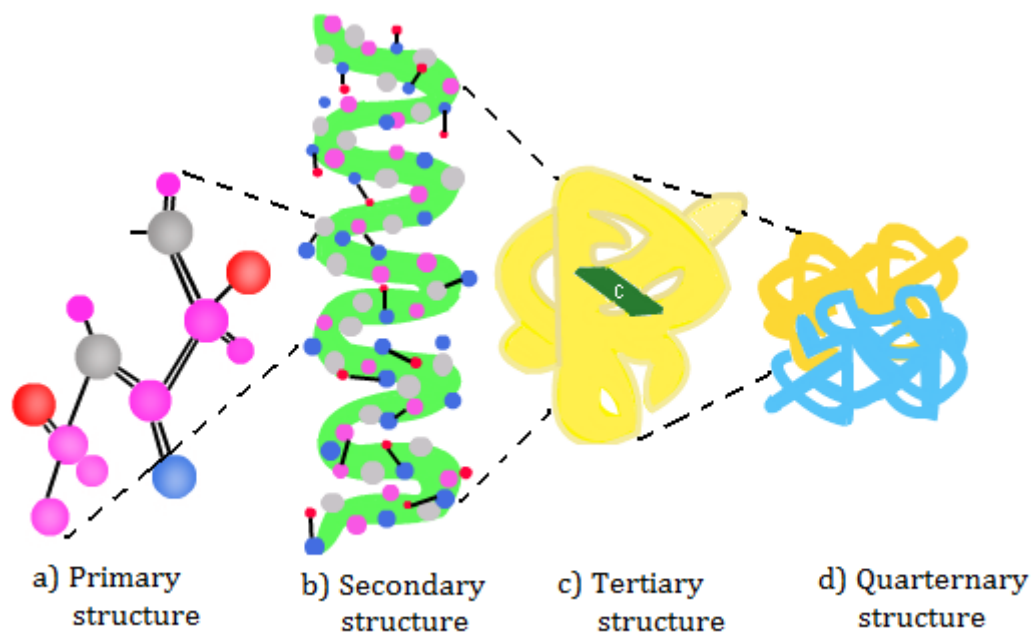
Figure 3.1. Cartoon representation showing primary, secondary, tertiary, and quaternary structures of the protein.

the H-bonding, van der Waals, disulphide bonding and the hydrophobic interactions.[6,7] Furthermore, the protein interaction is specific, since it can discriminate among the thousands of different molecules. The protein-ligand interactions are important in biological processes such as enzyme-substrate recognition, hormone action, signal transduction, and cell communication.[8-11] For example, the binding of cyanide to cytochrome inhibits its function, which is an integral part of the electron transport system in respiration.

The amyloid fibrillation of the proteins has been regarded as the hallmark of a large variety of debilitating disorders such as Creutzfeld-Jakob, Alzheimer's, Parkinson's disease as well as type II (non-insulin dependent) diabetes.[12,13] Among

the various proteins, lysozyme is a protein that readily undergoes the fibrillogenesis process and has been used as an excellent model for studying the protein amyloidogenesis.[14] The amyloid fibrils of lysozyme are formed at acidic pH and elevated temperatures, where a partially folded molten globule state gets populated.[14c] The basic structure of the amyloid fibrils is long and often twisted, a few nanometers in diameter, and predominantly composed of cross β-sheets and hence designated as β-amyloid.[13] The β-amyloid aggregation disrupts the brain cells by clogging points of cell-to-cell communication and activates the immune cells that trigger inflammation and devour disabled cells, and, ultimately, causing cell death.[14,15] Therefore, the sensitive detection and inhibition of the β-amyloid fibers is challenging and inhibition of the amyloid deposition with small organic molecules is of a great therapeutic value.

In this context, we have investigated the interaction of the squaraine dyes **1**-**3** (Chart 3.1) with lysozyme and its amyloids with an objective to evaluate their potential as anti-amyloid agents. Squaraines form a novel class of dyes which contain two donor moieties (D) connected to a central C_4O_2 electron withdrawing group (A) forming a donor-acceptor-donor (D-A-D) system.[16-18] The intramolecular charge transfer character of the S_0-S_1 transition combined with an extended π-electron network, gives rise to the observed sharp and intense bands in the visible to infrared region for these dyes.[19-22] We chose these dyes because they are known to interact with BSA and HSA and signal the binding event through 'visual color' change and 'turn on' fluorescence intensity as reported earlier.[22] These dyes showed unique

interactions with lysozyme as determined through the observation of hypochromicity in the absorption spectra and significant quenching in the fluorescence intensity. We have further investigated the interaction of these dyes with amyloids derived from lysozyme through various photophysical and biophysical techniques. These results demonstrate that the squaraine dyes **1**-**3**, under investigation, efficiently destabilized the amyloid fibers indicating thereby their potential as anti-amyloid agents.
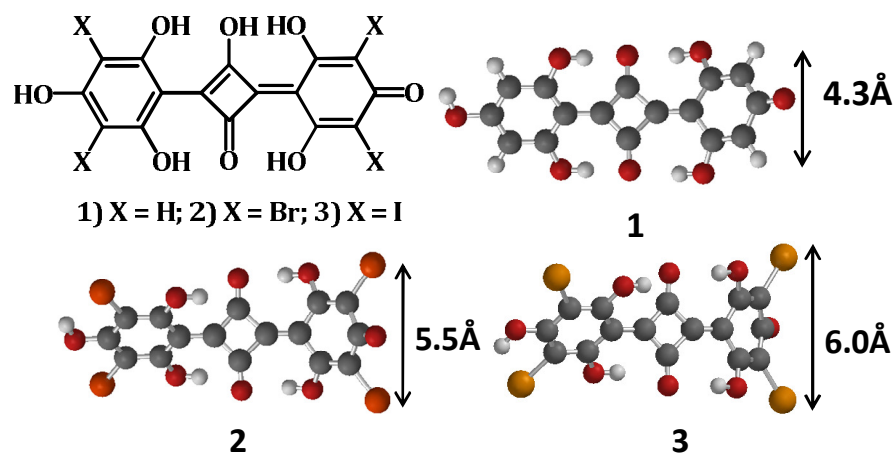
Chart 3.1

3.3. RESULTS AND DISCUSSION

3.3.1. Synthesis and Photophysical Properties

The synthesis of the squaraine dyes **1**-**3**, was achieved as per the reported procedure shown in Scheme 3.1. The squaraine dye **1** was prepared in *ca.* 67% yield by the reaction of phloroglucinol with squaric acid.[21] Subsequently, the dye **1** was

halogenated with bromine or iodine monochloride in acetic acid at 50 °C to give the dyes **2** and **3** in *ca.* 80% and 71% yields, respectively. These dyes **1-3** existed in solution in the protonated, neutral, singly deprotonated or doubly deprotonated forms, depending on the pH of the solution.[21] Figure 3.2 shows the absorption and emission spectra of the singly deprotonated form of the squaraine dyes **1-3** in 2% ethanol buffer.
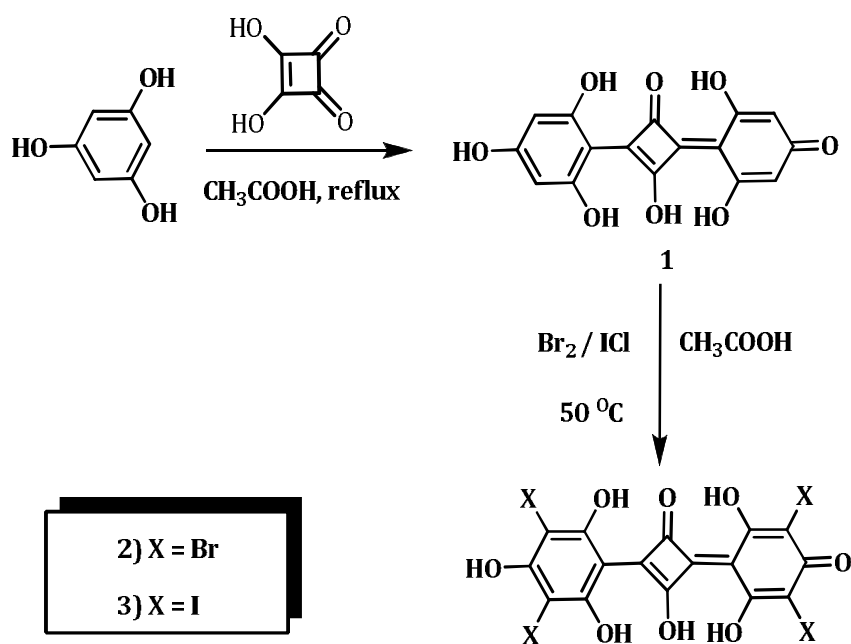
Scheme 3.1. Synthesis of the squaraine dyes **1**, **2** and **3**.

The singly deprotonated forms of the dyes **1-3** showed relatively intense sharp bands at 584, 610 and 613 nm, respectively, wherein the absorption maxima of the dyes **2** and **3** were red shifted by about 26-29 nm, as compared to **1**.[21c] Inset of Figure 3.2 shows the emission spectra of the singly deprotonated forms of the dyes **1-3** in 2% ethanol-buffer mixture. The emission maximum of the iodo derivative **3**,

showed a bathochromic shift of 9 nm, as compared to **2**. The quantum yields of fluorescence (Φ_F) in 2% ethanol-buffer for **2** and **3** were determined and were found to be lower than **1**. The decreased quantum yield values in the case of **2** and **3** can be attributed to the enhanced intersystem crossing efficiency due to the heavy atom effect in these cases.[29-32]
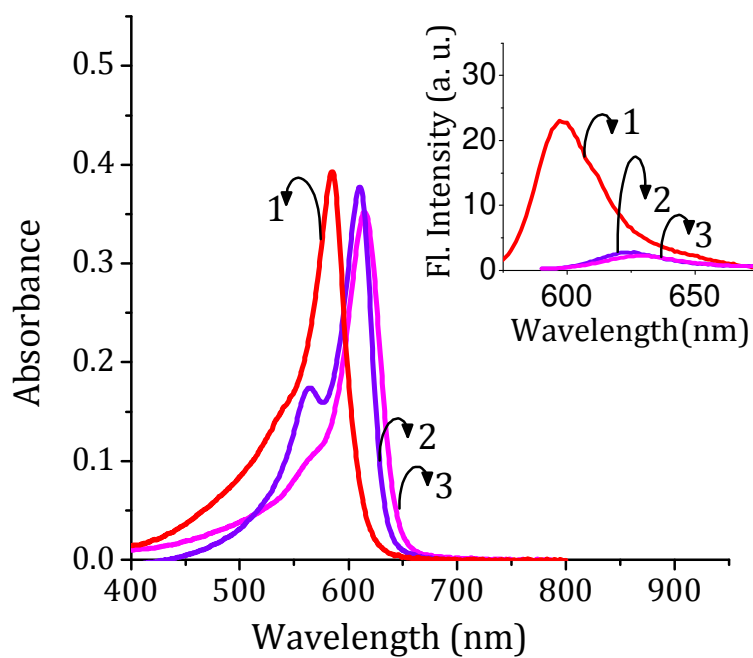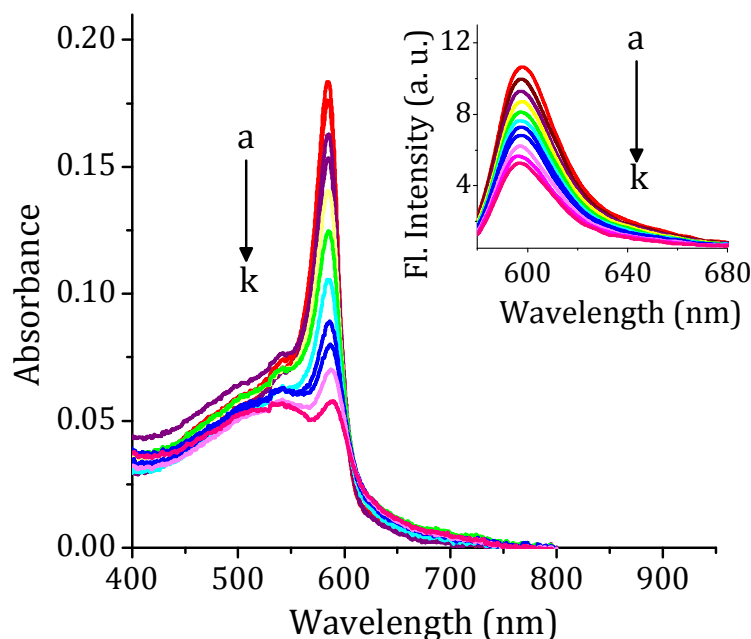

Figure 3.2. Absorption spectra of **1**-**3** in 2% ethanol-phosphate buffer mixture and the inset shows their corresponding emission spectra of **1**-**3**. Excitation wavelength, 560 nm for **1** and 575 nm for **2** and **3**.

3.3.2. Interaction of Squaraine Dyes with Lysozyme

The study of protein-ligand interactions is important in many biological processes and such effective systems can be exploited for the development of novel

therapeutic agents. In this context, we have investigated the interactions of the dyes **1**-**3** with lysozyme. We have monitored the changes in the absorption and emission spectra of these dyes with the addition of lysozyme in 2% ethanol-phosphate buffer. For example, Figure 3.3 shows the changes in the absorption spectra of **1** (1.3 μM) with increasing concentration of lysozyme (0-8 μM) in 2% ethanol-phosphate buffer at pH 8.4. We could observe a hypochromicity of *ca.* 69% in the absorbance of **1** at 584 nm with a red shift of ~ 4 nm. Similar observations have been made with the dyes **2** (Figure 3.4) and **3**, wherein a hypochromicity of *ca*. 71% and *ca*. 49% with a bathochromic shift of about *ca*. ~14-15 nm in the absorption spectra were observed

Figure 3.3. Changes in the absorption of **1** (1.3 μM) with increasing concentrations of lysozyme in 2% ethanol-phosphate buffer at pH 8.4 and the inset shows the corresponding emission changes. [lysozyme] a) 0 and k) 8 μM. Excitation wavelength, 560 nm.
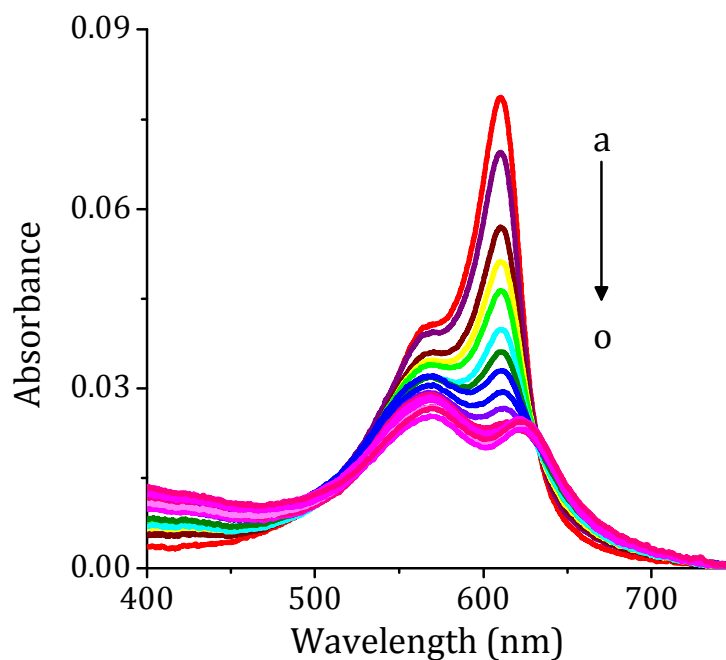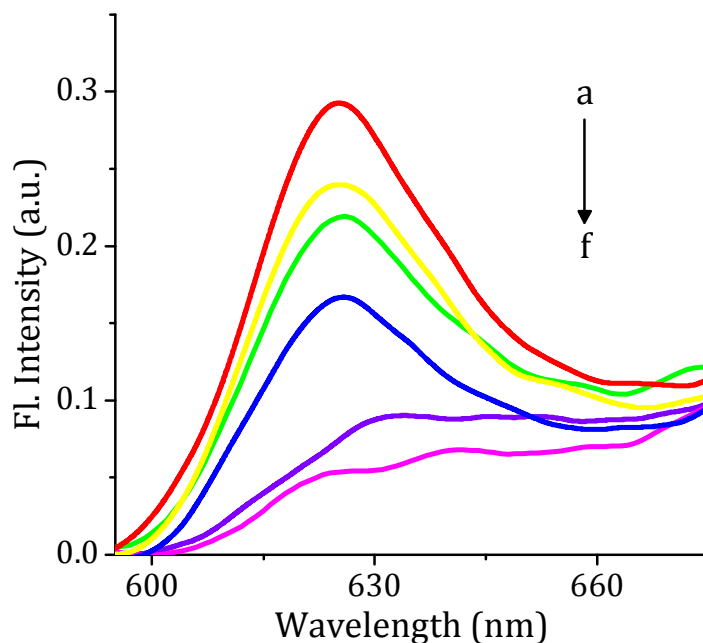
Figure 3.4. Changes in the absorption spectra of the dye **2** (1.6 μM) with increasing concentrations of lysozyme, [lysozyme] a) 0 and o) 8 μM in 2% ethanol-phosphate buffer at pH 6.4.

under similar experimental conditions. The fluorescence spectral changes were monitored with the increasing concentrations of lysozyme (Inset of Figure 3.3). We observed *ca.* 50% quenching in the fluorescence intensity of the dye **1** at 600 nm. Similar increasing lysozyme concentrations, resulted in the complete quenching of fluorescence intensity of both the dyes **2** (Figure 3.5) and **3**.

The photophysical properties of the singly deprotonated forms of **1**-**3** in the presence and absence of lysozyme are summarized in Table 3.1. These photophysical changes showed that the squaraines **1**-**3**, under investigation, showed efficient interaction with lysozyme to form a stable [squaraine.lysozyme] complex with significant association constants. In addition to lysozyme, we have investiagted

Figure 3.5. Changes in the emission spectra of **2** (1.6 μM) with increasing concentrations of lysozyme in 2% ethanol-phosphate buffer at pH 6.4. [lysozyme] a) 0 and f) 8 μM. Excitation wavelength, 575 nm.

the interactions with similar important proteins like BSA, HSA, ferritin, transferin, fibrinogen, lysozyme, carboxy peptidase A, ribonuclease A, bovine gamma globulin, gamma globulin and chymotrypsinogen. We have monitored the changes in the absorption and emission spectra of the dyes **1**-**3** with the addition of these different proteins. In contrast, to the interactions observed with lysozyme, BSA and HSA, the dyes **1**-**3** showed negligible interactions with all other proteins under similar conditions. For example, Figure 3.6 shows the relative changes in the fluorescence intensity of the dye **1** (1.3 μM) with the addition of 8 μM of different proteins. The observations made with BSA and HSA were reported in our earlier publications.[23a-b]

Table 3.1. Absorption and emission properties of the squaraine dyes **1-3** in the absence and presence of lysozyme in 2% ethanol-phosphate buffer.*

Dye	λ_{abs}, nm[a]	λ_{em}, nm[b]	Φ_F
1	584	600	0.140
[**1**.lysozyme]	588	600	0.011
2	610	625	0.018
[**2**.lysozyme]	624	c	c
3	613	634	0.006
[**3**.lysozyme]	628	c	c

*Average of more than two independent experiments. c, negligible fluorescence; Φ_F, quantum yields of fluorescence were determined by using cresyl violet as the standard; [a], absorption maximum; [b], emission maximum.
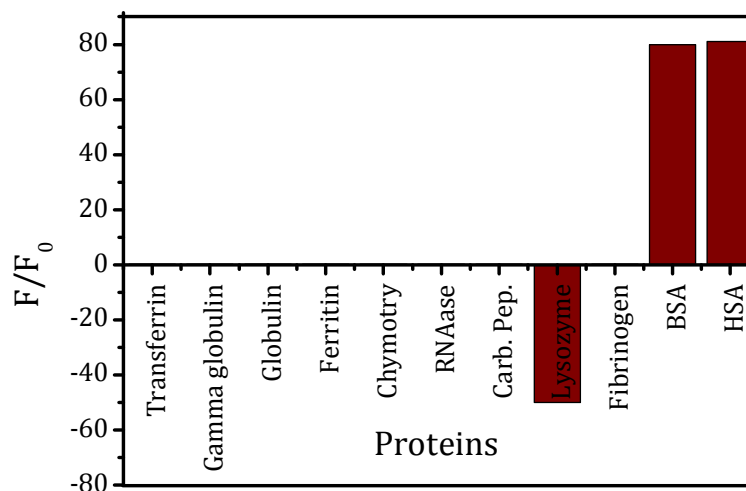
Figure 3.6. Relative changes in the fluorescence intensity of the dye **1** (1.3 μM) with the addition of selected proteins (0-8 μM) in 2% ethanol-phosphate buffer (pH 7.4). Excitation wavelength, 560 nm.

To elucidate the magnitude of the binding strength of these complexes, the intrinsic binding constants with lysozyme were determined using the titration data. The half-reciprocal analysis of the absorption data gave a 1:1 stoichiometry for the complex formed between lysozyme and squaraine dyes. For example, Figure 3.7 shows the binding analysis of **1** (1.3 µM) with increasing concentrations of lysozyme 0-8 µM. The binding constant for the complex between **1** and lysozyme was determined and the value is found to be K_{ass} = 2.7 x 10^5 M^{-1}. Similarly, the half-reciprocal analysis of the absorption titration data of **2** and **3** gave the binding constants of K_{ass} = 5.0 x 10^5 M^{-1} and 1.1 x 10^5 M^{-1}, respectively, indicating strong binding affinity of these dyes for lysozyme. The corresponding changes in the free
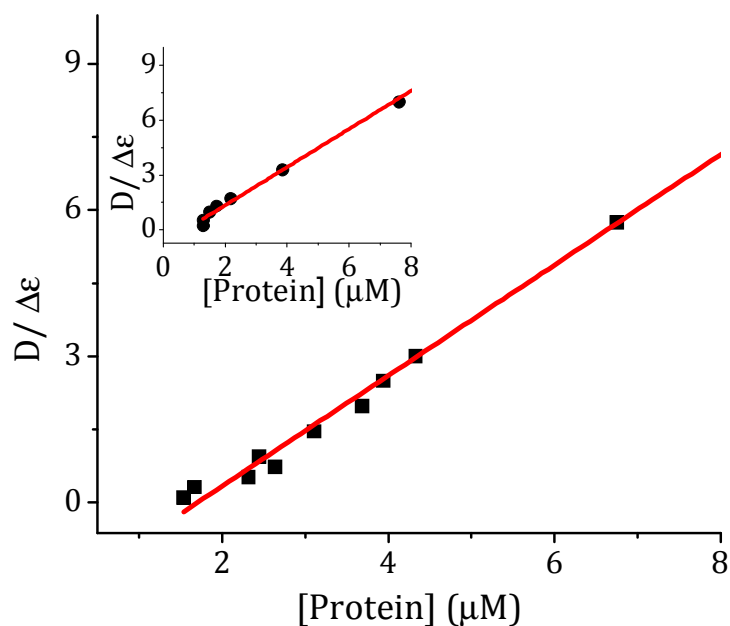
**Figure 3.7.** Half-reciprocal analysis of the absorption data for the binding of **1** (1.3 µM) with lysozyme. Inset shows the binding analysis for **3** (1.6 µM) with lysozyme. [lysozyme] 0-8 µM under similar conditions.

energy was estimated for the [**1**.lysozyme] complex and the values is found to be -30.78 kJmol^{-1}. Whereas, for [**2**. lysozyme] and [**3**. lysozyme] complexes, we obtained the values of *ca*. -32.31 kJmol^{-1} and -28.58 kJmol^{-1}, respectively.

3.3.3. Nature of Interaction of Squaraine Dyes with Lysozyme

To understand the nature of interaction of the squaraines **1**-**3** with lysozyme, we have carried out isothermal titration calorimetry (ITC) and circular dichroism (CD) studies. In addition, we have carried out the interaction studies with representative amino acids such as cysteine, L-lysine and glutamic acid, which are the major constituents of the side chain of lysozyme. Isothermal titration calorimetry (ITC) is a valuable tool to study the thermodynamics of interactions between proteins or peptides, with other ligands. With the gradual addition of lysozyme to the squaraine dyes **1**-**3** at 25 °C, we observed a regular exothermic response in the isothermal titration calorimetric (ITC) measurements. For example, Figure 3.8 shows the ITC titration curve for **1** (0.01mM) with lysozyme (0.1 mM). After the addition of 0.1 mM of lysozyme, we observed saturation in the heat change. A similar standard titration curves were obtained for the dyes **2** and **3**, which was fitted using a single binding site model. The association constants were determined and the values are found to be *ca.* 2.2 × 10^5 M^{-1}, 3.2 × 10^5 M^{-1}, and 1.2 × 10^5 M^{-1} for **1**, **2** and **3**, respectively. These values are in agreement with the association constants calculated from the half reciprocal analysis obtained from the absorption changes. The changes in free energy for the complexation also was determined based on ITC

data and the values are found to be -27.9 kJmol^{-1} for **1**, whereas for **2** and **3**, we observed the free energy change of -28.7 kJmol^{-1} and -26.6 kJmol^{-1}, respectively. These results confirm that there is an effective interaction between the squaraine dyes **1**-**3** and lysozyme resulting in the formation of stable complexes.
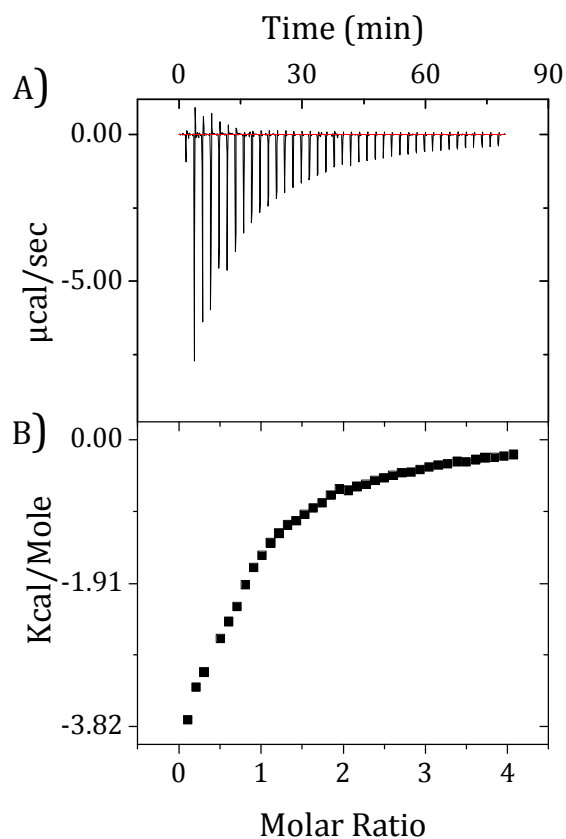
Figure 3.8. ITC titration of **1** (0.01mM) with lysozyme (0.1mM) in 0.1% ethanol-phosphate buffer, pH 8.4. A) Differential power recorded in the experiment; B) Integration of areas under peaks corresponding to the amount of heat released upon the addition of lysozyme to **1** as a function of the molar ratio.

Circular dichroism studies are useful in understanding the complex formation of organic ligands in a chiral environment. The binding of small achiral

molecules with the proteins has been well known to result in induced CD (ICD) signal in the absorption region corresponding to the bound ligand. In other words, ICD occurs when the achiral guest is encircled by a chiral host. The squaraine dyes under investigation alone, being achiral, did not give any CD signal. When the squaraine dye **1** (15 µM) interacted with lysozyme (30 µM), we observed negligible ICD signal as shown in Inset of Figure 3.9. In contrast, the addition of lysozyme (30 µM) to the solutions of squaraine dyes **2** (Figure 3.9) and **3**, resulted in strong ICD signals in the absorption region of the squaraines. The ICD had one positive and one
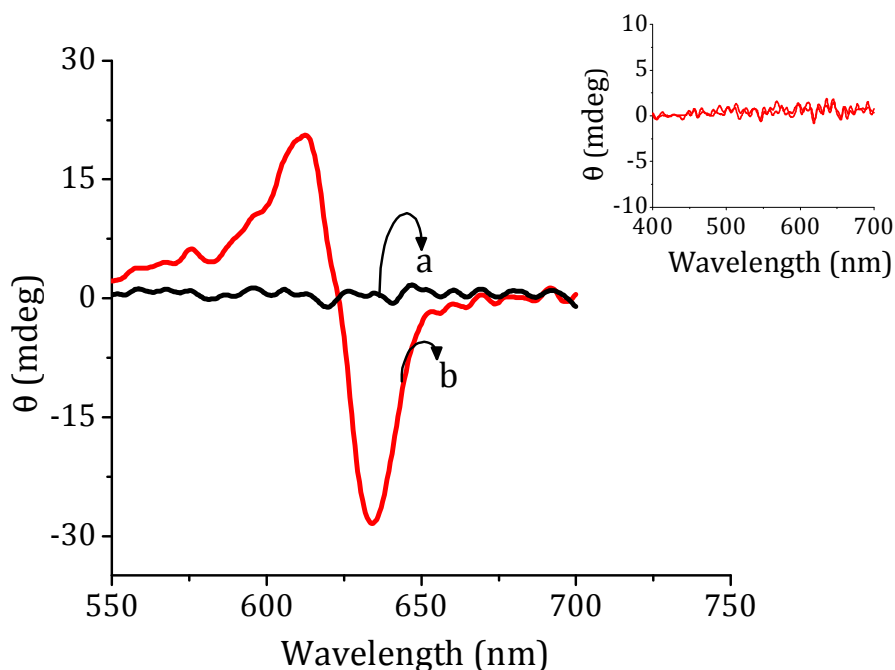
Figure 3.9. Circular dichroism (CD) spectra of the dye **2** (15 µM) in the presence of lysozyme in 2% ethanol-phosphate buffer (pH=6.4), [lysozyme]. a) 0 and b) 30 µM. The inset shows the CD spectra of the dye **1** (15 µM) in the presence of lysozyme (30 µM) in 2% ethanol-phosphate buffer (pH=8.4).

negative bands in the case of **2** at 612 nm and 636 nm, respectively. Meanwhile, the positive and negative bands in the case of **3** appeared at 612 nm and 637 nm. The two ICD peak positions approximately match with the absorption band positions of the bound [squaraines.lysozyme] complexes. The squaraine dyes **2** and **3**, when bound to lysozyme results in ICD signal due to the local asymmetric environment provided by the amino acid residues at the dye binding. The left-handedness in the CD spectra was found to be the nature of the complexes [**2/3**.lysozyme] and that provides the basis for the assumption that the sites of the binding of both dyes with lysozyme was with the β-sheets. These results gave a direct evidence for the complexation between the protein and the dyes **2** and **3**.

To get more insights into the nature of interaction of the squaraine **1**-**3** with lysozyme, we have carried out the studies with representative amino acid constituents of lysozyme such as cystein, L-lysine and glutamic acid. For example, Figure 3.10, shows the interaction of the dye **1** (1.7 μM) with the addition of increasing concentrations of cystein. We observed *ca.* 57% hypochromicity at ~584 nm in the absorption spectrum, when the concentration of cystein was 8.5 μM. On the other hand, the emission profile (inset of Figure 3.10) showed *ca.* 52% quenching in the fluorescence intensity at 600 nm. A similar trend of hypochromicity in absorption and quenching in the fluorescence intensity was observed when cystein was titrated with the dyes **2** and **3**. In addition, with glutamic acid , we observed *ca.* 52%, 69% and 42%, hypochromicity, respectively, in the absorption spectra of the squaraine dyes **1**-**3**, along with a significant quenching in
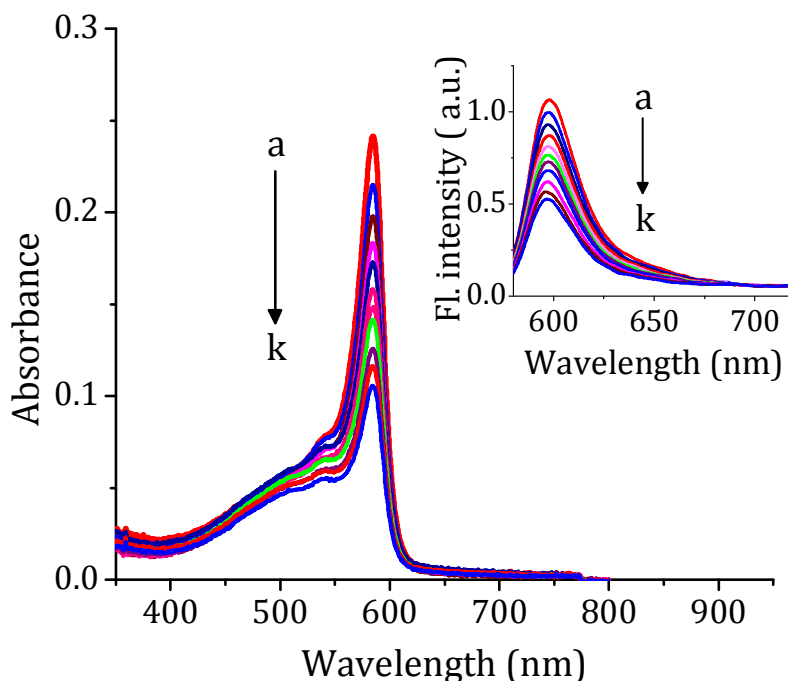
Figure 3.10. Changes in the absorption spectra of the dye **1** (1.7 µM) in 2% ethanol-phosphate buffer mixture at 8.4 pH with increase in concentration of cystein and inset shows the corresponding emission changes. [cystein] a) 0 and k) 8.5 µM.

the emission profile. When L-lysine was titrated with the dyes **1-3**, we observed negligible changes in the absorbance as well as emission intensity (Figure 3.11). These results indicate that cysteine and glutamic acid side chains of lysozyme found to interact strongly with the squaraine dyes while L-lysine showed negligible interactions. Moreover, in support of the hypothesis of a chemical reaction between the protein and the squaraine dyes under investigation, there have been few reports in the literature that cysteine and glutamic acid, which found to react with squaraine dyes to yield products, derived from them.[31]
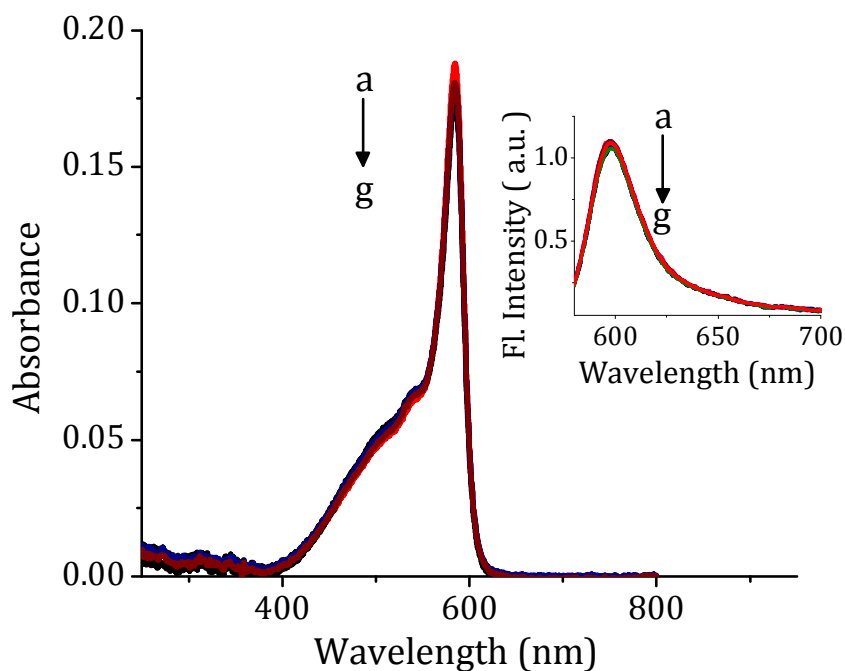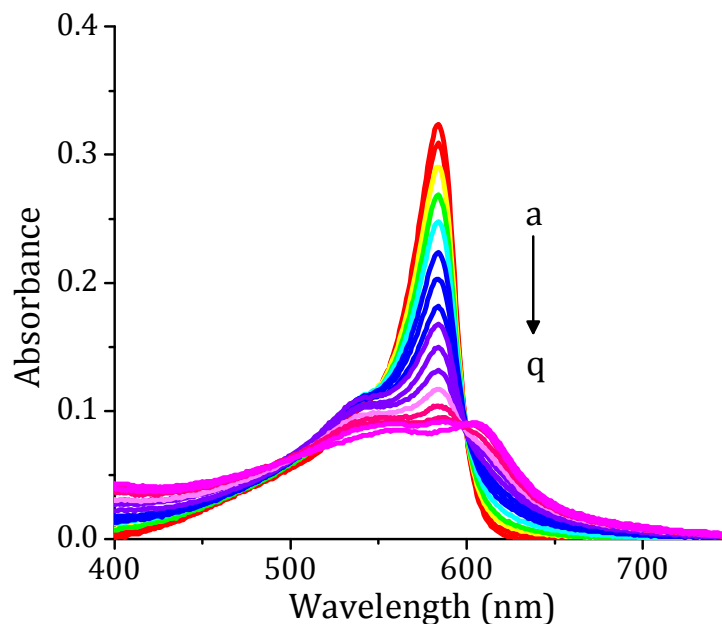
Figure 3.11. Changes in the absorption spectra of **1** (1.3 μM) in 2% ethanol-phosphate buffer at 8.4 pH with increase in concentration of L-lysine and the inset shows the corresponding emission spectral changes. [lysine] a) 0, and g) 20 μM.

### 3.3.4. Interaction of Squaraine Dyes with β-Amyloids

The amyloid fibrils are insoluble protein aggregates that have been associated with a range of neurodegenerative diseases, including Alzheimer's, Parkinson's, and Creutzfeldt-Jakob disease.[15] Inhibition of the amyloid fibril assembly is one of the strategies for therapeutic intervention to prevent proteins from aggregating. It was our interest to study the utility of the squaraines under investigation for the inhibition of the β-amyloid fibres. In this study, we have investigated the interaction of squaraines, **1**-**3** with the amyloid fibrils derived from

97

lysozyme. Lysozyme is often used as a model system, which upon incubation in acid solutions and at elevated temperatures found to form the amyloid fibrils.[14]

To understand the potential of the squaraine dyes **1-3**, under investigation for the inhibition of the amyloid fibrillation, we have monitored the changes in the absorption and emission spectra of these derivatives with the addition of increasing concentration of the amyloids. For example, with the addition of the amyloids to a solution of the dye **1** (2.3 μM), we observed a gradual decrease in the absorbance (*ca.* 74% hypochromicity) at 584 nm in 2% ethanol-phosphate buffer along with a ~23 nm bathochromic shift of the absorption maximum (Figure 3.12). A similar trend was observed with the dyes **2** (Figure 3.13) and **3** on titration with the amyloid fibers under similar experimental conditions. As the amyloid concentration

Figure 3.12. Changes in the absorption spectra of the dye **1** (2.3 μM) in 2% ethanol-phosphate buffer at 8.4 pH in the presence of the amyloids. a) 0 and q) 10 μM.
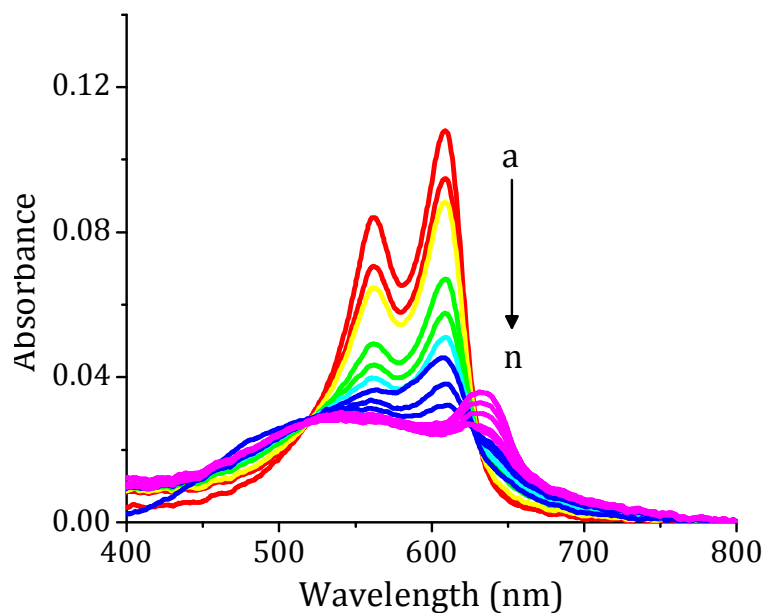
Figure 3.13. Changes in the absorption spectra of the dye **2** (2.3 µM) in 2% ethanol-phosphate buffer at 6.4 pH with the addition of the amyloids. a) 0, and n) 10 µM.
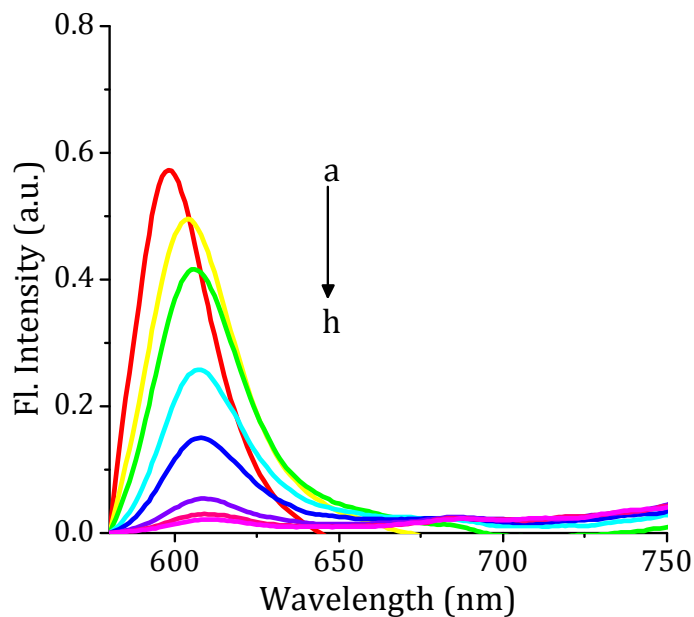

Figure 3.14. Changes in the emission spectra of the dye **1** (2.3 µM) with increasing concentrations of the amyloids in 2% ethanol-phosphate buffer at pH 8.4, a) 0 and h) 10 µM. Excitation wavelength, 560 nm.

was increased to *ca.* 10 μM, the absorbance of **2** and **3** at 611 nm and 613 nm, respectively, showed *ca.* 76% and *ca.* 68%, hypochromism along with a bathochromic shift of *ca.* 26 nm and 28 nm, respectively. Furthermore, the fluorescence spectral changes were monitored with the increasing concentrations of the amyloids. For example, by increasing the concentration of the amyloid (0-10 μM), the dye **1** (2.3 μM) exhibited complete quenching in the fluorescence intensity at 600 nm (Figure 3.14). We observed similar fluorescence quenching behavior in the case of the emission profiles of **2** and **3,** on interaction with the amyloids.

3.3.5. Nature of Interaction of squaraine Dyes with β-Amyloid Fibers

To understand the nature of interaction of the squaraine dyes **1-3** with β-amyloids, we have carried out isothermal titration calorimetry (ITC), thioflavin assay, and circular dichroism studies. Isothermal titration calorimetry (ITC) is capable of measuring the magnitude of the thermodynamic parameters that can define the binding affinity of the squaraine dyes with the amyloids. To quantify the binding affinities of the squaraine dyes with the amyloids, the interaction of **1-3** with amyloid was studied with ITC (Figure 3.15). With the increasing in addition of the amyloids to the solutions of the dyes **1-3** at 25 °C, the enthalpy change associated with each injection of the amyloid was found to be exothermic. The association constant for the squaraine **1** with the amyloids was found to be *ca.* 1.2×10^5 M^{-1}. Similarly, the association constants for the squaraines **2** and **3** with the amyloids
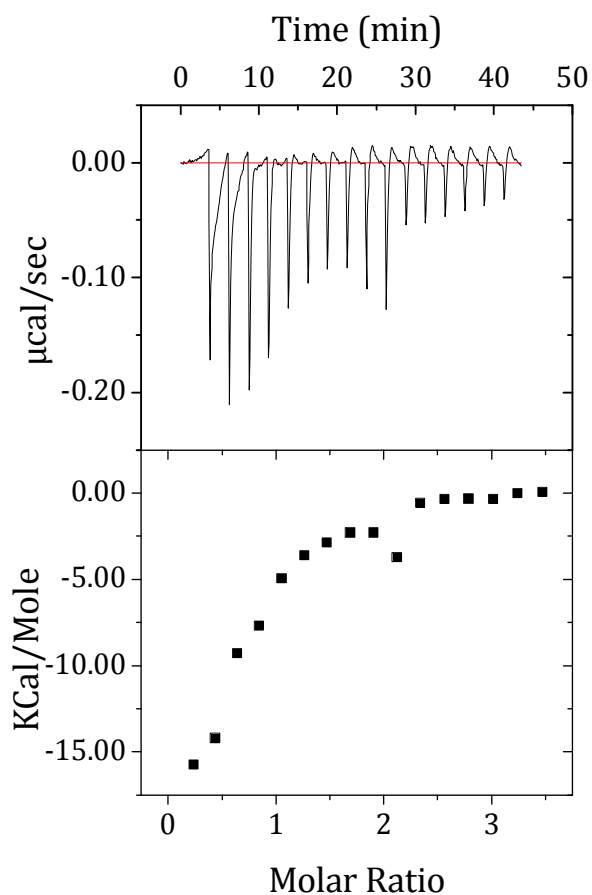
Figure 3.15. ITC titration of **2** (0.01 mM) with amyloids (0.1 mM) in 0.1% ethanol-phosphate buffer, pH 6.4. Differential power recorded in the experiment (top) and (bottom) shows the integration of areas corresponding to the amount of heat released upon addition of the amyloids as a function of the molar ratio.

were determined using the titration data and the values are found to be *ca.* 3.6×10^5 and 3.2×10^5 M^{-1}, respectively. The squaraine dyes **1**-**3**, on titration with the amyloids exihited almost similar values of binding parameters, like changes in enthalpy and entropy values. For example, the enthalpy change accompanying the interaction of the dye **1** with the amyloids was *ca.* -15.2 x 10^4 calMol^{-1}, while

the dyes **2** and **3** showed *ca.* -25.7 x 10^4, -12.6 x 10^4 calMol^{-1}, respectively. Similarly, the ΔS values were found to be negative (ranging from -11.93 to -59.1 calmol^{-1}K^{-1}). These thermodynamic parameters indicated that the non-covalent forces as well as hydrophobic interactions play a major role in the binding process between the squaraine dyes and the amyloid fibers.

To gain more insights on the nature of binding of the squaraine dyes **1-3**, with the amyloid fibers, we have employed literature reported thioflavin analysis. The small molecule, thioflavin T (ThT) is a standard probe for the identification and mechanistic study of the amyloid fibers formation.[33] Thioflavin T (ThT) is a benzothiazole salt which was known intercalate between hydrophobic amino acid residues which are parallel to the fibers axis of the amyloids and exhibits fluorescence at 485 nm. The ThT assay for understanding the binding interactions of the squaraine with the amyloids was carried out at pH 7.4 using phosphate buffer. A solution of the amyloid (8 µM) containing ThT (10 µM) was incubated at 37 °C in the absence (control) and presence of the dyes **1-3** (5 µM) for 30 min. The fluorescence of thioflavin of the control experiment was found to be at 485 nm, which was a characteristic observation of the presence of the amyloid fibers in the solution.[14] The addition of the dyes **1-3** (5µM) led to the complete quenching in the apparent fluorescence intensity of ThT at 485 nm (Figure 3.16). This observation, suggests the efficient inhibition of fibril formation in the presence of the squaraine dyes as noted for the literature known anti-amyloids (or anti-aggregates) agents.[17]
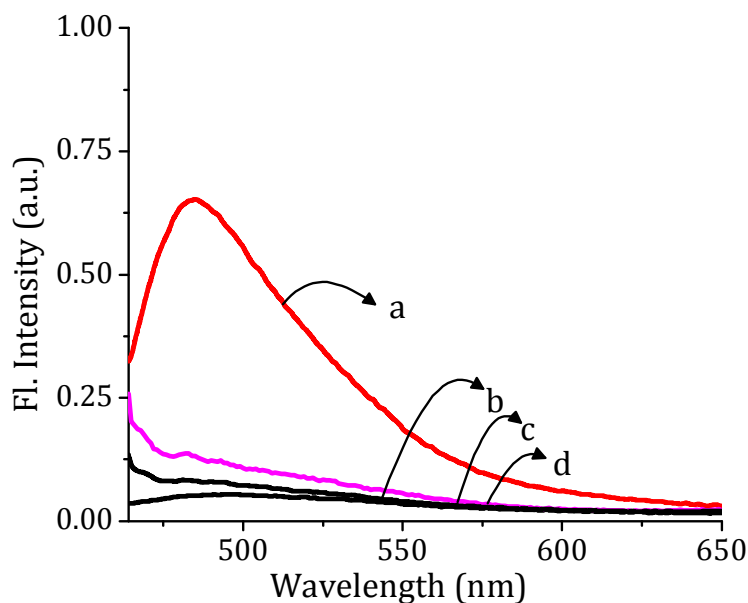
Figure 3.16. Changes in Thioflavin (10 µM) fluorescence intensity in the presence of a) amyloids alone (8 µM) and amyloids incubated with the dyes b) **3** c) **2** d) **1** (5 µM each) at pH 7.4. Excitation wavelength, 440 nm.

To understand the conformational changes of the amyloid fibers in the presence of squaraine dyes **1-3**, we have used far-UV CD spectroscopy. The CD spectra of the native protein exhibited two minima in the ultraviolet region at 208 and 222 nm, which are characteristic of an α-helical structure of the protein.[14,17] During the amyloid fibers formation, we observed the CD changes from an α-helical rich to a β-sheet rich profiles, as noted by the emergence of a new CD band at 230 nm (Figure 3.17). When this amyloid solution (8 µM) was incubated with the dye **1**, we observed a blue shift in the CD signal at 230 nm to 220 nm with a *ca.* 76% decrease in the negative ellipticity (Figure 3.18). Similar observation of blue shift was made in the presence of the halogenated dyes **2** and **3**. These results confirm the
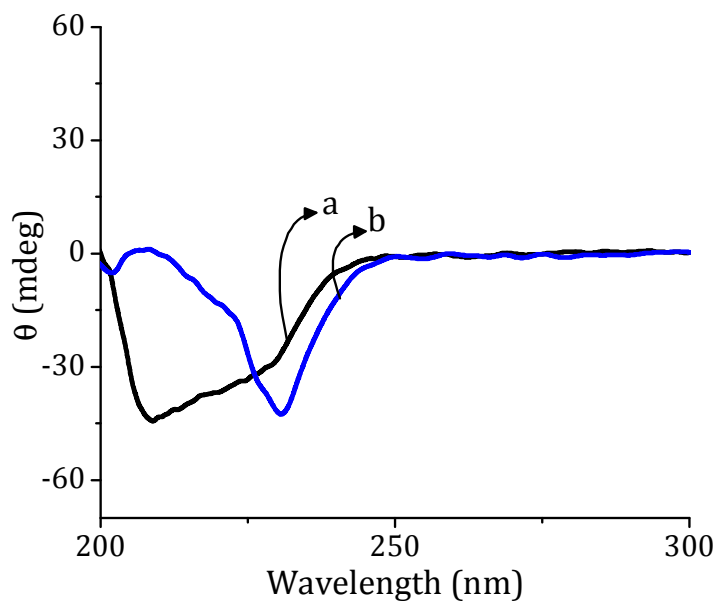
Figure 3.17. CD spectra of a) lysozyme (6 µM) and b) amyloid fibers (8 µM) synthesized from lysozyme following the literature protocol.
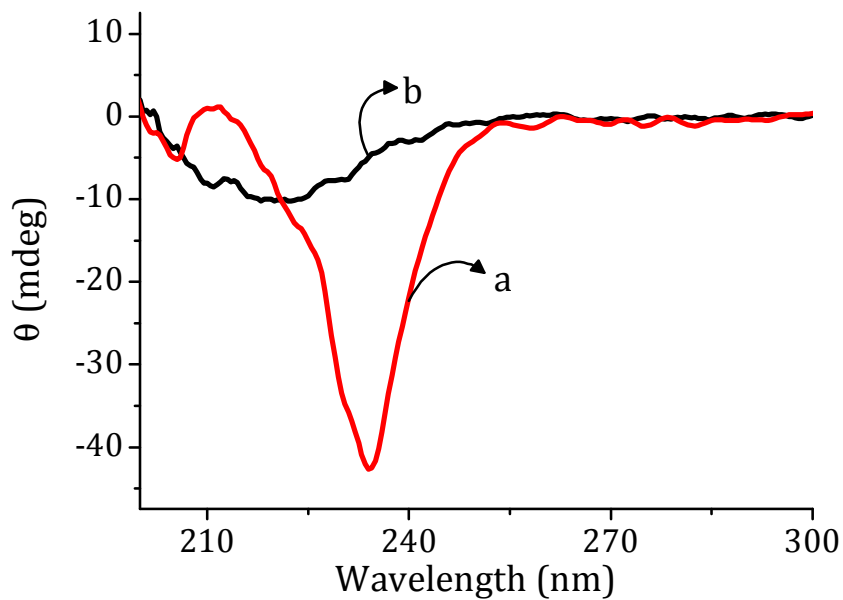

Figure 3.18. CD spectral changes of the amyloid fibers in the presence and absence of the squaraine dye **2**. a) Amyloid fibers alone (8 µM) and b) amyloid fibers (8 µM) in the presence of **2** (5 µM).

transformation of the secondary β-sheet structure to the α-helical rich in the presence of **1**-**3**, thereby demonstrating their potential as inhibitors of the amyloids.
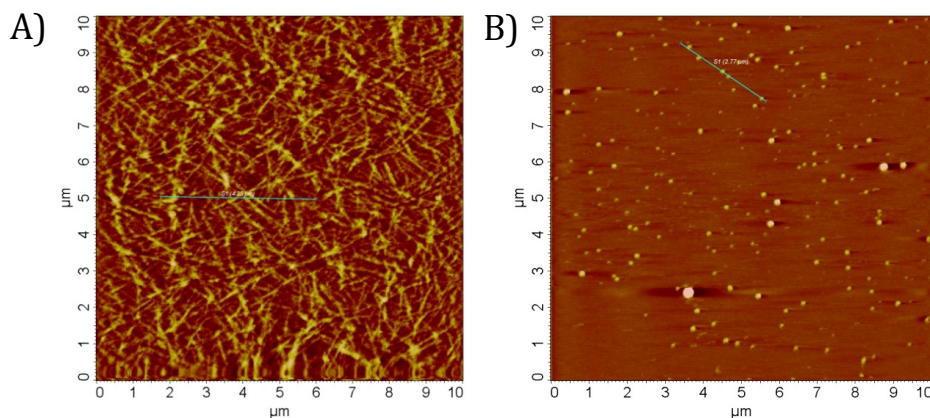
3.3.6. Morphological Analysis

To have more insights on the photophysical as well as chiroptic changes on interaction of the squaraine with the amyloids, we have carried out the morphological analysis through dynamic light scattering studies (DLS), AFM and TEM. DLS is a technique used for detecting and characterizing submicron aggregates *in situ*, with high temporal resolution. Figure 3.19, represents the correlograms of the DLS experiments of the amyloids in the presence of the dyes. In the presence of amyloids alone there was increased amplitude of the shoulder representing larger
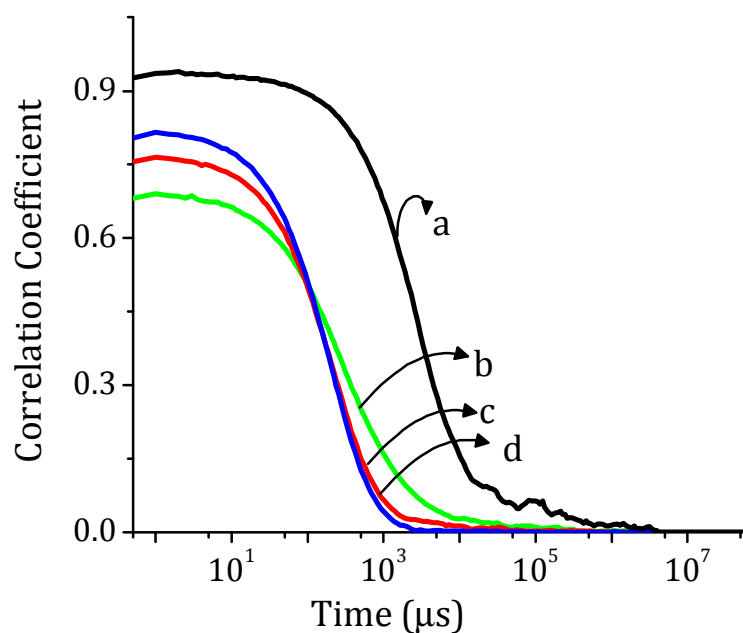

Figure 3.19. Correlogram of the dynamic light scattering experiments, a) amyloids alone (8 μM) and in the presence of the dyes, b) **1** c) **2** and d) **3** (5 μM).

aggregated species. The amplitude of the correlogram exhibited a steady decrease after the incubation with the squaraine dyes **1**-**3** (Figure 3.19). Furthermore, the extent of decrease was found to be similar for all the squaraine dyes **1**-**3** under investigation.

We have further carried out the morphological analysis through AFM as well as TEM. In the AFM studies, as could be evidenced from the Figure 3.20A, the amyloid fiber (8 µM) alone showed characteristic of the nano-fiber with diameters of *ca.* 20 nm. When we have incubated the amyloid fiber solution (8 µM) with the squaraine dye **2** (5 µM) for 30 min and drop casted the solution and imaged through AFM, we observed only spherical particles of average size of ~ 350 nm. These observations evidenced the disassembly of the amyloid fibers in the presence of the squaraine dye **2**. The further evidence for such a process was obtained through the
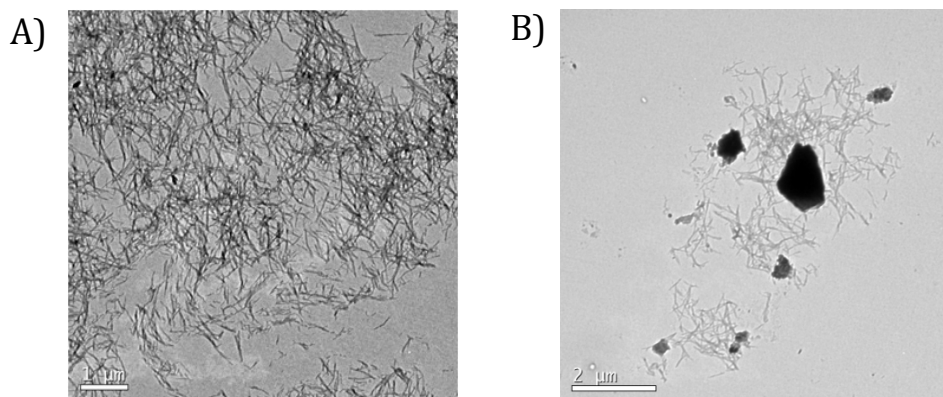

Figure 3.20. Morphological analysis of the amyloid fibers through AFM images in the absence and presence of the dye **2**. A) Amyloid fibers alone (8 µM) and B) amyloid fibers (8 µM) incubated with the dye **2** (5 µM).
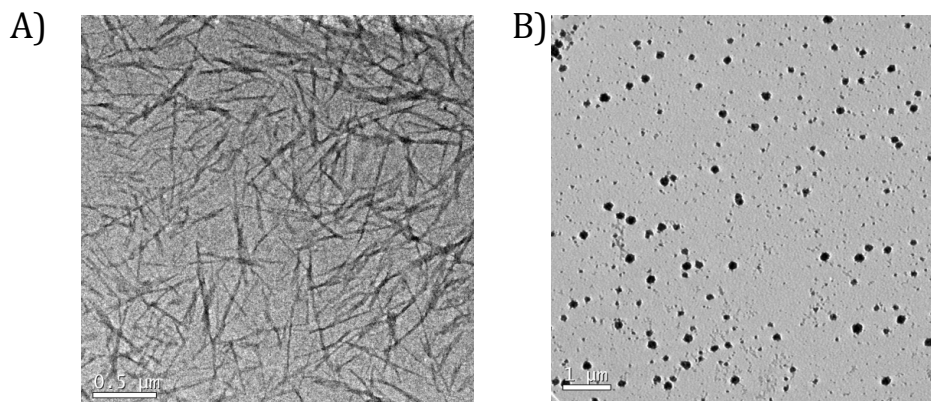
Figure 3.21. Morphological analysis of the amyloid fibers through TEM images in the absence and presence of the dye **2**. A) Amyloid fibers alone (8 µM) and B) amyloid fibres (8 µM) incubated with the dye **2** (5 µM).

transmission electron microscopic (TEM) analysis, wherein, we observed the complete destruction of the amyloid fibers (Figure 3.21) and transformation of fibers into spherical particles of average diameter, *ca*. 350 nm. Similar observations were made with the dye **3**. In contrast, the incubation of the amyloid fibers with the dye **1** (5 µM) under similar conditions, we observed negligible destruction of the amyloid fibers as shown in Figure 3.22. The amyloid structures in the absence and presence of **1-3** was further studied by X-ray diffraction measurements. The principal features of the X-ray pattern from the amyloids consist of a sharp and intense ring at 4.75 Å along with a broad and less intense ring at 9.8 Å. Figure 3.23A shows the X-ray fiber diffraction pattern showing the 4.7-4.8 Å meridional reflections that define the basic β-structure of the amyloids. In the presence of the squaraine dye **2** (5 µM), we observed disappearance of the diffraction pattern at

Figure 3.22. Morphological analysis of the amyloid fibers through TEM images in the absence and presence of the dye **1**. TEM images of A) amyloids alone (8 µM), B) amyloids incubated with the dye **1** (5 µM).
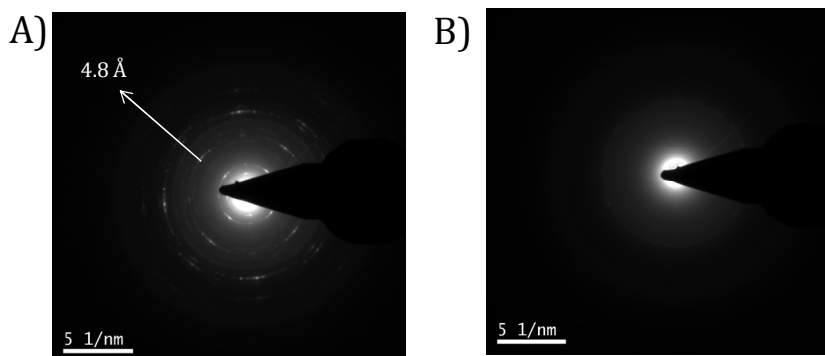
Figure 3.23. A) X-ray fibre diffraction pattern showing basic β-structure of the amyloids alone. B) X-ray fibre diffraction pattern in the presence of **2** (5 µM).

4.8 Å confirming thereby the destruction of amyloid fibers in the presence of the dye

2 (Figure3.23B). Similar results confirming the inhibition of the amyloid fibers was observed with the dye **1** as well as **3**. The morphological studies and the CD data

discussed earlier corroborate that the dyes **1**-**3** are an excellent inhibitors of the amyloid fibrillogenesis and can be efficiently utilized as anti-amyloidogenic agents.

3.4. CONCLUSION

In summary, we have studied the interactions of the polyhydroxyl substituted squaraine dyes **1**-**3** with lysozyme and the amyloids derived from lysozyme. These dyes showed good solubility in the aqueous medium and exhibited favorable photophysical properties. The study of their interactions with various proteins revealed that **1**-**3** showed strong interactions with serum albumins as well as lysozyme. The strong binding with lysozyme was further confirmed through various photophysical and biophysical techniques like circular dichroism and isothermal titration calorimetry. The half-reciprocal analysis of the absorption data and isothermal titration calorimetric (ITC) analysis of the titration experiments gave a 1:1 stoichiometry for the complexes with the association constants (K_{ass}) in the range 10^4-10^5 M^{-1}. Furthermore, the study of the interactions of these NIR dyes **1**-**3** with the β-amyloid fibers derived from lysozyme indicated that these dyes interact effectively with this aggregated protein. Such an effective interaction resulted in the complete destabilization of the amyloid fibers and transformation of these fibers into spherical particles of *ca*. 350 nm in the presence of the dyes **1**-**3** as demonstrated through ITC, circular dichroism, thioflavin assay and microscopic analyses. These results demonstrate the dyes **1**-**3** under study can act as efficient protein labeling agents as well as the inhibitors of the protein amyloidogenesis.

3.5. EXPERIMENTAL SECTION

3.5.1. General Techniques

All melting points are uncorrected and were determined on a Mel-Temp II melting point apparatus. The electronic absorption spectra were recorded on a Shimadzu UV-3101PC UV-VIS-NIR scanning spectrophotometer. The fluorescence spectra were recorded on a SPEX-Fluorolog F112X spectro-fluorimeter. The ^{1}H and ^{13}C NMR spectra were obtained using a Bruker DPX-300 MHz spectrometer. The mass spectra were recorded on a JEOL AX503 mass spectrometer. The pH measurements were carried out using ELICO Model L1-120 digital pH meter, which was calibrated using standard buffer solutions of pH 4 and 9.2. The fluorescence quantum yields were determined by using cresyl violet ($\Phi_s = 0.52$) in methanol as the standard, wherein, A_s and A_u are the absorbance of standard and unknown, respectively. The quantum yields of fluorescence emission were calculated using the equation 3.1.

$$\Phi_u = \frac{A_s\,F_u\,n_u{}^2}{A_u\,F_s\,n_s{}^2}\,\Phi_s \qquad \text{(Eq. 3.1)}$$

F_s and F_u are the areas of fluorescence peaks of the standard and unknown and n_s and n_u are the refractive indices of the solvents used for the standard and unknown, respectively. Φ_s and Φ_u are the fluorescence quantum yields of the standard and unknown compounds. The Circular dichroism (CD) spectra were recorded on Jasco

Corporation, J-810 spectropolarimeter. All experiments were carried out at room temperature (25 ± 1°C), unless otherwise mentioned.

3.5.1.1. Transmission Electron Microscopy (TEM). TEM analysis was performed on JEOL 100 kV high resolution transmission electron microscope. A drop of amyloid solution or amyloid incubated with squaraine **1**-**3** solution was placed on the top of carbon-coated Cu grid. The grids were mounted on reverse tweezers and the samples were dried by a vacuum pump under reduced pressure for 1 h at room temperature. The accelerating voltage of the transmission electron microscope was 100 kV and the beam current was 65 A. Samples were imaged using a Hamamatsu ORCA CCD camera.

3.5.1.2. Atomic Force Microscopy (AFM). The AFM images were recorded under ambient conditions using a NTEGRA (NT-MDT) and operated with the use of tapping mode regime. Micro-fabricated TiN cantilever tips (NSG10) with a resonance frequency of 299 kHz and a spring constant of 20-80 Nm^{-1} were used. AFM section analysis was done offline. Samples for the imaging were prepared by drop casting the solution on freshly cleaved mica surfaces at the required concentrations and at ambient conditions.

3.5.1.3. Dynamic Light Scattering (DLS). The DLS studies were carried out on a Nano Zeta Sizer, Malvern instruments. The samples were prepared in water at required concentrations. The light scattering experiments were performed under low polydipersity index by using glass cuvettes. The hydrodynamic diameters and
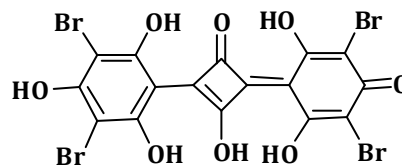
polydisperse indices of the samples were determined using a Malvern Zeta Nano-ZS system.

3.5.1.4. Isothermal Titration Calorimetry (ITC). Isothermal titration calorimetric titrations were carried out using a Microcal ITC200 microcalorimeter (Microcal, Northampton, MA). All the data were calculated with Origin ITC data-analysis software using one set of binding site model.

3.5.2. MATERIALS

Lysozyme, phloroglucinol, squaric acid, bromine, iodine monochloride and glacial acetic acid were purchased from Sigma Aldrich and S. D. Fine Chemicals, India and were used without further purification. The squaraine dye **1** was prepared by the reaction of phloroglucinol with squaric acid by adopting a reported procedure.[21]

3.5.2.1. Synthesis of bis (3,5-Dibromo-2,4,6-trihydroxyphenyl)-squaraine (2). The squaraine dye **1** (0.3 mmol) was dissolved in glacial acetic acid (85 mL) by stirring the solution at 50 °C for 90 min. After cooling the solution to room temperature, bromine (1.3 mmol) in glacial acetic acid (15 mL) was added dropwise, over a period of 1 h. The reaction mixture was kept in the refrigerator for 4 h to yield **2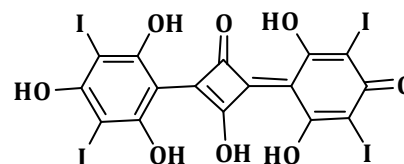** (80%), mp 315 °C, which was recrystallized from a mixture (4:1) of water and isopropanol. IR (KBr) ν_{max} 519, 726, 1622 and 3413 cm^{-1}; HRMS-ESI Calcd for $C_{16}H_6O_8Br_4$: 642.68, Found: 642.68 (M$^+$).

3.5.2.2. Synthesis of bis (3,5-Diiodo-2,4,6-trihydroxyphenyl)squaraine

(3). The squaraine dye **1** (0.3 mmol) was dissolved in glacial acetic acid (85 mL) by stirring the solution at 50 °C for 90 min. After cooling the solution, iodine monochloride (1.3 mmol) in glacial acetic acid (15 mL) was added dropwise, over a period of 1 h. The reaction mixture was further stirred for 1 h. Water (15 mL) was added to the reaction mixture and kept in the refrigerator for 5 h.

The solid precipitate was filtered to give 180 mg (71%) of **3**, mp 270 °C, which was recrystallized from a mixture (4:1) of methanol and isopropanol. IR (KBr) ν_{max} 508, 726, 1603, and 3383 cm^{-1}; HRMS-ESI Calcd for $C_{16}H_6O_8I_4$: 834.6320. Found: 834.8360 (M$^+$).

3.5.2.3. Preparation of Lysozyme Amyloid Fibers.

Lysozyme fibrils were prepared according to previous report with minor modification.[14] Briefly, 100 mg hen egg white lysozyme was dissolved in 10 ml HCl solution (10 mM, pH 4.0) in 10 mM HCl containing 0.02% NaN$_3$ at pH 4.0. The final concentration was 10 mg/ml. The mixture was incubated for 10 days at 65 °C in a water-bath without agitation. The growth of lysozyme fibril was monitored by thioflavin fluorescence and transmission electron microscopy (TEM) measurements.

3.5.3. METHODS

3.5.3.1. Calculation of association constant (K_{ass}).

The binding constant K_{ass} was determined from the half reciprocal plot of $D/\Delta\varepsilon_{ap}$ vs D, where D is the

concentration of lysozyme, $\Delta\varepsilon_{ap} = [\varepsilon_a - \varepsilon_F]$ and $\Delta\varepsilon = [\varepsilon_b - \varepsilon_F]$.[32] The apparent extinction coefficient, ε_a, is obtained by calculating $A_{[obsd]}/$ [squaraine]. ε_b and ε_F correspond to the extinction coefficient of the bound form of the squaraine derivatives and the extinction coefficient of the free squaraine, respectively. The data were fitted to Equation 3.2, with a slope equal to $1/\Delta\varepsilon$ and a y-intercept equal to $1/(\Delta\varepsilon K_{ass})$. ε_b was determined from $\Delta\varepsilon$ and $K_{Lysozyme}$ was obtained from the ratio of the slope to the y-intercept.

$$D/\Delta\varepsilon_{ap} = D/\Delta\varepsilon + 1/(\Delta\varepsilon\, K_{DNA}) \qquad \text{(Eq. 3.2)}$$

3.5.3.2. Calculation of change in free energy (ΔG). Change in free energy (ΔG) associated with the complexation between SQ and lysozyme, was determined using the equation 3.3, where K_{ass} is the association constant.

$$\Delta G = -2.303\text{RT}\log K_{ass} \qquad \text{(Eq. 3.3)}$$

3.6. REFERENCES

1.   a) C. Branden and J. Tooze, *Introduction to protein structure*, Garland Publishing, New York, **1991**.

2.   a) S. K. Pal and A. H. Zewail, *Chem. Rev.*, **2004,** *104,* 2099; b) C. E. Lyon, E. S. Suh, C. M. Dobson and P. J. Hore, *J. Am. Chem. Soc.*, **2002,** *124,* 13018.

3.   a) H. M. Berman, *Curr. Opin. Biotechnol.*, **1999**, *10*, 76. b) D. J. Prockop and K. I. Kivirikko, *Annu. Rev. Biochem.*, **1995**, *64*, 403.

4.   D. Voet and J. G. Voet, *Biochemistry*, John Wiley and Sons, New York, **1995**.

5.   A. Banerjee, W. Yang, M. Karplus and G. L. Verdine, *Nature*, **2005**, *434*, 612.

6.   a) S. L. Cohen, D. G. Cramp, A. D. Lewis and T. R. Tickner, *Clin. Chim. Acta*, **1980**, *104*, 393; b) G. Baldo-Enzi, M. R. Baiocchi, G. C. VignaMosconi and R. Fellin, *J. Inher. Metab. Dis.,* **1987**, *10*, 317.

7.   a) J. P. Collman, R. Boulatov, C. J. Sunderland and L. Fu, *Chem. Rev.,* **2004**, *104*, 561; b) M. Momenteau and C. A. Reed, *Chem. Rev.*, **1994**, 94, 659.

8.   a) S. H. Gellman, *Chem. Rev.*, **1997**, *97*, 1231; b) H.-J. Schneider and A. K. Yatsimirsky, *Chem. Soc. Rev. 37*, **2008**, 263.

9.   a) J. Davila and A. Harriman, *Photochem. Photobiol.*, **1989**, 51, 9; b) R. Langlots, H. Ali, N. Brasseur, J. R. Wagner and I. R. van Lier, *Photochem. Photobiol.*, **1986**, 44, 117.

10.   a) L. Beljaars, G. Molema, D. Schuppan, A. Geerts, P. J. De Bleser, B. Weert, D. K. F. Meijer and K. J. Poelstra, *J. Biol. Chem.*, **2000**, *275*, 12743.

11.   P. Kurtzhals, S. Havelund, I. Jonassen, B. Kiehr, U. D. Larsen, U. Ribel and J. Markussen, *Biochem. J.*, **1995**, *312*, 725.

12.   a) J. W. Kelly, *Curr. Opin. Struct. Biol.,* **1998**, *8*, 101; b) M. Stefani and C. J. Dobson*, Mol. Med.*, **2003**, *81*, 678.

13.   a) C. M. Dobson, *Nature,* **2003**, *426*, 884; b) J. Hardy and D. J. Selkoe, *Science*, **2002**, *297*, 353.

14.   A. L. Gharibyan, V. Zamotin, K. Yanamandra, O. S. Moskaleva, B. A. Margulis, I. A. Kostanyan and L. A. M. Roche*, J. Mol. Biol.*, **2007**, *365*, 1337.

15.   a) N. Rubin, E. Perugia, M. Goldschmidt, M. Fridkin and L. Addadi, *J. Am. Chem. Soc.,* **2008**, *130*, 4602; b) D. Ozawa, H. Yagi, T.Ban, A. Kameda, T. Kawakami, H. Naiki and Y. Goto, *J. Biol. Chem.*, **2009**, 284, 1009.

16.   a) C. V. Kumar and A. Buranaprapuk, *Angew. Chem., Int. Ed. Eng.*, **1997**, *36*, 2085; b) C. V. Kumar, L. Qin and P. K. Das, *J. Chem. Soc. Faraday Trans.*, **1984**, *80*, 783; c) C. V. Kumar, A. Buranaprapuk, H. C. Sze, S. Jockusch and N. J. Turro, *Proc. Natl. Acad. Sci. U. S. A.*, **2002**, *99*, 5810.

17.   a) J. B. Ghaim , D. P. Greiner, C. F. Meares and R. B. Gennis, *Biochemistry*, **1995**, *34*, 11311; b) M. R. Ermacora, J. M. Delfino, B. Cuenoud, A. Schepartz and R. O. Fox, *Proc. Natl. Acad. Sci. U. S. A.*, **1992**, *89*, 6383.

18.   a) R. Schmidt, *Photochem. Photobiol.*, **2006**, *82*, 1161; b) R. W. Bigelow and H. J. Freund, *Chem. Phys.*, **1986**, *107*, 159.

19.   a) J. Fabian, H. Nakazumi and M. Matsuoka, *Chem. Rev.*, **1992**, *92*,1197; b) S. Sreejith, K. P. Divya, and A. Ajayaghosh, *Angew. Chem., Int. Ed.,* **2008**, *120*, 8001.

20.   a) R. R. Avirah, K. Jyothish and D.Ramaiah, *Org. Lett.*, **2007**, *9*, 121; b) K. T. Arun and D. Ramaiah, *J. Phys. Chem. A*, **2005**, *109*, 5571; c) K. Jyothish, M. Hariharan and D. Ramaiah, *Chem. Eur. J.*, **2007**, *13*, 5944.

21.   a) A. Triebs, and K. Jacob, *Angew. Chem., Int. Ed.,* **1965**, *4,* 694; b) D. Ramaiah, A. Joy, N. Chandrasekhar, N. V. Eldho, S. Das and M. V. George, *Photochem. Photobiol.*, **1997**, *65*, 783; c) S. Das, P. V. Kamat, B. D. Barre, K. G. Thomas, A. Ajayaghosh and M. V. George, *J. Phys. Chem.*, **1992,** *96*, 10327.

22.   a) N. J. Turro, *Modern Molecular Photochemistry*; Benjamin/Cumings: Menlo Park, CA, **1978**; b) M. R. Detty, and P. B. Merkel, *J. Am. Chem. Soc.,* **1990**, *112*, 3845.

23.   a) V. S. Jisha, K. T. Arun, M. Hariharan and D. Ramaiah, *J. Am. Chem. Soc.,* ***2006,*** *128, 6*024; b) V. S. Jisha, K. T. Arun, M. Hariharan and D. Ramaiah, *J. Phys. Chem. B,* **2010,***114,* 5912; c) P.D. Ross and S. Subramanian, *Biochemistry*, **1981**, *20,* 3096.

24.   a) J. V. Ros-Lis, B. Garcia, D. Jime nez, R. Martι´nez-Manez, F. Sancenon, J. Soto, F. Gonzalvo and M. C. Valldecabres, *J. Am. Chem. Soc.*, **2004**, *126*, 4064; b) J. V. Ros-Lis, R. M. Manez and J. Soto, *Chem. Commun.*, **2002**, 2248.

25.   a) E. Kuruvilla and D. Ramaiah, *J. Phys. Chem. B,* **2007**, *111*, 6549; b) J. Joseph, E. Kuruvilla, A. T. Achuthan, D. Ramaiah and G. B. Schuster, *Bioconjugate Chem.*, **2004**, *15*, 1230.

26.   a) H. Levine, *Protein Sci.*, **1993**, *2*, 404; b) M. Groenning, M. Norrman, J. M. Flink, M. van de Weert, J. T. Bukrinsky, G. Schluckebier and S. Frokjaer, *J. Struct. Biol.*, **2007**, *159*, 483.

27.   C. Rodriguez-Rodriguez, A. Rimola, L. Rodriguez-Santiago, P. Ugliengo, A. Alvarez-Larena, H. Gutierrez-de-Teran, M. Sodupe and P. Gonzalez-Duarte, *Chem. Commun.*, **2010**, 1156.

28.   a) K. Harata and H. Uedaira, *Bull. Chem. Soc. Jpn.*, **1975**, *48*, 375.

29.   T. D. Slavnova, H. Golrner and A. K. Chibisov, *J. Phys. Chem. B*, **2007**, 111, 33.

30.   a) D. R. Booth, M. Sunde, V. Bellotti, C. V. Robinson and W. L. Hutchinson, *Nature*, **1997**, *385*, 787; b) E. Frare, M. F. Mossuto, P. P. Laureto, M. Dumoulin and C. M. Dobson *J. Mol. Biol.*, **2006**, *361*,551.

31.   L. N. Arnaudov, and R. D. Vries, *Biophys. J.*, **2005**, *88*, 515.

32.   a) Wallevik, K. *J. Biol. Chem.*, **1973**, *248*, 2650; b) J. Chmelik, P. Anzenbacher and J. Chmelikova, C*hem. Commun.,* **1988**, *53*, 411.

33.   Y. Porat, A. Abramowits and E. Gazit, *Chem. Biol. Drug. Des.,* **2006**, *67*, 27.

SYNTHESIS, PHOTOPHYSICAL, SELF-ASSEMBLY AND BIO-IMAGING PROPERTIES OF NOVEL TPE CONJUGATES
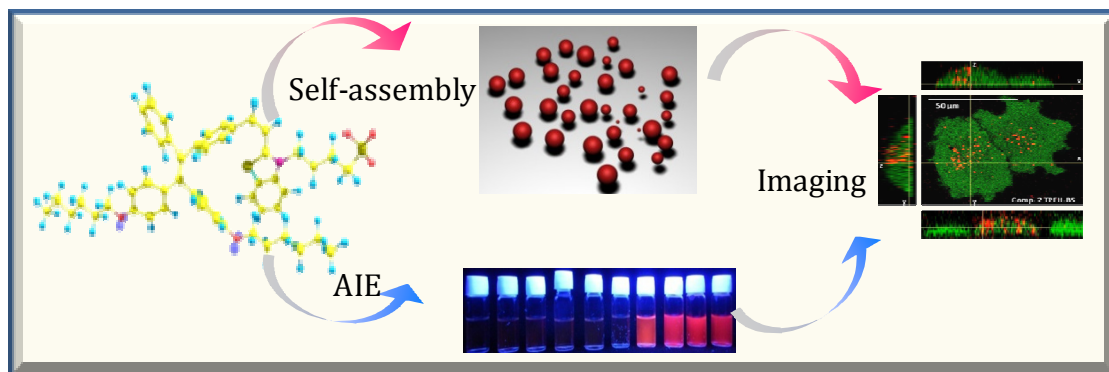
4.1. ABSTRACT

We designed few novel tetraphenylethene-benzothiazole conjugates **4-6** and have investigated their photophysical, self-assembly and bio-imaging properties under different conditions. These conjugates consist of an iconic tetraphenylethene (TPE) moiety as the electron donor (D) and benzothiazole core as the electron acceptor (A) unit. These systems exhibited significantly reduced fluorescence due to the intramolecular charge transfer (ICT) mechanism and showed significant variation in the absorption and emission features with the increase in the percentage of water in acetonitrile. We have observed a "Turn-on" fluorescence intensity through aggregation induced enhanced emission (AIEE), when the water fraction (f_w) was increased to *ca*. 70%, 50% and 95% in acetonitrile for **4**, **5** and **6**,

respectively. We have carried out morphological studies through various microscopic techniques like transmission electron microscope (TEM) and scanning electron microscope (SEM) and have observed self-assembled architectures like nanorods for the derivatives **4** and **5**, while nanoflowers were observed for the system **6**. On further increasing the water percentage to *ca.* 99%, we observed the disassembly of the self-assembled nanostructures resulting in the formation of nanoparticles (NPs) of ∼ 10 nm in all the three cases. The cellular toxicity, uptake and efficiency of intracellular imaging applications of the TPE conjugates **4-6** were explored through MTT assay, flow cytometry and confocal laser scanning microscopy (CLSM). The nanoparticles of these conjugates **4-6**, which were formed when the water percentage was increased to *ca.* 99%, have been found to have unique cellular uptake mechanism and were found to be localized within the cellular cytoplasm. These nanoparticles exhibited efficient fluorescence emission, large stokes shift, good stability, biocompatibility and excellent cellular imaging properties and hence can have potential applications for tracking and monitoring of cells for cancer research and in cell-based therapy.

4.2. INTRODUCTION

The development of efficient luminescent materials with aggregation induced enhanced emission (AIEE) is a topic of great current interest. This is because of the fact that the aggregation induced quenching (ACQ) effect has prohibited the technological applications of the conventional fluorophores in optoelectronics and

bioscience.[1] Therefore the potential applications of the conventional dye molecules have been limited due to the existence of intermolecular π-π interactions that favor the dye aggregation, which normally results in quenching of the fluorescence intensity.[2] To alleviate the ACQ problem, various physical, chemical and engineering methods have been developed but these strategies showed only a limited success.[1-2] For example, Tang *et al.*, have reported for the first time a phenomenon called aggregation-induced emission (AIE) or aggregation-induced enhanced emission (AIEE).[3a] The authors have employed propeller-shaped molecules such as silole[3] and tetraphenylethene in which the fluorescence emission was enhanced, rather than quenched upon aggregation.[4,5] This discovery of AIE fluorophores has attracted a lot of attention, which led to the development of newer AIE molecules for various technological applications.[6]

Among the various molecules, the tetraphenylethene (TPE) based systems have been explored intensively due to their facile synthesis and excellent AIE properties.[7] The TPE molecules are non-emissive in solution but exhibited high emission in the aggregated state.[1,4] The freedom of rotation of the phenyl rings and twisting of the C=C bond has been attributed to the quenched fluorescence of these systems in solutions.[8] The restriction of the intramolecular rotation (RIR) of phenyl substituent can suppress the non-radiative decay pathways thereby can cause the AIE effect.[9-12] In this context, the conjugated molecules with electron donor-acceptor (D-A) architectures have been investigated due to their unique photochemical and intramolecular charge transfer (ICT) properties.[13] Though such effective molecules

can have applications in biophotonics, long wavelength emitters, and as two photon absorption materials, the synthesis of the emissive D-A conjugates is still a challenge because of the ACQ effects.

The strategy for the conjugated molecules having electron donor-acceptor (D-A) architectures in which one of the constituents is an AIE active chromophore has attracted attention because of their unique photochemical properties along with the AIE effect.[14] On the other hand, the emergence of the fluorescence imaging probes based on organic dyes has proven to be a powerful tool due to their unrivalled ability to locate and monitor biological targets.[15] To minimize the optical interferences like light scattering and autofluorescence of the biological media, which limit the detection sensitivity of the fluorescence probe, it is desirable to have the probe with intense emission in the far-red/near-infrared (FR/NIR) region.[17] Such effective systems can have potential use in visualization of cancerous cells and thereby their application in ideal cancerous medical diagnostics and therapeutics.[16] To date, a large variety of materials, including organic dyes,[18] fluorescent proteins[19] and inorganic quantum dots (QDs),[20] have been studied as FR/NIR fluorescence imaging agents. The organic dyes and fluorescent proteins, however, suffer from limited molar absorptivity and low photobleaching thresholds,[21] while inorganic QDs were found to be highly cytotoxic in an oxidative environment[22] thereby limiting the scope of their *in vitro* and *in vivo* applications.

With a view to develop efficient emitting materials, we have designed and synthesized novel TPE-benzothiazole conjugates **4-6** (Chart 4.1) and have

investigated their photophysical and *in vitro* photobiological properties. These systems having electron donor-acceptor (D-A) moieties exhibited intramolecular charge transfer (ICT) interactions, efficient aggregation induced enhanced emission (AIEE) along with unique self-assembling properties in different solvent ratios. Detailed morphological studies through various microscopic techniques have revealed that the self-assembled architectures like nanorods were observed for the conjugates **4** and **5**, while nanoflowers for the system **6**. At water fraction of *ca*. 99%, the self-assembled nanostructures were disassembled to form nanoparticles (NPs) and which exhibited efficient cellular uptake and localization in cytoplasm demonstrating thereby there potential for cell imaging applications.
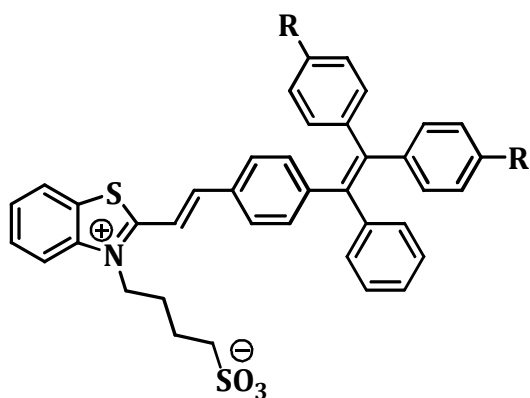

4) R= OC$_6$H$_{13}$
5) R= OC$_{12}$H$_{25}$
6) R= H

Chart 4.1

4.3. RESULTS AND DISCUSSION

4.3.1. Synthesis of the TPE-Benzothiazole Conjugates

The synthesis of the alkyl substituted TPE-benzothiazole conjugates **4** and **5** and the non-alkylated derivative **6**, was achieved in good yields as shown in Scheme 4.1. The hexyl and dodecyl derivatives **8a** and **8b**, respectively, were synthesized by the reaction of the corresponding 4,4'-dialkyloxybenzophenone with 4-bromo-benzophenone using a modified McMurry cross coupling reaction.[1] The crude product thus obtained was purified by column chromatography, which afforded **8a** and **8b** in *ca*. 10% and *ca*. 12% yields, respectively. The non-alkylated derivative **8c** (*ca*. 12%) was similarly prepared by using benzophenone and 4-bromo-benzophenone under similar conditions. The derivatives **8a-c** were converted to their corresponding aldehydes **9a-c** (*ca*. 38-42%) by the reaction with n-BuLi followed by formylation using DMF as the solvent. Subsequently, the synthesis of the TPE-benzothiazole conjugates, **4**, **5** and **6**, was achieved in good yields (*ca*. 89-92%) by the reaction of the corresponding TPE aldehyde with the quaternized salt of the benzothiazole derivative. All these products were purified and well characterized through various analytical and spectroscopic techniques. For example, ^{1}H NMR spectrum of the TPE linked benzothiazole conjugate **4** in CDCl$_3$, showed a peak corresponding to the vinylic proton at δ 8.53 as a doublet with a coupling constant of 15.5 Hz, while the aromatic protons corresponding to the TPE and benzothiazole moieties were appeared as multiplets in the region between δ 8.5 and δ 6.2. Similar observations were made with the derivative **5** and the model compound **6**.
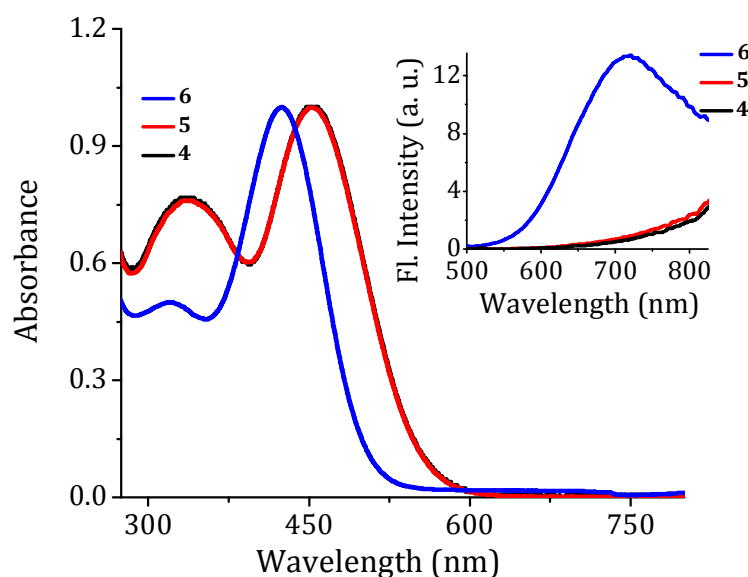
124
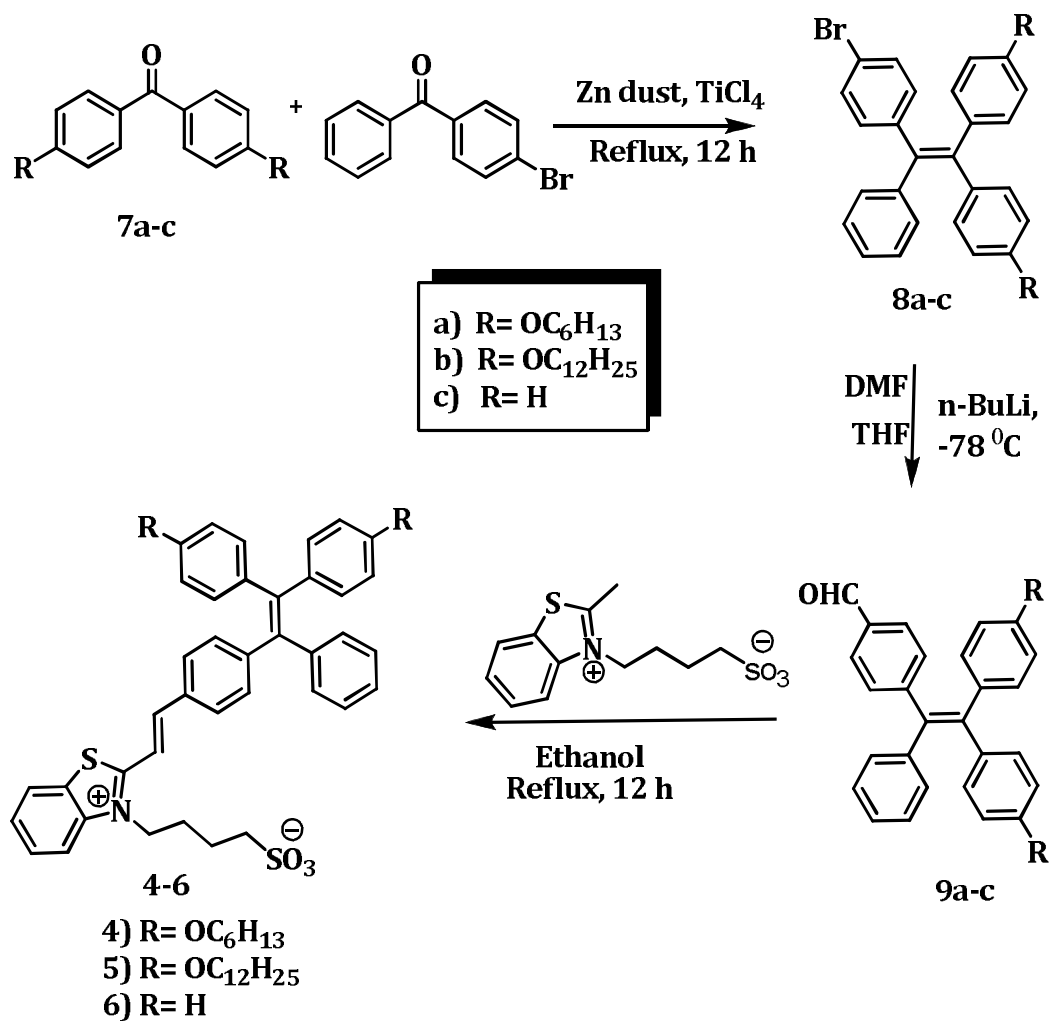
Scheme 4.1. Synthesis of the TPE-benzothiazole derivatives **4**, **5** and **6**.

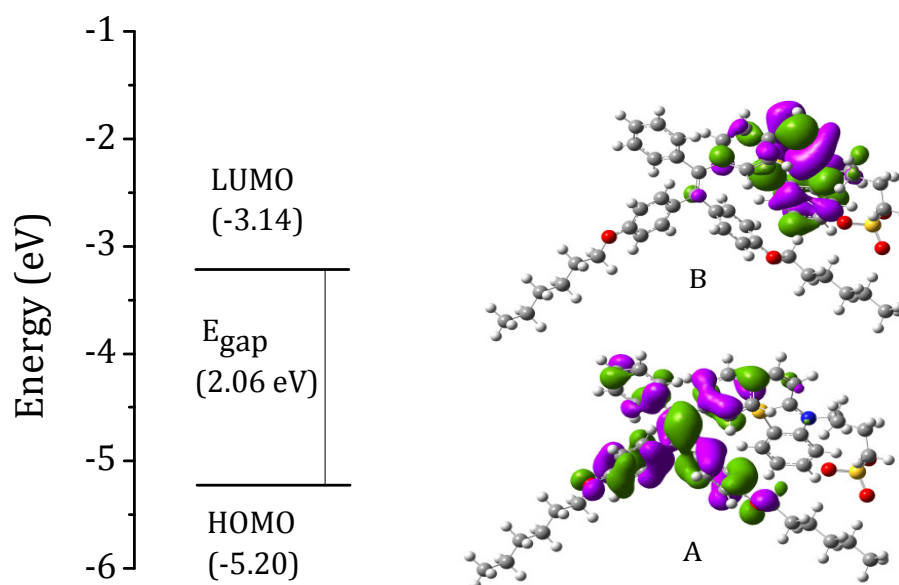## 4.3.2. Photophysical Aspects of the TPE-Benzothiazole Conjugates

The photophysical studies of the TPE-benzothiazole conjugates **4-6** were carried out in different organic solvents and their absorption and fluorescence spectra in acetonitrile are shown in Figure 4.1. The conjugate **4** showed two absorption bands, at 450 and 335 nm having extinction coefficient values of 8.42 ± 0.11 ×10^3 $M^{-1}cm^{-1}$and 1.78 ± 0.23 ×10^4 $M^{-1}cm^{-1}$, respectively. Similar observations were made with the dodecyl conjugate **5** (ε = 8.31 ± 0.21 ×10^3 $M^{-1}cm^{-1}$and 1.72 ±

0.23×10^4 $M^{-1}cm^{-1}$). The peak at 335 nm can be attributed to the characteristic absorption of the TPE chromophore, while the latter band at 450 nm to the intramolecular charge transfer (ICT) from the TPE chromophore to the electron deficient benzothiazole moiety.[2] In contrast, for the non-alkylated derivative, **6**, we observed the ICT band at 425 nm ($\varepsilon = 1.82 \pm 0.2 \times 10^4$ $M^{-1}cm^{-1}$) and a shoulder band at 320 nm ($\varepsilon = 6.42 \pm 0.11 \times 10^3$ $M^{-1}cm^{-1}$). The fluorescence properties of these conjugates **4-6** were investigated in different solvents. Of these systems, the conjugates **4** and **5** showed significantly reduced fluorescence yields, whereas the derivative **6**, exhibited emission maxima at 710 nm and a quantum yield of 0.034 (Inset of Figure 4.1). The photophysical properties of the conjugates **4-6** are summarized in Table 4.1.

Figure 4.1. Normalized absorption spectra of the TPE-benzothiazole (10 μM), conjugates derivatives **4-6** in acetonitrile, **4** (Black), **5** (Red) and **6** (Blue) and inset shows their corresponding emission spectra. Excitation wavelength, 450 nm.

To understand the photophysical aspects, we have carried out theoretical studies of the conjugates **4-6** using the Density Functional Theory (DFT) employing the B3LYP/6-31g* method. All these systems found to exist in twisted conformations. The HOMO and LUMO energy levels were calculated for these conjugates and the band gap energies are found to be 2.06, 2.06 and 2.46 eV for the conjugates **4-6,** respectively. From the optimized geometry, it can be understood that TPE chromophore orbitals predominantly contribute to the HOMO level, while the LUMO levels have been dominated by the orbitals from the benzothiazolium core. These observations were consistent with the absorption properties exhibited by these conjugates. Figure 4.2 shows the optimized energy level diagram of the conjugate **4**, as a representative example of these systems.

Figure 4.2. Energy level diagram containing the A) HOMO and B) LUMO orbitals calculated for the conjugate **4** by using the B3LYP/6-31g* method.

**Table 4.1.** Photophysical properties of the TPE-benzothiazole conjugates **4-6** in acetonitrile.*

TPE	λ_{abs} (nm)	ε_{max} x 10^4 ($M^{-1}cm^{-1}$)	λ_{em} (nm)	E_{gap} Theoretical (eV)	E_{gap} Experimental (eV)
4	450	1.78	a	2.06	2.10
	335	0.84			
5	450	1.72	a	2.06	2.10
	335	0.83			
6	425	1.82	710	2.43	2.34
	320	0.64			

Average of more than two independent experiments; λ_{abs}, absorption; λ_{em}, emission maximum; a, negligible fluorescence; E_{gap} (Theoretical), HOMO-LUMO gaps (band gap) calculated by B3LYP/6-31g; E_{gap} (Experimental), HOMO-LUMO gaps (band gap) calculated from absorption spectra.

The solvatochromic effects on the absorption features of the TPE-benzothiazole conjugates, **4-6**, were studied in different organic solvents of varying polarity like cyclohexane, chloroform, dichloromethane, tetrahydrofuran, acetonitrile, methanol and DMSO. The long wavelength absorption band at *ca*. 426-450 nm of the derivatives **4-6** showed a hypsochromic shift (negative solvatochromism) as the solvent polarity increased. For example, by increasing the polarity from cyclohexane to DMSO, we observed hypsochromic shift of *ca*. 95 nm in
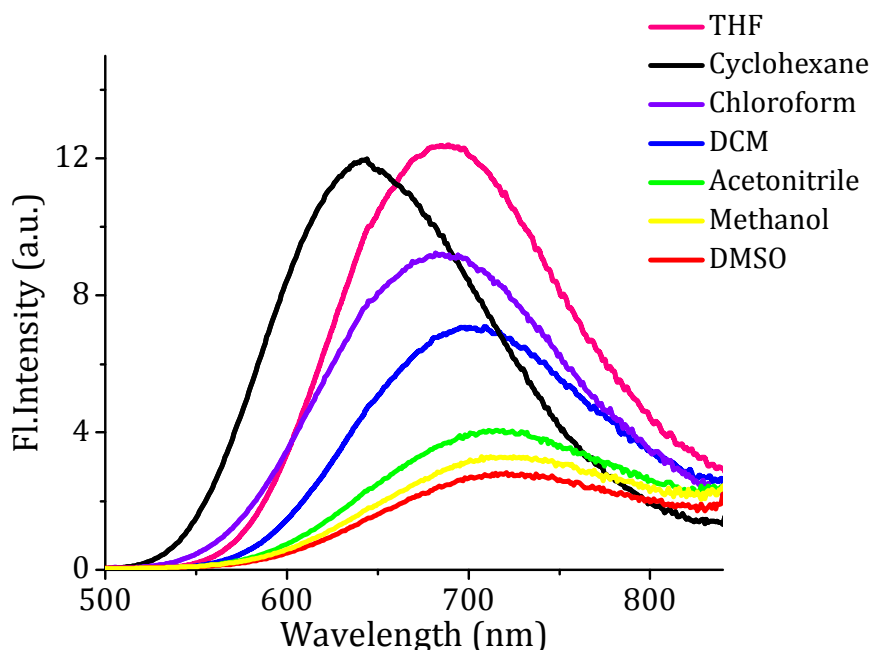
the absorption maximum of **4**. The UV-Vis absorption profile of **4** in different solvents is shown in Figure 4.3. Similar observations were made in the case of the derivative **5** and the model compound **6**, wherein we observed a hypsochromic shift of *ca*. 92 and 75 nm, respectively. These observations can be attributed to zwitter ionic nature of the ground states of these derivatives, which are relatively more polar than their excited states.[4] The intramolecular charge transfer (ICT) bands in the halogenated solvents appeared at wavelengths longer than or closer to that of
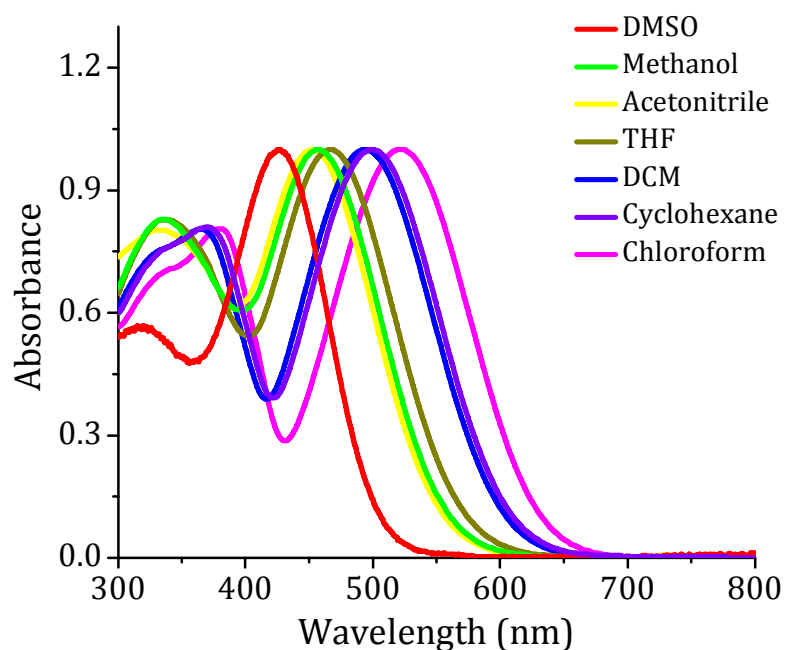
Figure 4.3. Normalized absorption spectra of the TPE-benzothiazole conjugate **4** (5 µM) in solvents having different polarity.

the least non-polar cyclohexane, which may be due to the fact that the halogenated solvents often show variable effects of solvatochromism on the fluorophore with high ICT character.[5]

We have also recorded fluorescence spectra of the alkylated derivatives **4** and **5**, and non-alkyl derivative **6** in different solvents (Figure 4.4) of varying polarity. The conjugates **4** and **5** showed negligible fluorescence in all the solvents investigated. In contrast, the non-alkylated derivative **6**, exhibited the emission maximum (λ_{em}) at *ca.* 640 nm in the nonpolar solvent, cyclohexane, while in DMSO, it showed a bathochromically shifted emission at 716 nm. The solvatochromic properties of the non-alkylated derivative, **6**, are summarized in Table 4.2. The conjugate **6** showed a fluorescence quantum yield of *ca.* 12% in cyclohexane, while in DMSO, we observed significantly reduced quantum yield of *ca.* 1%. The red shifted fluorescence with significantly reduced intensity with the increase in polarity can be attributed to the intramolecular charge transfer (ICT) as reported.[6-8]

Figure 4.4. Fluorescence spectra of the TPE derivative **6** (10 μM) in solvents having different polarity. λ_{ex} at their absorption maximum.

130

Table 4.2. Changes in the absorption and fluorescence properties of the conjugate **6** in different solvents.*

Solvent	Polarity Index	λ_{abs} (nm)	λ_{em} (nm)	Φ_F (%)
Cyclohexane	0.2	476	640	12.2
DCM	3.1	459	699	5.9
THF	4.0	442	686	12.1
Chloroform	4.1	500	684	10.5
Methanol	5.1	432	714	2.2
Acetonitrile	5.8	426	710	3.4
DMSO	7.2	425	716	1.2

*Average of more than two independent experiments. λ_{abs}: absorption maximum, λ_{em}: emission maximum Φ_F: quantum yield of fluorescence determined employing tetraphenylporphyrin (TPP) as the standard.

4.3.3. Self-Assembly Aspects of the TPE Conjugates

To investigate the self-assembly aspects, we have carried out the aggregation studies of the conjugates **4-6** in various mixtures of water/acetonitrile. The TPE-benzothiazole conjugate **4**, showed two absorption bands, at 450 and 335 nm in acetonitrile. However, by gradually increasing the percentage of water in acetonitrile solution, we observed significant change in the absorption spectra of **4** as shown in Figure 4.5. Initially, we observed negligible changes upto water fraction

(f_w) ≤ 60%, but when it was increased to *ca*. 70%, we observed a profound

hypochromicity of *ca*. 49% at 450 nm along with a 27 nm bathochromic shift. The

peak at 335 nm, on the other hand, showed red shifted absorption to 345 nm along

with the increase in the intensity under these conditions. Similar observations were

made with the derivative **5**. It showed the hypochromicity of *ca*. 32% at 450 nm,

when the water fraction was increased to *ca*. 50%. In contrast, the non-alkylated
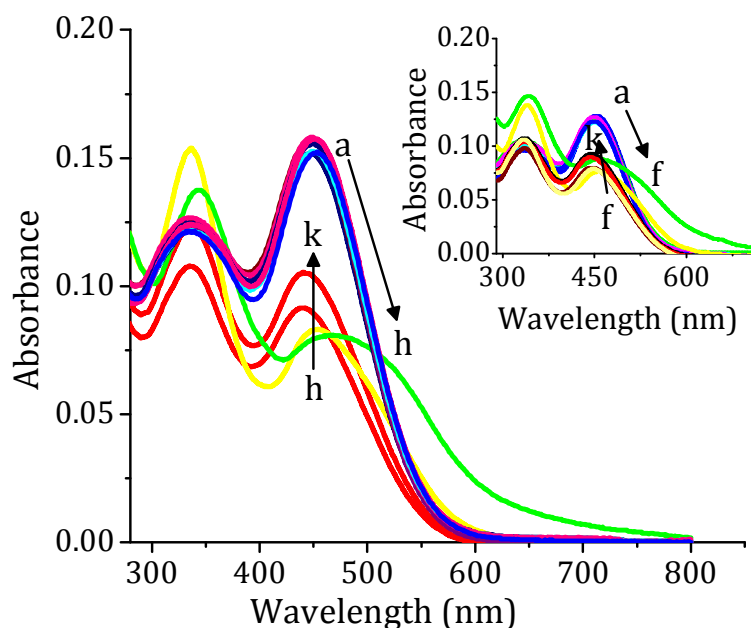
Figure 4.5. Changes in the absorption spectra of **4** (10 μM) in various water/acetonitrile mixtures. Inset shows changes in the absorption spectra of **5** (10 μM) under similar conditions. Percentage of water (f_w) a) 0, h) 70, f) 50 and k) 99%.

derivative **6**, showed a gradual decrease in the intensity of absorbance at 425 nm

with the increase in water fraction (Figure 4.6). In this case, we observed a red shift

of 7 nm in the absorption band from 325 nm to 332 nm. From these spectral

changes, it was clear that as the percentage of the water fraction was increased, there were prominent changes in the absorption properties of the conjugates **4**-**6**. The observation of bathochromically shifted absorption maximum with the increase in the percentage of water indicates the formation of J-type aggregates as reported in the literature.[23]
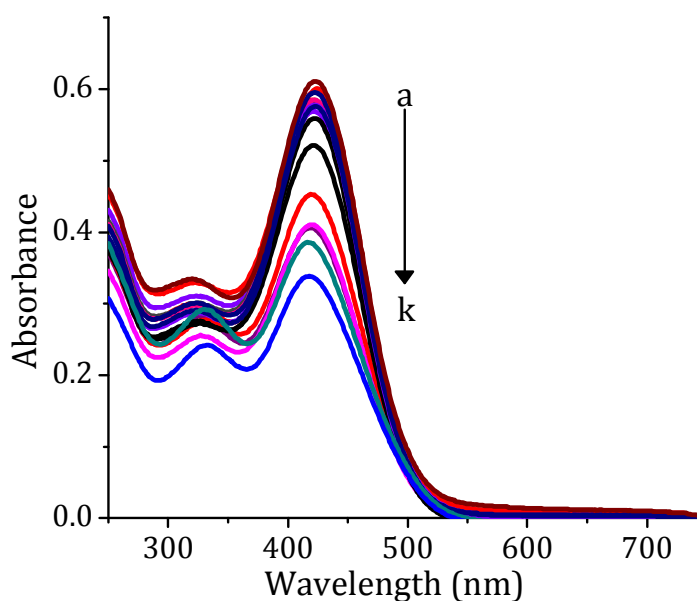
Figure 4.6. Changes in the absorption spectra of **6** (10 μM) in various water/acetonitrile mixtures. Percentage of water (f_w) a) 0 and k) 99.

In the emission spectrum, we observed significant changes with the increase in the water fraction. The conjugate **4** showed negligible fluorescence in acetonitrile. Upon increasing the water fraction to *ca*. 50%, we observed non-significant changes in the emission spectrum. Eventually, at f_w of *ca*. 70%, as shown in Figure 4.7, we observed a significant enhancement in the emission intensity of the conjugate at 715 nm. From the absorption studies, we could get the indication of aggregate formation

at *ca*. 70% water/acetonitrile mixture. Since the tetraphenylethene (TPE) based systems are active as aggregation induced emissive (AIE) molecules, the observed profound enhancement in the emission can be due to the restricted intramolecular rotation (RIR) of the phenyl substituents.[11-13] However, with the further increase in the water percentage, we observed a decrease in the fluorescence intensity. Inset of
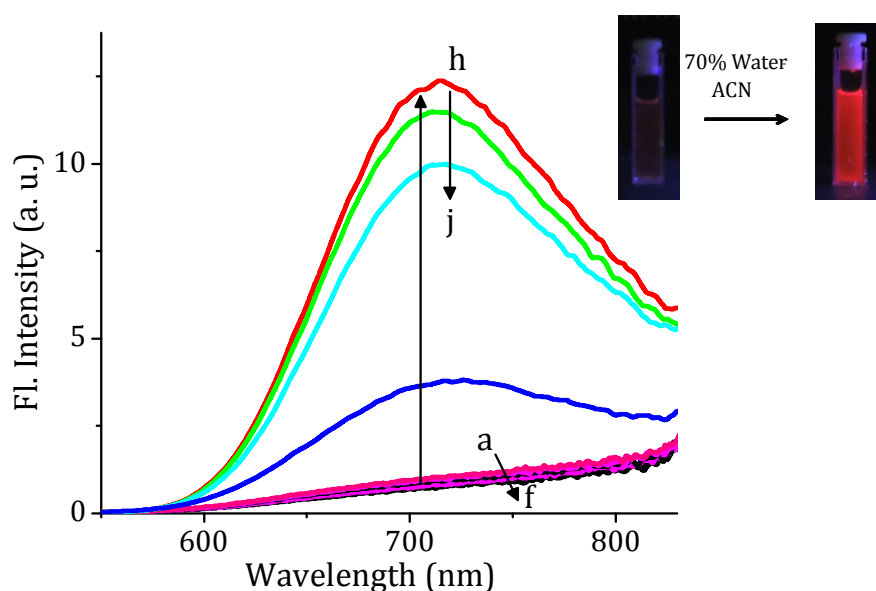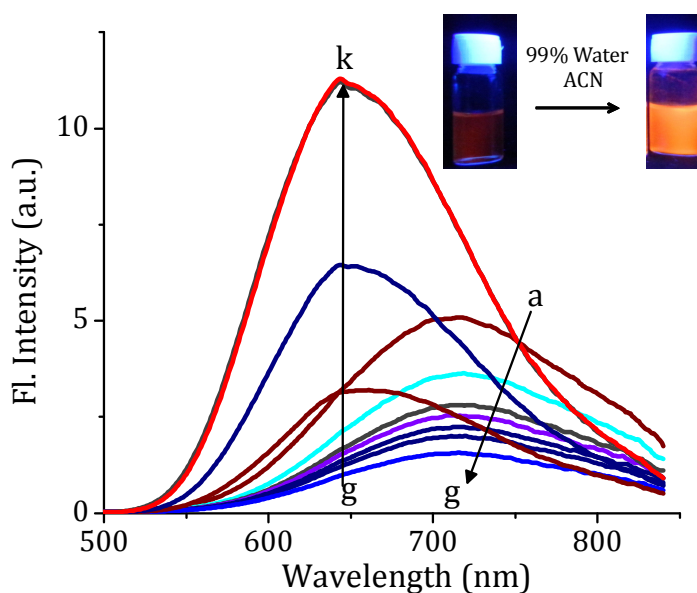

Figure 4.7. Changes in the emission spectra of the conjugate **4** (10 μM) in various water/acetonitrile mixtures. Percentage of water (f_w) a) 0, h) 70 and j) 99%. Inset shows the visual observation of fluorescence changes of **4** in acetonitrile and when water fraction was increased to *ca*. 70%. Excitation wavelength, 450 nm.

Figure 4.7 shows the visual fluorescence changes when the water fraction was changed from *ca*. 0% to *ca*. 70%.

In the case of the dodecyl derivative **5**, similar enhancement in the fluorescence intensity was observed at water fraction (f_w) of *ca*. 50%. In contrast,

the non-alkylated derivative **6** exhibited an initial fluorescence at 710 nm, with a fluorescence quantum yield (Φ_F) of *ca.* 3.4%. On increasing the percentage of water fraction (f_w), we observed a decrease in fluorescence intensity up to $f_w \leq 60\%$ as shown in Figure 4.8. Interestingly, when the water fraction was further increased to *ca.* 60%, we observed a prominent enhancement in the fluorescence intensity with a


Figure 4.8. Changes in the emission spectra of **6** (10 μM) in various water/acetonitrile mixtures. Percentage of water (f_w) a) 0, g) 60 and k) 99%. Inset shows the visual observation of fluorescence changes of **6** in acetonitrile and 99% water-acetonitrile mixture. Excitation wavelength, 425 nm.

hypsochromic shift of *ca.* 60 nm. We observed a maximum enhancement in the fluorescence intensity at 650 nm, when the water fraction was increased to *ca.* 95% and exhibited a fluorescence quantum yield (Φ_f) of 13.2%. On further increasing the

water fraction to *ca.* 99%, we observed negligible changes in the emission intensity for **6**. Inset of the Figure 4.8 shows the visual fluorescence changes when the water fraction was changed from *ca.* 0% to *ca.* 99%.

We have plotted the changes in the emission peak intensity at 715 nm for **4** and **5** and at 650 nm for **6** versus water fraction in the water/acetonitrile mixtures. As shown in Figure 4.9, we observed that the TPE-benzothiazole conjugates **4-6** exhibited aggregation induced enhanced emission (AIEE). The initial solvent depended studies and theoretical studies confirmed the existence of the
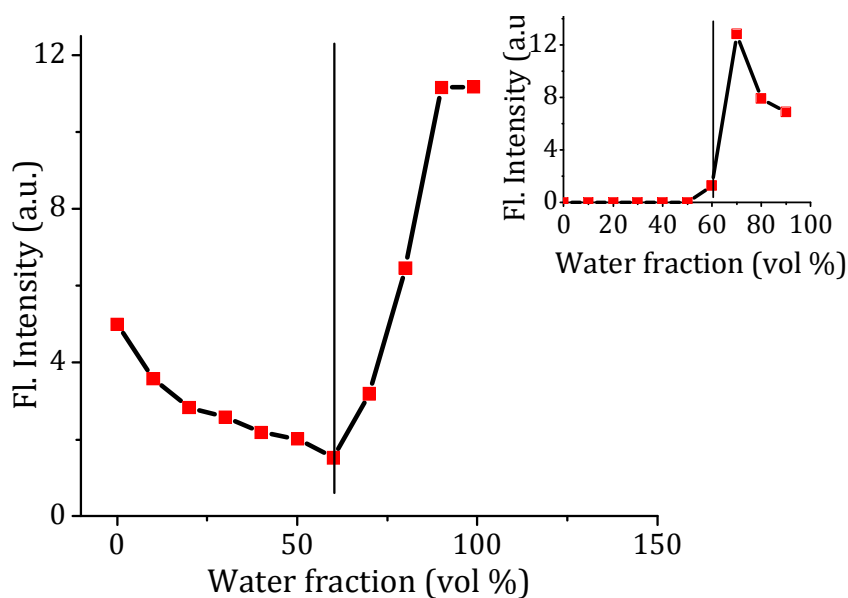
Figure 4.9. Plot of fluorescence intensity versus water fraction in the water-acetonitrile mixture of **6** [10 µM], (λ_{em}=650 nm) and inset shows the changes for **4** [10 µM], (λ_{em}=715 nm) under similar conditions.

intramolecular charge transfer (ICT) mechanism for these conjugates. In the solvent mixtures like water/acetonitrile, we observed both ICT as well AIE effects (Figue

4.9). For example in the case of **6**, when the water content was increased initially upto *ca.* 60%, there was a decrease in the initial emission intensity at 710 nm. When the water percentage was increased to *ca.* 95%, we observed the prominent enhancement in emission intensity at 650 nm, confirming the proposed hypothesis.

To have a better understanding of the fluorescence changes observed in the monomeric as well as in the aggregated state, we have analyzed the emission decay dynamics by varying the percentage of water f_w in acetonitrile solution of TPE derivatives through time-resolved fluorescence technique. We observed different decay dynamics for the TPE derivatives as shown in Figure 4.10. For example, the fluorescence decay profile of the conjugate **6** in acetonitrile showed a monoexponential decay with a lifetime of 0.4 ns, which corresponds to the TPE
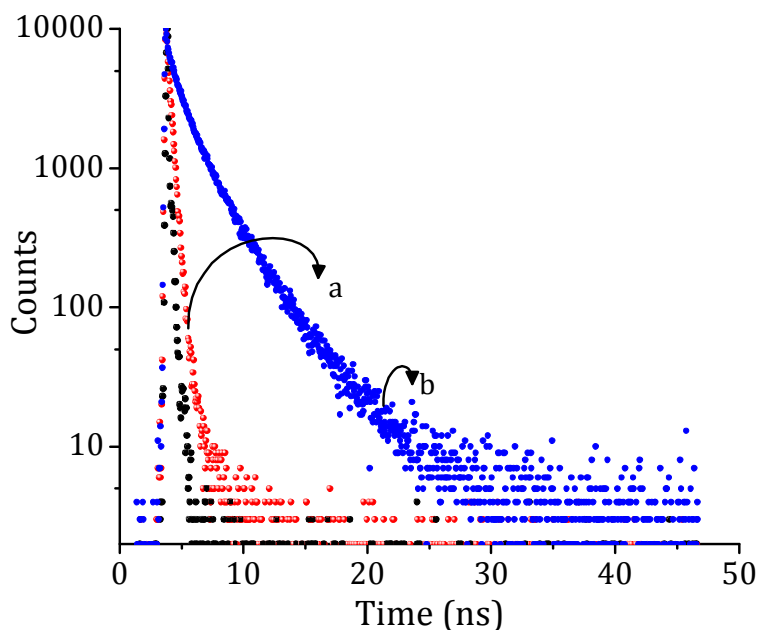
Figure 4.10. Fluorescence decay profiles of **6** (10 μM) in a) acetonitrile b) 95% water/acetonitrile mixtures. Excitation wavelength, 440.

chromophore. Interestingly, in the fluorescence decay profile of **6** in the water-acetonitrile mixture having 95% water, we observed a double-exponential decay. The short lived component was the minor species (*ca.* 9%) with a lifetime of 1.4 ns, while the major component (*ca.* 91%) exhibited a lifetime of 5.7 ns which can be attributed to the aggregated species (Table 4.3). This longer lifetime for the aggregate excited state has been in conjunction with our observation of the corresponding fluorescence quantum yield enhancement in the aggregated state. Similar observations were made in fluorescence decay dynamics of the alkylated derivative **4** and **5**, wherein the aggregated state exhibited a double exponential decay. We observed a longer lifetime of 3.87 ns and 2.15 ns for **4** and **5**, respectively.

Table 4.3. Summary of fluorescence properties of the TPE conjugates **4-6**.*

| TPE	Φ_F (%) CH$_3$CN	Φ_F (%) (H$_2$O:CH$_3$CN)	τ (ns) acetonitrile	τ (ns) (H$_2$O:CH$_3$CN)
4^x	a	7.6	a	T$_1$=0.96 (10%), T$_2$=3.87 (90%)
5^y	a	7.5	a	T$_1$=0.53 (21%), T$_2$=2.15 (79%)
6^z	3.4	13.2	T$_1$=0.40 (100%)	T$_1$=1.40 (9%), T$_2$=5.66 (91%)

*Average of more than two independent experiments. a, negligible fluorescence; Φ_F, quantum yield of fluorescence; τ, Fluorescence lifetime; x, y and z indicates the percentage of water in water/acetonitrile mixture. x=70%, y= 50% and z= 95%

4.3.4. Nature of Self-Assembled Structures of the TPE Conjugates

With a view to understand the nature of the aggregates formed, we have carried out temperature, time and ionic strength dependent studies employing UV/Vis absorption and fluorescence techniques as well as the contour map of the emission spectra and powder XRD studies. In the temperature dependent studies, we observed a reversible transition of the aggregates to the monomeric species, when we increased the temperature from 25 °C to 80 °C for all the derivatives. In the case of **4**, an increase in the temperature from 25 °C to 80 °C, led to a reduction in the intensity of absorption at 477 nm (aggregated state), with a concomitant increase in the intensity of the absorption at 450 nm. In addition, we observed a
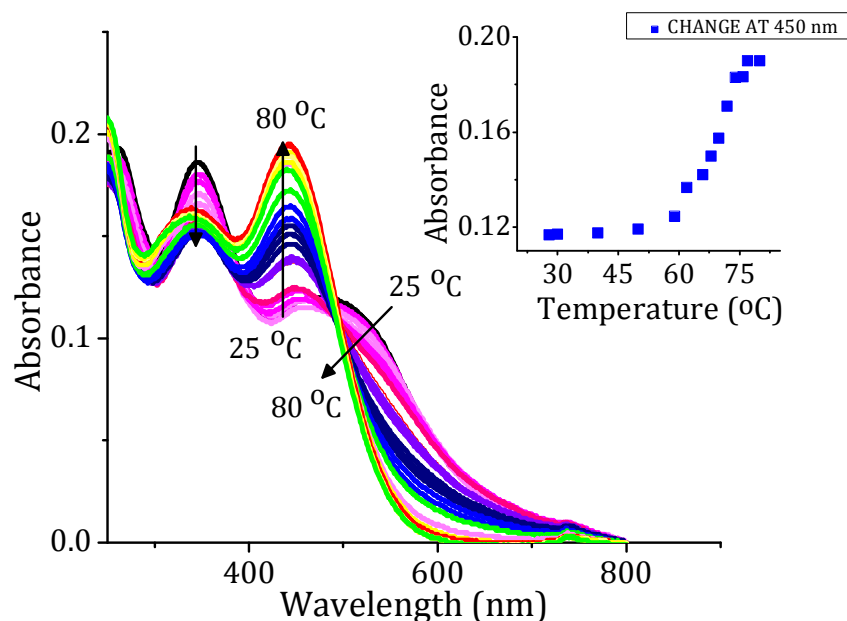
Figure 4.11. Temperature-dependent absorption spectra of the conjugate **4** [10 μM] in 70% water/acetonitrile mixture and the inset shows the secondary plot of the changes observed at 450 nm as a function of temperature.
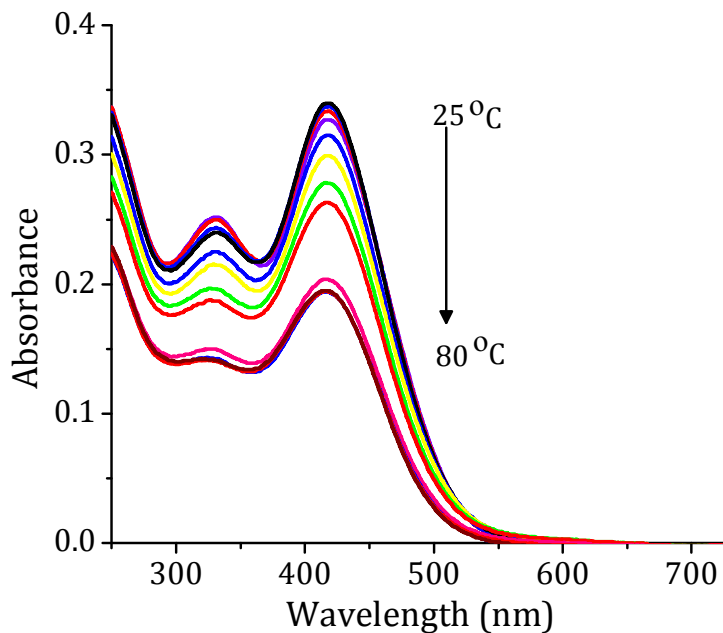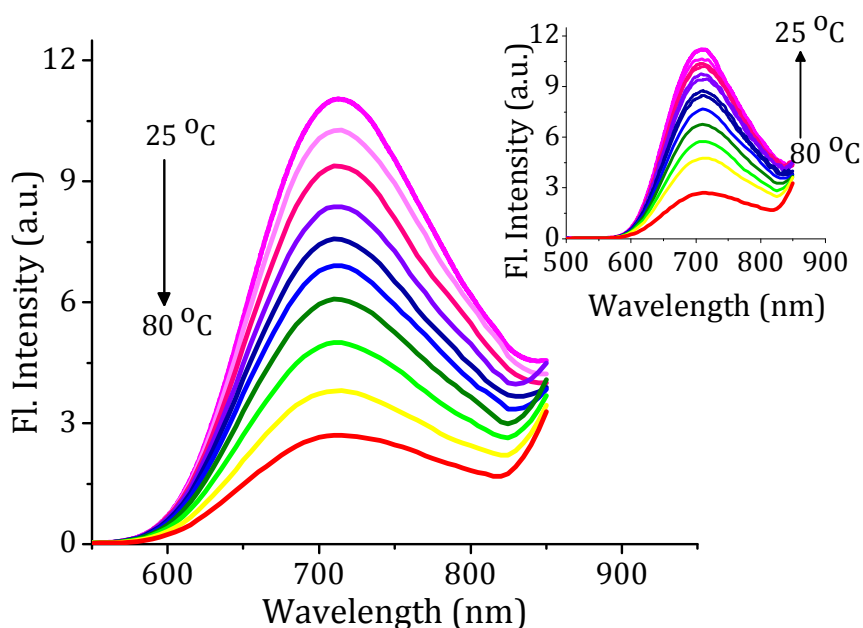
Figure 4.12. Temperature-dependent absorption spectra of the conjugate **6** (10 μM) in 95% water/acetonitrile mixture.

decrease in the intensity of the absorbance at 334 nm (Figure 4.11). In the cooling cycle, we observed the reverse process, indicating thereby the reversibility of the aggregation phenomenon. Inset of Figure 4.11 shows the plot of change in the absorbance at 450 nm with increase in temperature from 25 °C to 80 °C. Similar observations were made with the derivative **5**. In contrast, the non-alkylated derivative **6** (Figure 4.12), exhibited (f_w = 95%) only a decrease in the absorbance of the aggregated solution with increase in temperature from 25 °C to 80 °C. These observation indicate the fact that the aggregates formed from **6** are different from those of the alkylated TPE conjugates **4** and **5**.

Furthermore, we have investigated the effect of temperature on the emission profile of the aggregated form of the conjugates **4**-**6**. When the temperature of the

aggregated solution of the conjugate **4** (*ca.* 70% water/acetonitrile) was varied from 25 °C to 80 °C, we observed a prominent decrease in the emission intensity indicating thereby the dissociation of the aggregates at this temperature (Figure 4.13). However, in the cooling cycle, we observed a complete revival of the emission intensity at 715 nm, indicating thereby the reformation of the aggregates. Similar thermo-reversible changes were observed in the emission spectra of the conjugates **5** and **6** derivatives as shown in Figure 4.14.


Figure 4.13. Heating cycle of the temperature dependent emission spectra of the conjugate **4** [10 μM] in 70% water/acetonitrile mixture and inset shows the corresponding cooling cycle. Excitation wavelength, 450 nm.
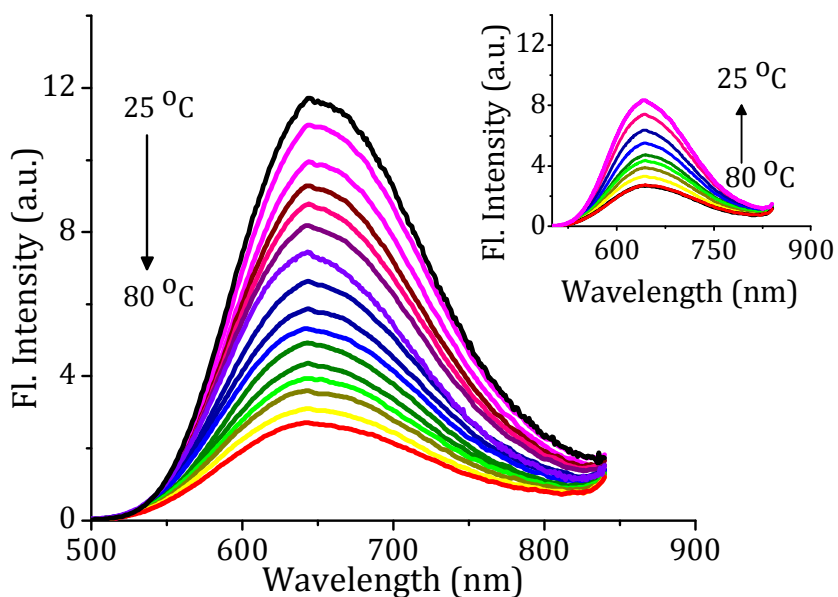
Figure 4.14. Heating cycle of the temperature-dependent emission spectra of the conjugate **6** [10 μM] in 99% water/acetonitrile mixture and inset shows the corresponding cooling cycle. Excitation wavelength, 425 nm.

observed negligible changes in the absorbance and fluorescence intensity of the aggregates with the time for all the conjugates **4-6**. For example, Figure 4.15 shows the emission spectra of the conjugate **6** over a period of 5 h, which exhibited negligible changes under these conditions. Similar observations were made with the conjugates **4** and **5**. Further to investigate the involvement of electrostatic interactions in the formation of aggregates, we have investigated the changes under different salt concentrations (0-1M NaCl). As shown in the inset of Figure 4.15, and with the increase in the ionic strength of the medium, we observed negligible changes in the fluorescence intensity at 650 nm for the conjugate **6**. Similar observations were made with **4** and **5** under these conditions. These results confirm

the involvement of hydrophobic and van der Waals interactions and rule out the role

of the electrostatic interactions in the formation of the aggregates of **4-6**.
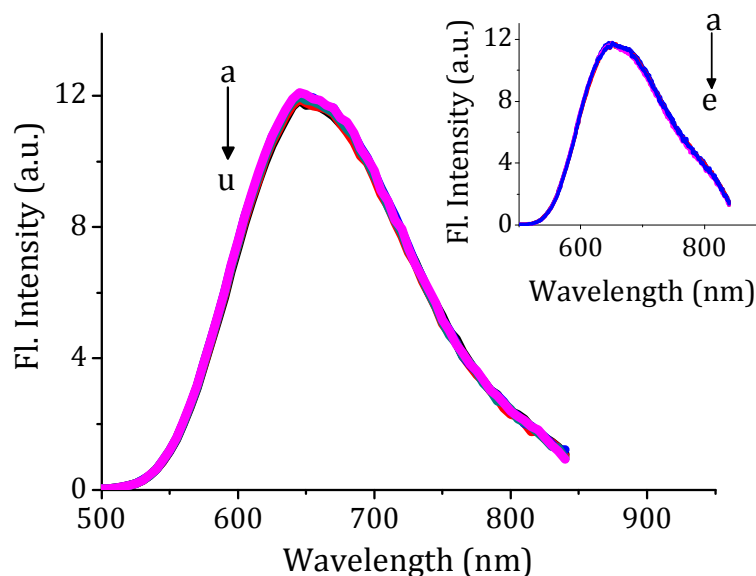
Figure 4.15. Time dependent emission spectra of the conjugate **6** [10 μM] in 95% water/acetonitrile mixture, a) 0 and u) 5 h. Inset shows the emission spectra of the conjugate **6** [10 μM] in 95% water/acetonitrile mixture by varying the ionic strength, a) 0 and e) 1 M NaCl.

In order to understand the nature of the aggregates formed by increasing the water

percentage, matrix scan experiments of the conjugates **4-6** were also carried out.

While taking the excitation spectra of the aggregated state, we observed a broad

spectrum, which could be attributed to the involvement of both the aggregate and

monomer species. We have further carried out matrix scan experiments in which

fluorescence spectra were recorded at excitation wavelengths between 300 and 550

nm. By taking the conjugate **6** as a representative example, we observed the

emission spectra (Figure 4.16A), which originated mainly from excitation of the monomer band in the 400-450 nm region. The recorded emission intensities of the conjugate **6** in 95% water/acetonitrile are shown in Figure 4.16B. It can be clearly seen from Figure that there was an equal contribution of both the J-type aggregates (~310-340 nm) as well as monomeric species for the observed emission at 650 nm. Similar observations were made from both the species (aggregate and monomer) of the conjugates **4** and **5**. Results of these contour experiments indicate the fact that the observed aggregates of the TPE-benzothiazole conjugates were of J-type and that they were thermodynamically quite stable, wherein weak non-covalent interactions play a major role as confirmed through detailed photophysical stuides.
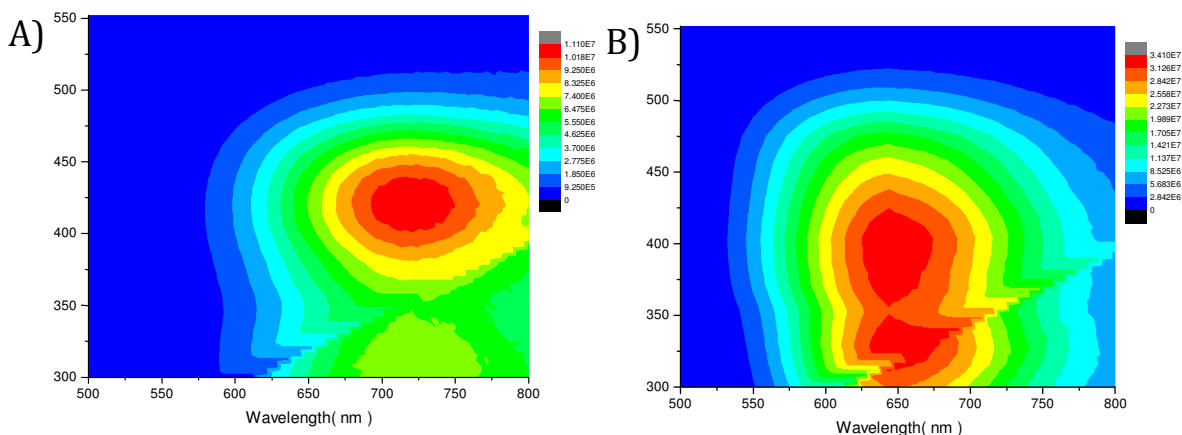

Figure 4.16. Contour map of the observed fluorescence intensity as a function of the fluorescence excitation and emission wavelengths of the conjugates **6** (15 µM) in A) acetonitrile alone and B) 95% water/acetonitrile mixture.

The solid state packing pattern was investigated through powder XRD analysis of the compounds **4-6**. For example, the conjugate **4** exhibited a peak

corresponding with a d-spacing of 3.1 Å, which could be attributed to the C-H...π-stacking distance between two molecules. Further, we observed diffraction peak with a d-spacing of around 28.3 Å, which corresponds to the edge to edge packing of the alkyl side chains of the conjugate in the same plane. The presence of higher order reflections at 5.4 Å, 7.7 Å, and 10.18 Å may correspond to end-to-end or alternate distances between two molecules and it indicates the fact that a high degree of ordering exists in the case of **4**. We observed similar diffraction pattern in the case of the dodecyl derivative **5**. In contrast to these conjugates, the higher ordered diffraction patterns were absent for the non-alkylated derivative **6**. These
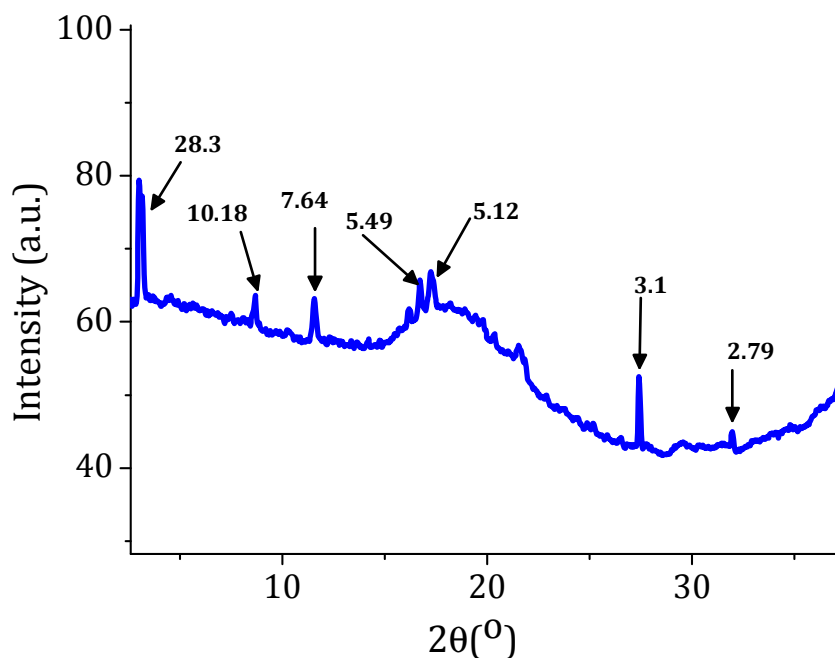

Figure 4.17. Powder XRD pattern of the TPE-benzothiazole conjugate **4**.

results confirm the importance of the alkyl chains. The linear alkyl substituents present in the case of the conjugates **4** and **5** allow a close packing of the conjugated

chains into very long, regular stacks, resulting in the ordered architectures, while such interactions were absent in the case of the non-alkylated conjugate **6**.

### 4.3.5. Analysis of Morphological Aspects of Self-Assemblies of 4-6

To understand the self-assemblies formed from the conjugates **4-6**, we have carried out their morphological analysis through dynamic light scattering studies (DLS), scanning electron microscope (SEM) and transmission electron microscope (TEM) under different conditions. The TPE conjugates **4-6** in acetonitrile solution showed negligible formation of nanoparticles as analyzed by the particle size analyzer. However, by increasing in the water percentage to ca. 70% in the solution of the conjugate **4**, we observed the larger aggregates with an average size of *ca*. 650 nm (Figure 4.18A).
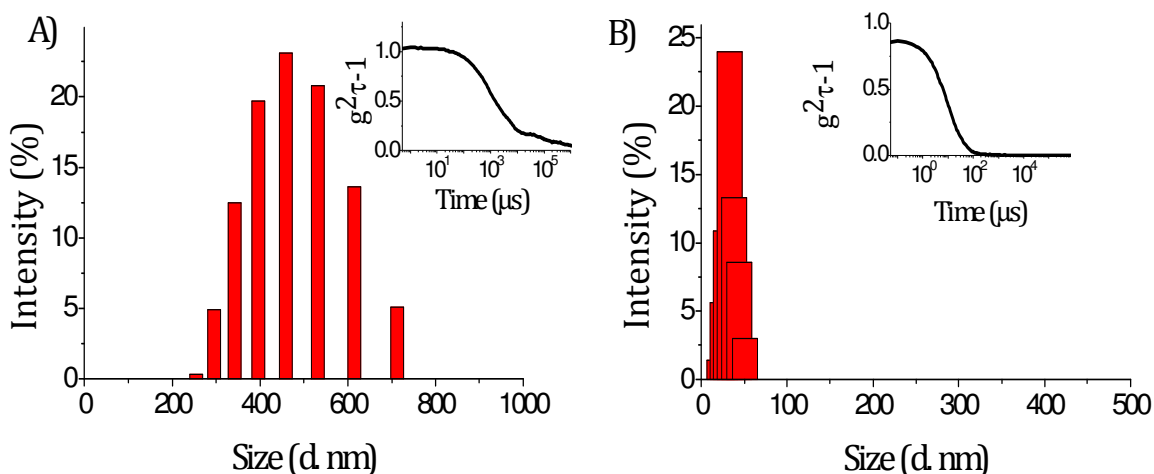

Figure 4.18. DLS analysis of **4** (10 μM) in A) 70% H_2O/acetonitrile mixture and B) 99% H_2O/acetonitrile mixture. Insets show the corresponding correlograms.

Further increase in the water percentage to *ca.* 99% resulted in the formation of nanoparticles of average size of *ca.* 45 nm (Figure 4.18B). Similar DLS data was obtained in the case of the conjugates **5** and **6**. In these case we observed the formation of nanoparticles of size *ca.* 47 and 32 nm, respectively for the conjugates **5** and **6**. The solutions of the conjugates **4-6** in various acetonitrile-aqueous mixtures were found to be homogeneous and visually transparent without precipitate, even at f_w as high as *ca.* 99%, suggesting thereby that the aggregates form nanoparticles under these conditions.

To have a better understanding of the self-assemblies of the TPE derivatives with changes in the percentage of water-acetonitrile solvent mixtures, we have further carried out the morphological analysis through TEM and SEM techniques. For example, in the case of **4**, when the water fraction was increased to *ca.* 70%, we observed the rod shape architectures of ∼ 780 nm in diameter and ∼ 12 μm in length as evidenced through the TEM and SEM analysis (Figure 4.19). Similarly, with the dodecyl derivative **5**, we observed the nanorods having ∼ 720 nm in diameter and 15 μm under similar conditions. In contrast, the non-alkylated derivative **6** exhibited aggregate of nanoflowers at a f_w ∼ *ca.* 90-95% (Figure 4.20). In these cases, the aromatic segments present form the cylindrical core in a radial arrangement and allowed space-filling by the long alkyl chains. Furthermore, the length of the flakes of petals formed in the case of the non-alkylated system **6** was found to be ∼ 750 nm and which finally resulted in the flower morphology.
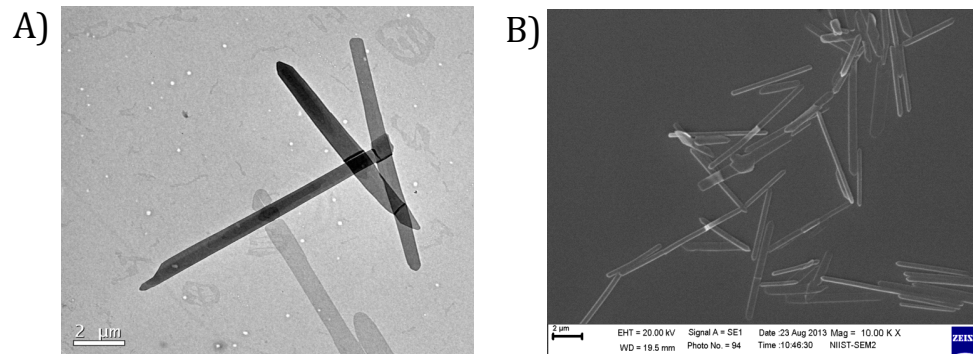
Figure 4.19. A) TEM and B) SEM image of the nanorods formed from the conjugate **4** (10 µM) in water/acetonitrile mixtures with f_w of 70%.
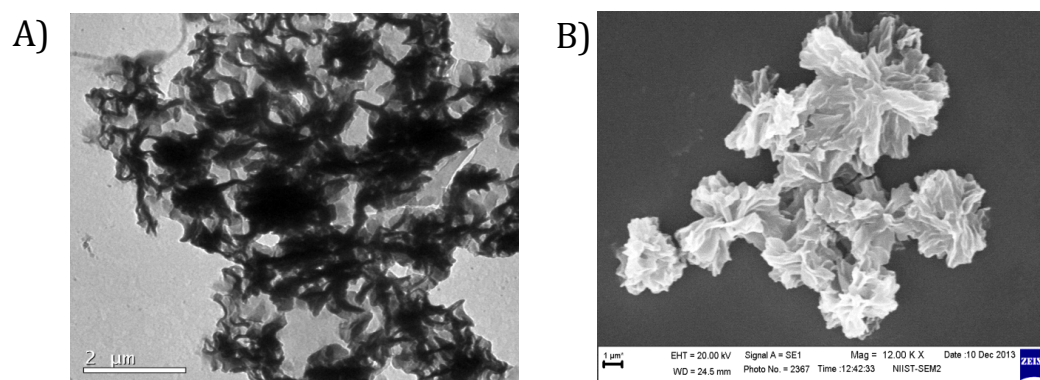

Figure 4.20. A) TEM and B) SEM images of the nanoflowers formed from the conjugate **6** (10 µM) in water/acetonitrile mixtures with f_w of 95%.

Further we have carried out the morphological analysis at a water fraction of *ca.* 99% since the larger aggregates dissembled into nanoparticles under these conditions as analyzed by DLS. For example, the conjugate **4**, which showed initially nanorod like morphology (Figure 4.21), transformed into nanoparticle of average size of ∼ 10 nm with the increase in the water content (Figure 4.21C). Similar

disassembled structures were obtained for the conjugate **5** and **6**, which finally gave the nanoparticles with an average size of ~10 nm under similar conditions.
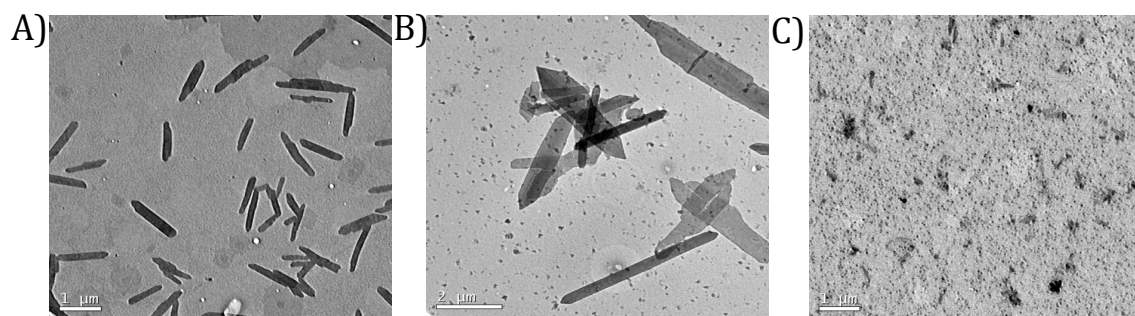

 Figure 4.21. TEM images of the disassembly of the nanorods to nanoparticles of the hexyl derivative **4** [10 µM], in various water/acetonitrile mixtures with water fraction *fw* of A) 60, B) 80 and C) 99%.
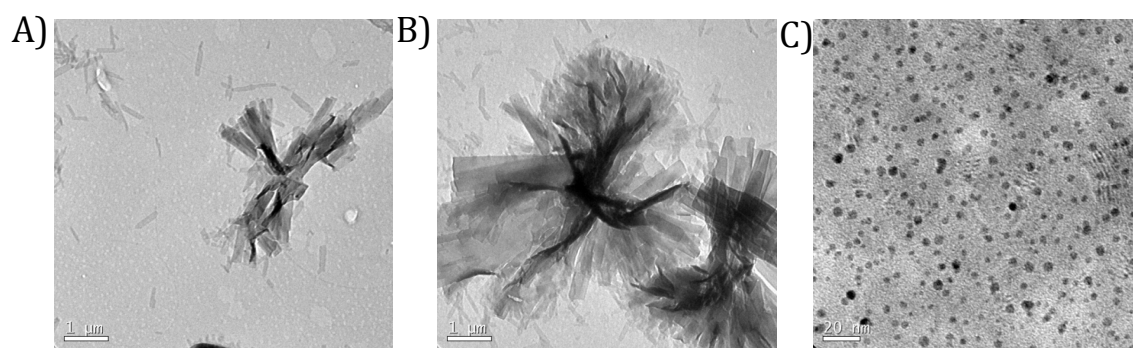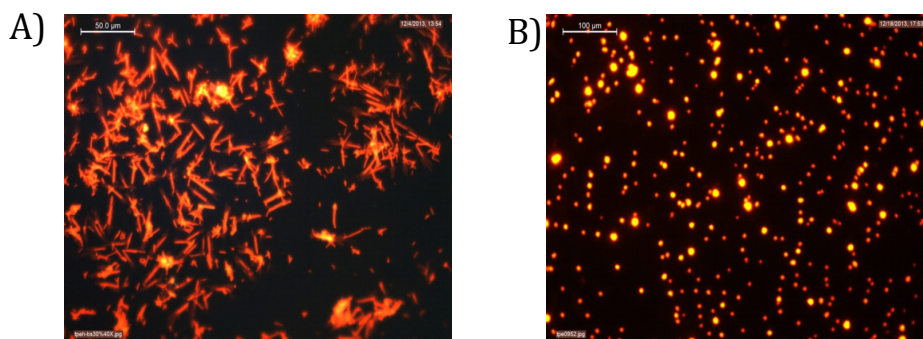

Figure 4.22. TEM images of the aggregates formed by **6** [10 µM] in A) 80, B) 90 and C) 99% water/acetonitrile mixture.

To gain more insights in the aggregation, we have carried out the electron diffraction (ED) studies. From the electron diffraction (ED) measurements it was evident that the aggregates formed were found to be highly crystalline in the case of the conjugates **4** and **5**. For example, the conjugate **4**, at *ca*. 70% water/acetonitrile

mixture, showed an electron diffraction pattern which confirms to the crystalline nature of the self-assembled state (Figure 4.23A). When we have increased the water content to *ca.* 99%, the aggregates formed showed the amorphous nature (Figure 4.23B) without any diffraction pattern. In contrast, the self-assembled structures of the conjugate **6** were found to be amorphous. Furthermore, fluorescence microscopic analysis showed that the nanorods formed from **4** (Figure 4.24A) and **5** as well as the nanoflowers from **6** (Figure 4.24B) exhibited bright red
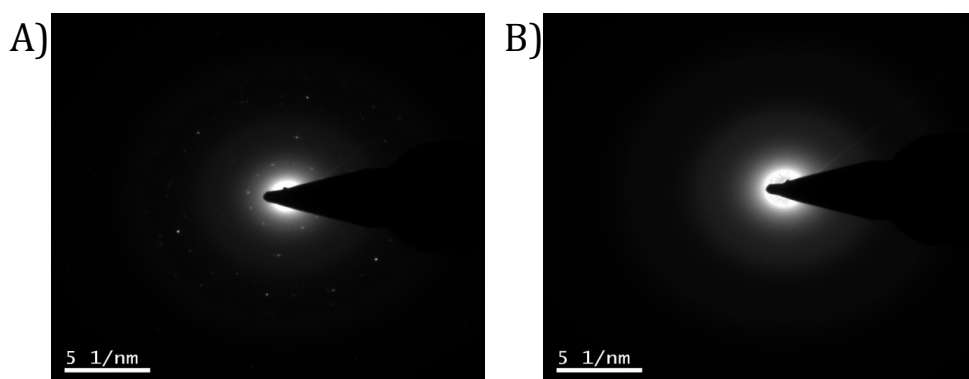
Figure 4.23. A) ED pattern of the nanorods formed from **4** (10 µM) in 70% water-acetonitrile mixture B) **4** (10 µM) in 99% water-acetonitrile mixture.


Figure 4.24. Fluorescence images of the aggregates formed from A) **4** and B) **6** at 70 and 95% water fraction in acetonitrile. Excitation wavelength, 488 nm.

emission upon excitation by a 488 nm laser. Moreover, the nanoparticles formed at *ca*. 99% of water/acetonitrile solutions from the conjugates **4-6** also showed similarly high red emission thereby confirming their potential use in fluorescence imaging applications.

4.3.6. *In Vitro* Cytotoxicity and Imaging Studies

The photophysical and morphological studies suggest that the TPE-benzothiazole conjugates under investigation are highly emissive in the aggregated state and form nanoparticles at *ca.* 99% water/acetonitrile mixtures. To test the cytotoxicity of the conjugates **4-6**, we have employed prostate cancer (PC-3) cell lines and colorimetric MTT assay by adopting standard protocols. In the presence of the nanoparticles of the TPE derivatives, we observed negligible toxicity in PC-3 prostate cancer cells similar to those in control cell lines (Figure 4.25A). It was found that more than *ca*. 97% cells were alive even after 48 h of incubation with the conjugates **4** and **6** (Figure 4.25B) while **5** showed a survival rate of *ca*. 92%. Evidently, from the concentration dependent studies, we observed that the nanoparticles derived from TPE conjugates **4** and **6** showed non-toxicity even upto 50 µM while **5** showed the cytocompatibility only up to 25 µM.

We have carried out the flow cytometric experiments using PC-3 human prostate cancer cells to demonstrate the ability of the TPE derivatives for *in vitro* cell tracing applications. PC-3 cancer cells were first incubated with different concentrations of the nanoparticles in *ca.* 99% water/acetonitrile mixtures for
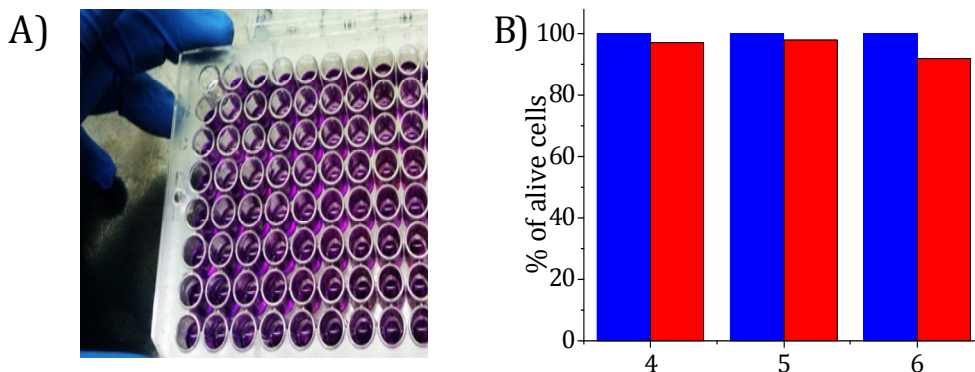
Figure 4.25. A) Purple color of the 3-(4,5-dimethylthiazol-2-yl)-2,5-diphenyl-tetrazolium bromide in living cells in presence of the NPs of the conjugates **4**-**6**. B) Metabolic viability of prostate cancer (PC-3) cell lines, 12 h (blue), and 48 h (red).

overnight at 37 °C. The fluorescence profiles were recorded using flow cytometry by counting 10000 events employing excitation wavelength of 488 nm. Figure 4.26 shows the labeling rate of the TPE nanoparticles derived from the conjugate **4** towards PC-3 cells. It could be well understood from the results that more than *ca.* 95% of the cells were labeled by 1 μM concentration of the conjugate. We have carried out the similar experiments with the conjugates **5** and **6**. The labeling rate was found to be efficient in the case of the alkylated conjugates **4** and **5** when compared to the non-alkylated derivative **6**. We have also carried out the time-dependent flow cytometric analysis with the TPE NPs and found that almost *ca.* 98% labeling of this cell line was observed within 5 min of incubation at 5 μM concentration of the alkylated derivatives.

The application of the AIE active organic nanoparticles of the conjugates **4**-**6** for *in vitro* cellular imaging was investigated employing the confocal laser scanning
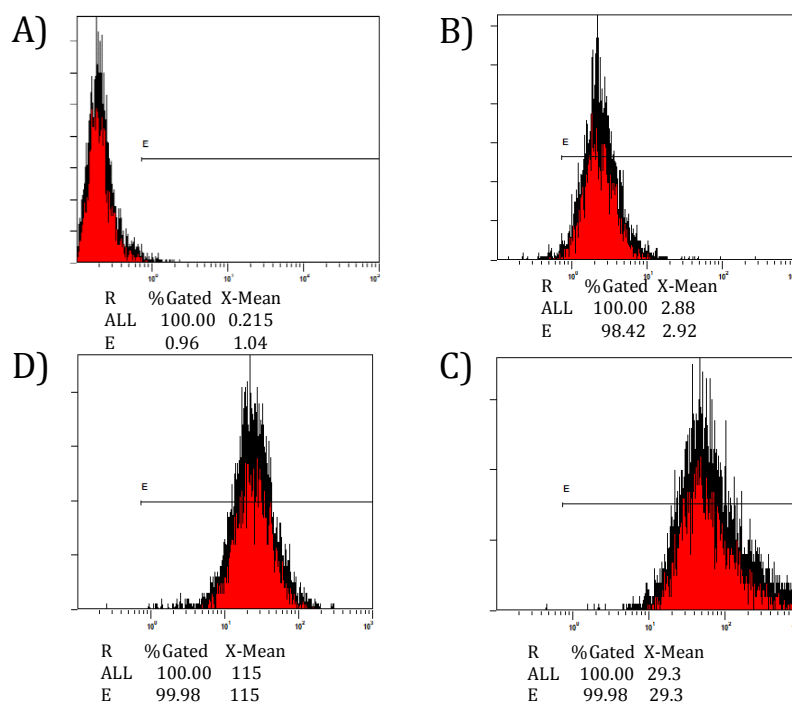
Figure 4.26. Flow cytometry histograms of PC-3 human prostate cancer cells after overnight incubation with A) 0 B) 1 C) 5 and D) 10 µM of the conjugate **4** at 37 °C. The untreated PC-3 human prostate cancer cells were used as the control.

microscopy (CLSM). After incubation with the TPE-NPs suspension (5 µM) for 2 h at 37 °C in the culture medium, PC-3 prostate-cancer cells were fixed and the cell nuclei were stained with 4′,6-diamidino-2-phenylindole (DAPI). For example, Figure 4.27A shows the CLSM image of PC-3 cell lines incubated with the NPs of the conjugate **4**. The cells were imaged by CLSM with a 488 nm laser excitation and the fluorescent signals were collected at above 650 nm for the TPE-NPs and 560 nm for DAPI, respectively. The blue fluorescence observed in Figure 4.27 was due to DAPI, while the NPs of the conjugate **4** exhibited the red fluorescence. DAPI stained the nucleus of the cells and while the red fluorescence from the NPs was observed from the
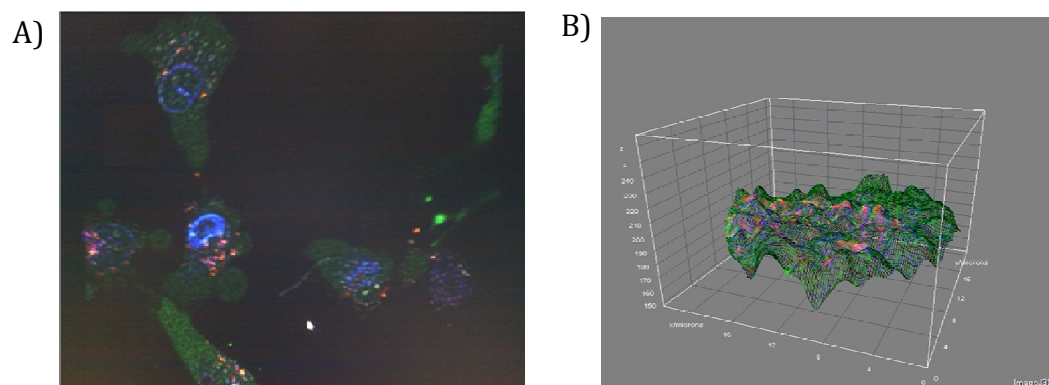
Figure 4.27. A) CLSM images of PC-3 prostate cancer cells after incubation with **4** (5 µM) for 2 h and counter staining with 4',6-diamidino-2-phenylindole (DAPI) at 37 °C. B) 3D plot of the corresponding CLSM image.

cellular cytoplasm as shown in Figure 4.27A. Figure 4.27B is the 3D analysis of the CLSM image, which further confirmed the internalization of the NPs in the cytoplasm of the cells. To further confirm the internalization of the TPE-NPs by the cells, we have carried out the Z-axis scanning of the fluorescent confocal microscope images. We observed the nanoparticles internalization by examining the orthogonal views (Figure 4.28). The Z-axis scanning of the TPE-benzothiazole nanoparticles of **4-6** incubated with the PC-3 prostate cancer cell lines indicated that the red fluorescent nanoparticles were not merely adhered to the cell surface but were also present in the cell cytoplasm. These results demonstrate that the TPE-NPs derived the conjugates **4-6** can effectively act as NIR fluorescent bioprobes for cellular imaging applications.
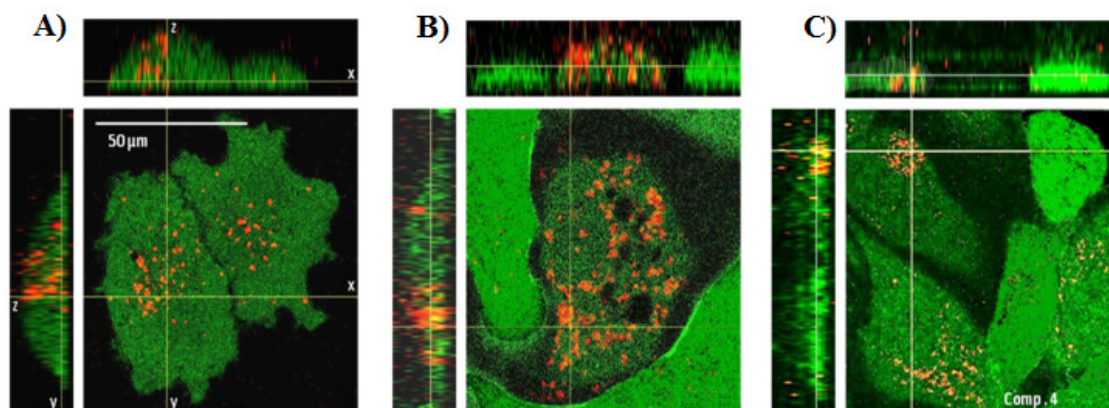
Figure 4.28. Confocal laser scanning microscopy images, including orthogonal views, left and top rectangular panels, of PC3 cell lines after an overnight incubation with the TPE nanoparticles (10 μM) of the conjugates A) **4,** B) **5** and C) **6**.

4.4. CONCLUSION

We have synthesized three tetraphenylethene-benzothiazole based donor-acceptor systems **4-6**, which have coupled effects of aggregation induced emission (AIE) and intramolecular charge transfer (ICT) mechanisms. The acetonitrile solutions of **4-6** were found to be less-emissive but upon addition of varying amounts of water to these solutions led the formation of their aggregates, having significant fluorescence emission. These molecules, owing to their unique self-assembling properties, formed supramolecular structures of different sizes, shapes, such as nanorods as well as nanoflowers. For example, the alkylated TPE derivatives, **4** and **5** formed the ordered nanorods, while the non-alkylated system **6** showed nanoflowers morphology in water/acetonitrile mixtures of *ca.* 70%, 50% and 95%, respectively. At *ca.* 99% of water, these TPE derivatives showed the formation of

NIR emitting fluorescent nanoparticles (NPs). These biocompatible NIR emitting NPs showed strong emission efficiency, large stokes shift, good stability and biocompatibility in the aqueous media as well as efficient cellular uptake mechanism. Thus these studies confirm that the D-A conjugates based on tetraphenylethene-benzothiazole systems act as AIE-active, biocompatible, NPs-based probes for fluorescence cellular imaging and diagnostics applications.

4.5. EXPERIMENTAL SECTION

4.5.1. General Techniques

All melting points were uncorrected and were determined on a Mel-Temp II melting point apparatus. The electronic absorption spectra were recorded on a Shimadzu UV-3101PC UV-VIS-NIR scanning spectrophotometer. The fluorescence spectra were recorded on a SPEX-Fluorolog F112X spectrofluorimeter. ^{1}H and ^{13}C NMR were recorded on a 500 MHz Bruker advanced DPX spectrometer. The mass spectra were recorded on a Thermo Scientific Exactive ESI-MS spectrophotometer. Fluorescence quantum yields of various conjugates were determined using tetraphenylporphyrin (TPP) as the reference compound (Φ_s = 0.11 in toluene).[23] Fluorescence quantum yields of the samples, Φ_f were caluculated by Eq 4.1,

$$\Phi_f = \frac{A_s\, F_u\, n_u^{\,2}}{A_u\, F_s\, n_s^{\,2}}\, \Phi_s \qquad \text{(Eq. 4.1)}$$

wherein, A_s and A_u are the absorbance of standard and unknown, respectively. F_s and F_u are the areas of fluorescence peaks of the standard and unknown and n_s and n_u

are the refractive indices of the solvents used for the standard and unknown, respectively.

Fluorescence lifetimes were measured using IBH (FluoroCube) time-correlated picosecond single photon counting (TCSPC) system. The samples were excited with a pulsed diode laser (<100 ps pulse duration) at a wavelength of 440 nm (NanoLED-11) with a repetition rate of 1 MHz. The detection system consisted of a microchannel plate photomultiplier (5000U-09B, Hamamatsu) with a 38.6 ps response time coupled to a monochromator (5000M) and TCSPC electronics [data station Hub including Hub-NL, NanoLED controller, and preinstalled fluorescence measurements and analysis studio (FMAS) software]. The fluorescence decay profiles were deconvoluted using IBH data station software V2.1 and minimizing the χ^2 values of the fit to 1 ± 0.1. Double-distilled water and dry acetonitrile were used for the studies. Imaging studies were carried out using Leica 3000 fluorescence and Nikon A1R confocal microscopes. Flow cytommetric analysis was carried out in a BD FACS Aria 2 machine. All experiments were carried out at room temperature (25 ± 1^{0}C), unless otherwise mentioned. The X-ray diffractograms of the samples were recorded on a Phillips diffractometer using Ni-filtered Cu Kα radiation.

4.5.1.1. Transmission Electron Microscopy (TEM). The TEM analysis was performed on JEOL 100 kV high resolution transmission electron microscope. The TPE conjugates **4-6** (3 mM) were dissolved in acetonitrile to prepare the stock solution. Then by increasing the water percentages of 10 μM acetonitrile solution upto 99%, we have drop casted on the top of carbon-coated Cu grid. The grids were

mounted on reverse tweezers and the samples were dried by a vacuum pump under reduced pressure for 1 h at room temperature. The accelerating voltage of the transmission electron microscope was 100 kV and the beam current was 65 A. Samples were imaged using a Hamamatsu ORCA CCD camera.

4.5.1.2. Scanning Electron Microscopy (SEM). The SEM studies were carried out using ZEISS EVO MA and LS series scanning electron microscope. The operating range was between 100-230 V at 50-60 Hz single phase with a consumption of 2.5 kVA. TPE conjugates **4-6** (3 x 10^{-3} M) were dissolved in acetonitrile to prepare the stock solution. Then by increasing different water percentages of 10 μM acetonitrile solution upto 99%, drop casted directly on the top of the aluminium grid and the solvents were allowed to evaporate at ambient conditions. The obtained sample was coated with gold in order to attain the easy passage flow of electrons.

4.5.1.3. Dynamic Light Scattering (DLS). The DLS of the TPE-benzothiazole conjugates were carried out on a Nano Zeta Sizer, Malvern instruments. The samples were prepared in different water/acetonitrile mixtures at a concentration of 5x 10^{-5} M. The light scattering experiments were performed under low polydispersity index by using glass cuvettes. The hydrodynamic diameters and polydisperse indices of the vesicles were determined using a Malvern Zeta Nano-ZS system.

4.5.1.4. Optical Polarized Microcopy (OPM). Optical Polarized Microcopy was performed using NikonHFX35A Optiphot-2 polarized-light optical microscope. For this analysis, the samples were prepared in various water/acetonitrile mixtures

at a concentration of 1 x 10^{-5} M. We drop casted the samples on a fresh glass plates and evaporate at ambient conditions with an excitation wave length of 340 nm. The images were taken using a CCD camera attached to NikonHFX35A.

4.5.1.5. Determination of Cellular Cytotoxicity. 3-(4,5-Dimethyl-thiazol-2-yl)-2,5-diphenyltetrazolium bromide (MTT) assay is a standard colorimetric assay for measuring cellular proliferation (cell growth). PC-3 cells (5 x 103 cells per well) were added to wells of two 96 well microliter plate with 150 μL Dulbecco's Modified Eagle Medium (DMEM) with 10% serum and incubated for 24 h. **4-6** (1-50 μM) were added in serial dilution (stock 100 mM diluted using DMEM for test, 1 % for control and incubated for 1 h. After 24 h of incubation, removed the plates from the incubator and added 10 μL of MTT (5mg/mL stock) to each well of the plate. After 4 h, carefully removed the supernatant without removing the formazan crystals formed. 100 μL of isopropyl alcohol was added to each well and covered the plates with aluminium foil and kept on a shaker until crystals were dissolved. The absorbance at 570 nm was measured in each well plate. The percentage growth inhibition was calculated as % Growth inhibition = (control-test)/control) × 100.
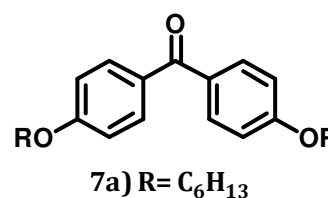
4.5.2. Materials

4, 4'-Dihydroxybenzophenone, 4-bromobenzophenone, 1-bromohexane, 1-bromododecane, 2-methylbenzothiazole, 1, 4-butane sultone, $TiCl_4$ and n-BuLi were purchased from Sigma Aldrich and S. D. Fine Chemicals, India and used as received without further purification.

4.5.2.1. General procedure for the synthesis of 7a and 7b. A mixture of 4, 4'-dihydroxybenzophenone (1 mmol), and 1-bromohexane or 1-bromododecane (5 mmol), and K_2CO_3 (10 mmol) in anhydrous DMF (20 mL) was stirred under N_2 atmosphere at 80 °C for 24 h. The reaction mixture was refluxed for 24 h and after cooling to room temperature the precipitated product was filtered. It was purified by re-crystallization from hexane to yield the derivatives **7a** or **7b**.

7a (96%): mp 82-83 °C; ^{1}H NMR (CDCl$_3$, 500 MHz) δ0.9 (m, 6H), 1.3 (m, 6H), 1.5 (m, 4H), 1.8 (m, 4H), 4.0 (t, 4H, *J*= 7.4 Hz), 6.9 (d, 4H, *J* = 8.5 Hz), 7.7 (d, 4H, *J* = 8.5 Hz); ^{13}C NMR (CDCl$_3$, 125 MHz) δ 14.7, 22.7, 24.2, 32.1, 65.7, 114.4, 119.2, 130.4, 132.1, 164.3, 190.1; HRMS (FAB) *m/z* Calcd for $C_{25}H_{34}O_3$: 382.25, Found 383.25 [M+1]$^+$.

7a) R= C_6H_{13}

7b (97%): mp 110-113 °C; ^{1}H NMR (CDCl$_3$, 500 MHz) δ 0.8 (m, 6H), 1.1 (m, 12H), 1.2 (m, 16H), 1.3 (m, 4H), 1.6 (m, 4H), 1.8 (m, 4H), 4.1 (t, 4H, *J*= 7.4 Hz), 6.9 (d, 4H, *J* = 8.4 Hz), 7.8 (d, 4H, *J* = 8.5 Hz); ^{13}C NMR (CDCl$_3$, 125 MHz) δ 14.1, 29.7, 28.2, 33.4, 68.7, 114.4, 117.2, 131.2, 132.1, 163.2, 191.1; HRMS (FAB) *m/z* Calcd for $C_{37}H_{58}O_3$: 550.43, Found 550.42 [M$^+$].
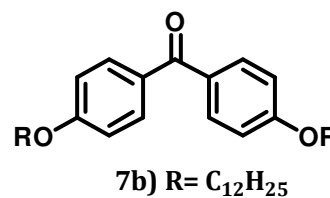
7b) R= $C_{12}H_{25}$

4.5.2.2. Synthesis of N-sulphobutyl- 2-methyl-1, 3 benzothiazole. A mixture of 2-methyl-1,3 benzothiazole (3.62 mmol) and 1,4 butanesultone (20.5 mmol) were heated in a pressure tube at 120 °C for 24 h. The solid obtained was washed thoroughly with diethyl ether and then with acetone. Repeated precipitation

from methanol using acetone yielded 880 mg (59%) of the

product, which was kept under vacuum and used for the next
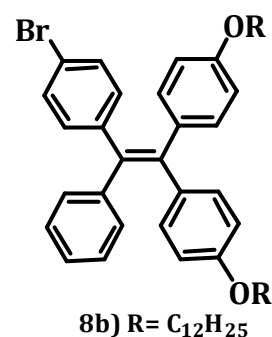
step without further purification.
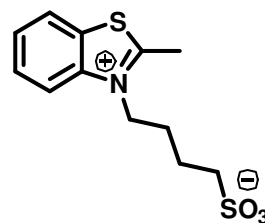
Yield, 59%, ; ^{1}H NMR (D$_2$O, 500 MHz) δ 8.47 (s, 1H), 8.09 (d,

1H, *J* = 8.5 Hz), 7.80-7.82 (d, 1H, *J* = 8.5 Hz), 4.62 (t, 2H, *J*= 7.4 Hz), 3.06 (s, 3H), 2.86-

2.89 (t, 2H, *J*= 7.4 Hz), 1.77-1.81 (m, 4H); ^{13}C NMR (D$_2$O, 125 MHz) δ 180.1, 141.4,

134.7, 132.3, 131.2, 129.7, 119.6, 58.6, 44.3, 34.2, 28.2, 19.8, 10.1; HRMS (FAB) *m/z*

Calcd for C$_{12}$H$_{15}$NO$_3$S$_2$: 285.04, Found 285.02 [M$^+$].

4.5.2.3. General procedure for the synthesis of 8a-c. TiCl$_4$ (13 mmol) was

added drop-wise to a stirred suspension of Zn powder (30 mmol) in dry THF (30

mL), under argon atmosphere at -10 °C, and the reaction was refluxed for 2 h. A

solution of compounds **7a-c** (3.3 mmol) and 4-bromobenzophenone (5 mmol) in

THF (65 mL) was added to the suspension of the titanium reagent, and the reaction

was continued at reflux for 12 h. The reaction mixture was cooled to 25 °C, poured

into a 10% aqueous K$_2$CO$_3$ solution (100 mL), and after vigorous stirring for 5.0 min,

the dispersed insoluble material was removed by filtration using a celite column.

The organic layer was separated, and the aqueous layer was extracted with CH$_2$Cl$_2$

(3×50 mL). The combined organic fractions were washed with water and dried with

Na$_2$SO$_4$. The crude product obtained after the removal of the solvent was purified by

column chromatography over silica and elution with petroleum ether gave the cross

coupled product **8a-c** in 10-12% yields.

8a (10%): mp 110-112 °C; ^{1}H NMR (500 MHz, CDCl$_3$): δ 0.9 (m, 6H), 1.2 (m, 8H), 1.34 (m, 4H), 1.72 (m, 4H), 3.86 (m, 4H), 6.62 (d, 2H, J = 8.5 Hz), 6.65 (d, 2H, J = 8.4 Hz), 6.84-6.96 (m, 5H), 6.97-7.04 (m, 2H), 7.05- 7.13 (m, 4H), 7.21 (d, 2H, J = 8.4 Hz); ^{13}C NMR (CDCl$_3$, 125 MHz) δ 14.1, 22.61, 25.7, 29.2, 31.61, 57.8, 77.3, 113.2, 114.4, 119.9, 127.8, 129.7, 130.8, 132.5, 135.7, 140.9, 143.9; HRMS (FAB) *m/z* Calcd for m/z C$_{38}$H$_{43}$BrO$_2$: 610.24, Found 610.39 [M$^+$].
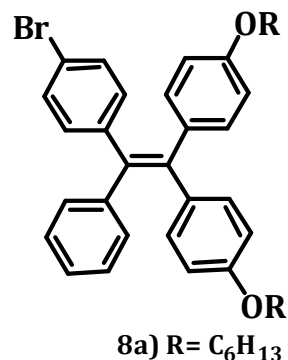
8b (12%): mp 130-131 °C; ^{1}H NMR (500 MHz, CDCl$_3$): δ 0.86-0.89 (m, 6H), 1.26-1.29 (m, 32H), 1.29-1.44 (m, 4H), 1.71-1.75 (m, 4H), 3.84-3.89 (m, 4H), 6.62 (d, 2H, J = 8.4 Hz), 6.65 (d, 2H, J = 8 Hz), 6.88-6.91 (m, 5H), 6.97-7.04 (m, 2H), 7.05-7.08 (m, 4H), 7.1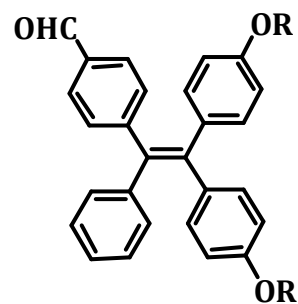1 (d, 2H, J = 8.5 Hz); ^{13}C NMR (CDCl$_3$, 125 MHz) δ 14.1, 22.7, 25.7, 26.0, 26.1, 29.5, 29.6, 29.3, 29.4, 31.9, 67.8, 77.2, 113.5, 113.7, 119.6, 127.7, 128.1, 128.5, 130.8, 132.4, 135.8, 140.9, 143.4, 157.7; ESI-MS m/z Calcd for C$_{50}$H$_{67}$BrO$_2$: 778.43, Found 779.64 (M + H)$^+$.

8c (12%): mp 150-151 °C; ^{1}H NMR (500 MHz, CDCl$_3$): δ 6.87-6.89 (d, 2H, *J* = 8.4 Hz), 6.99 -7.03 (m, 12H), 7.08-7.12 (m, 3H), 7.2 (d, 2H, *J* = 8.4 Hz); ^{13}C NMR (CDCl$_3$, 125 MHz) δ 120.6, 127.7, 142.2, 128.4, 131.4, 139.4, 140.4; ESI-MS m/z Calcd for C$_{26}$H$_{19}$Br: 410.1, Found 411.4 (M + H)$^+$.
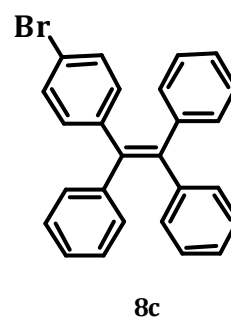
4.5.2.4. General procedure for the synthesis of 9a-c. The bromo derivatives **8a-c** were converted into their corresponding aldehydes by the formylation reaction. n-BuLi (1.6 M in hexane, 4.86 mmol) was added drop-wise to a solution of **8a-c** (2.43 mmol) in THF (15 mL) at -78 °C under argon atmosphere. After stirring for 4 h at the same temperature, dried DMF (14.56 mmol) was added quickly. The reaction mixture was allowed to rise to room temperature and stirred for 12 h before pouring into water. The product was extracted with dichloromethane (2×15 mL). The organic layer was subsequently washed with water (5 mL), brine (2 mL) and dried over anhydrous Na_2SO_4. The crude product was purified by column chromatography (silica gel/ethyl acetate: petroleum ether 5:95) to afford **9a-c** in 38-42% yields.

9a (40%): mp 161-162 °C; ^{1}H NMR (500 MHz, CDCl$_3$), δ 0.85-0.99 (m, 6H), 1.2 (m, 26H), 1.71-1.74 (m, 4H), 2.17-2.28 (m, 4H), 3.85-3.87 (m, 4H), 6.62 (d, 2H, *J* = 8.4 Hz), 6.65 (d, 2H, *J* = 8.4 Hz), 6.84-6.96 (m, 5H), 7.04-6.97 (m, 2H), 7.41-7.58 (m, 4H), 7.6 (d, 2H, *J* = 8.4 Hz), 9.87 (s, 1H); ^{13}C NMR (CDCl$_3$, 125 MHz) δ 14.0, 22.5, 25.7, 29.2, 31.6, 67.7, 77.1, 113.5, 113.7, 191.9, 127.8, 128.1, 129.2, 131.3, 132.6, 133.9, 135.4, 137.7, 142.5, 143.6, 158.2; ESI-MS m/z Calcd for $C_{39}H_{44}O_3$: 560.33, Found 561.33. (M + H)$^+$.


9a) R= C_6H_{13}

9b (42%): mp 170-171 °C; ^{1}H NMR (500 MHz, CDCl$_3$), δ 0.86-0.89 (m, 6H), 1.09-1.10 (m, 32H), 1.29-1.54 (m, 4H), 1.60-1.66 (m, 4H), 3.85-3.87 (m, 4H), 6.62 (d, 2H, *J* = 8.4 Hz), 6.5-6.84 (m, 5H), 6.69 (d, 2H, *J* = 8.4 Hz), 7 (m, 2H), 7.31-7.42 (m, 4H), 7.61 (d, 2H, *J* = 8.4 Hz), 9.98 (s, 1H); ^{13}C NMR (CDCl$_3$, 125 MHz) δ 14.1, 22.7, 26.1, 29.3, 29.4, 29.6, 31.9, 67.8, 77.3, 113.5, 113.7, 127.9, 129.2, 131.3, 132.0, 132.6, 133.9, 135.3, 137.7, 135.4, 142.4, 143.6, 151.4, 158.2, 191.9; ESI-MS m/z Calcd for C$_{51}$H$_{68}$O$_3$: 728.51, Found 729.52 (M + H)$^+$.
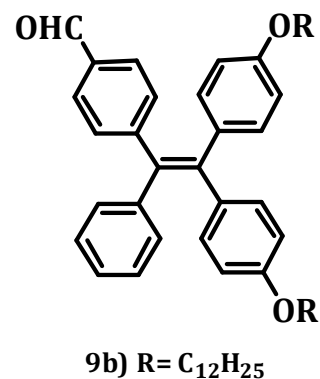
9c (38%): mp 156-157 °C; ^{1}H NMR (500 MHz, CDCl$_3$), δ 6.99 (m, 6H), 7.1 (m, 9H), 7.2 (d, 2H, *J* = 8.4 Hz), 7.61 (d, 2H, *J* = 8.4 Hz), 9.87 (s, 1H); ^{13}C NMR (CDCl$_3$, 125 MHz) δ 126.8, 126.6, 127.7, 129.1, 129.2, 131.1, 131.2, 131.9, 134.8, 139.7, 142.9, 143.2, 151.3, 191.9; ESI-MS m/z Calcd for C$_{27}$H$_{20}$O: 360.15, Found 361.15. (M + H)$^+$.
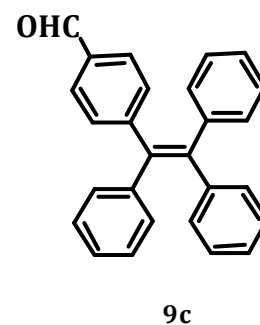
4.5.2.4. General procedure for the synthesis of the conjugates 4-6, Synthesis of the TPE-benzothiazole derivatives, **4**, **5** and **6** was achieved by the reaction of **9a-c** with N-sulphobutyl-2-methyl-1,3-benzothiazole in ethanol at 80 °C under argon atmosphere for 12 h. After cooling to room temperature, the solvent was evaporated under reduced pressure. The residue thus obtained was purified by

a silica gel column chromatography using methanol and chloroform mixture (5:95) as eluent to give **4-6** in 89- 92% yields.

4 (89%): mp 220-222 °C; ^{1}H NMR (500 MHz, CDCl$_3$), δ 0.85-0.89 (m, 6H), 1.37-1.41 (m, 24H), 1.68-1.76 (m, 4H), 2.11-2.64 (m, 10H), 3.0 (m, 2H), 3.85-3.88 (m, 2H), 5.11 (m, 2H), 6.21-6.61 (d, 4H, *J*= 8.4 Hz), 6.4 (d, 3H, *J* = 8.4 Hz), 6.43-6.54 (q, 4H), 7.0-7.14 (m, 3H, *J* = 8.4 Hz), 7.15 (d,
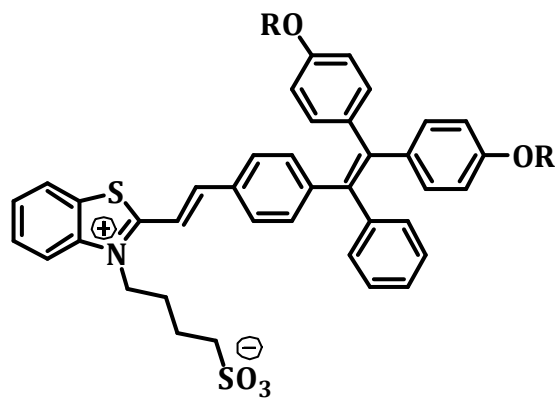
4) R= C$_6$H$_{13}$

2H, *J* = 8.4 Hz), 7.5-7.52 (m, 4H), 7.65 (t, 1H, *J* = 7.4 Hz), 7.88 (d, 1H, *J* = 8.5 Hz), 8.11 (d, 1H, *J* = 8.5 Hz), 8.54 (d, 1H, *J* = 15.5 Hz); ^{13}C NMR (CDCl$_3$, 125 MHz) δ 14.12, 22.2, 26.1, 29.6, 31.9, 56.7, 67.8, 114.3, 122.2, 124.6, 125.3, 127.7, 129.3, 131.3, 133.7, 139.2, 140.9, 162.5, 172.2; ESI-MS m/z Calcd for C$_{51}$H$_{57}$NO$_5$S$_2$: 827.35, Found 828.41 (M + H)$^+$.

5 (91%): mp 240-241 °C; ^{1}H NMR (500 MHz, CDCl$_3$), δ 0.84-0.89 (m, 6H), 1.37-1.41 (m, 32H), 1.67-1.75 (m, 4H), 2.11-2.16 (m, 10H), 2.99 (m, 2H), 3.84-3.88 (m, 2H), 5.1 (m, 2H), 6.61-6.64 (d, 4H, *J*= 8.4 Hz), 6.89-6.94 (q, 4H), 6.98 (d, 3H, *J* = 8.4 Hz), 7.08-7.10 (m, 3H, *J* = 8.4 Hz), 7.15 (d, 2H, *J* = 8.4
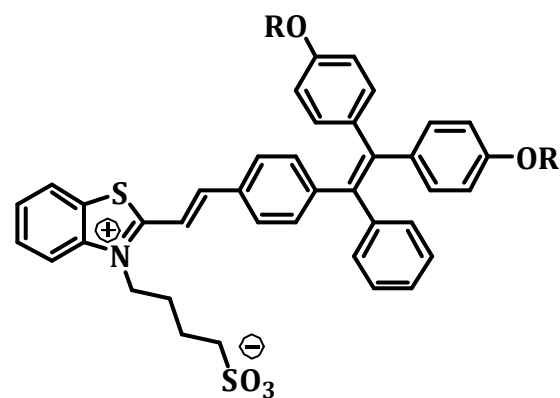
5) R= C$_{12}$H$_{25}$

Hz), 7.60–7.70 (m, 4H), 7.77 (t, 1H, *J* = 7.4 Hz), 7.98 (d, 1H, *J* = 8.5 Hz), 8.12 (d, 1H, *J* =

8.5 Hz), 8.26 (d, 1H, *J* = 15.5 Hz); ^{13}C NMR (CDCl$_3$, 125 MHz) δ 14.12, 22.3, 22.6, 26.0, 27.4, 29.6, 31.9, 56.7, 67.8, 113.5, 113.7, 116.8, 126.6, 127.4, 127.9, 128.5, 130.39, 131.1, 132.6, 135.5, 138.2, 142.6, 150.6, 158.0, 141.3, 171.3; ESI-MS m/z Calcd for C$_{63}$H$_{81}$NO$_5$S$_2$: 995.55, Found 996.56 (M + H)[+].

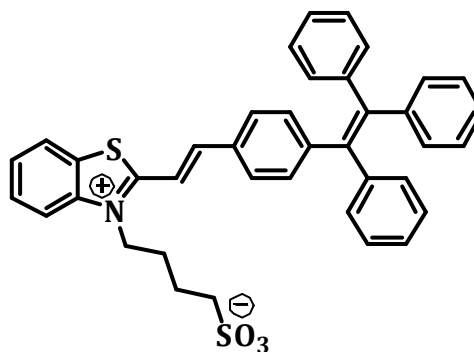**6** (92%): mp 210-211 °C; ^{1}H NMR (500 MHz, CDCl$_3$), 1.96-1.99 (t, 2H, *J*= 7.4 Hz), 2.18-2.15 (t, 2H, *J*= 6.4 Hz), 2.92-2.89 (t, 2H, *J*= 6.4 Hz), 3.3-3.82 (m, 2H), 4.93 (m, 2H), 6.96 (m, 6H), 7.00-7.18 (m, 11H), 7.73-7.9 (m, 4H), 7.94 (d, 1H, *J* = 16 Hz), 8.13 (d, 1H, *J* = 15.5 Hz), 8.2 (d, *J* = 8.4 Hz, 1H), 8.4 (d, 1H, *J* = 8.0 Hz); ^{13}C NMR (CDCl$_3$, 125 MHz) δ 14.12, 22.6, 26.0, 27.4, 31.9, 113.5, 113.7, 128.5, 130.4, 131.2, 131.6, 134.2, 139.3, 140.2, 141.2, 142.5, 147.2, 147.5, 172.3; and; ESI-MS m/z Calcd for C$_{39}$H$_{33}$NO$_3$S$_2$: 627.19, Found 628.19 (M + H)[+].

6

4.6. REFERENCES

1.   a) H. Yuning, J. W. Y. Lama and B. Z. Tang, *Chem. Commun.*, **2009**, 4332; b) N. Zhao, J. W. Y. Lam, H. H. Y. Sung, H. M. Su, I. D. Williams, K. S. Wong and B. Z. Tang, *Chem. Eur. J.*, **2013**, *19*, 1.

2.   a) W. Qin , K. Li , G. Feng , M. Li , Z. Yang , B. Liu and B. Z. Tang, *Adv. Funct. Mater.,* **2014**, *24*, 635; b) M. Shimizu, T. Hiyama, *Chem. Asian J.*, **2010**, *5*, 1516.

3.   a) Y. Hong, J. W. Y. Lam and B. Z. Tang, *Chem. Commun.*, **2009**, 4332; b) Z. Zhao, Z. Wang, P. Lu, C. Y. K. Chan, D. Liu, J. W. Y. Lam, H. H. Y. Sung, I. D. Williams, Y. Ma and B. Z. Tang, *Angew. Chem., Int. Ed.*, **2009**, *48*, 7608.

4.   Z. Zhao, S. Chen, X. Shen, F. Mahtab, Y. Yu, P. Lu, J. W. Y. Lam, H. S. Kwok and B. Z. Tang, *Chem. Commun.*, **2010**, *46*, 686.

5.   a) V. S. Vyas and R. Rathore, *Chem. Commun.*, **2010**, *46*, 1065; b) W. Wang, T. Lin, M. Wang, T.-X. Liu, L. Ren, D. Chen and S. Huang, *J. Phys. Chem. B*, **2010**, *114*, 5983.

6.   T. Noguchi, T. Shiraki, A. Dawn, Y. Tsuchiya, L. T. Ngoc Lien, T. Yamamoto and S. Shinkai, *Chem. Commun.*, **2012**, *48*, 8090.

7.   a) Z. Zhao, S. Chen, X. Shen, F. Mahtab, Y. Yu, P. Lu, J. W. Y. Lam, H. S. Kwok and B. Z. Tang, *Chem. Commun.*, **2010**, *46*, 686; b) Z. Zhao, J. W. Y. Lam and B. Z. Tang, *Curr. Org. Chem.*, **2010**, *14*, 2109; c) J. Huang, X. Yang, J. Wang, C. Zhong, L. Wang, J. Qin and Z. Li, *J. Mater. Chem.*, **2012**, *22*, 2478.

8.   a) S. Sharafy and K. A. Muszkat, *J. Am. Chem. Soc.*, **1971**, *93*, 4119; b) D. A. Shultz and M. A. Fox, *J. Am. Chem. Soc.*, **1989**, *111*, 6311.

9.   a) Z. Zhao, S. Chen, J. W. Y. Lam, C. K. W. Jim, C. Y. K. Chan, Z. Wang, P. Lu, H. S. Kwok, Y. Ma and B. Z. Tang, *J. Phys. Chem. C*, **2010**, *114*, 7963; b) Z. Zhao, P. Lu, J. W. Y. Lam, Z. Wang, C. Y. K. Chan, H. H. Y. Sung, I. D. Williams, Y. Ma and B. Z. Tang, *Chem. Sci.*, **2011**, *2*, 672.

10.   a) W. Z. Yuan, P. Lu, S. M. Chen, J. W. Y. Lam, Z. M. Wang, Y. Liu, H. S. Kwok, Y. G. Ma and B. Z. Tang, *Adv. Mater.*, **2010**, *22*, 2159; b) Z. J. Zhao, S. M. Chen, J. W. Y.

Lam, P. Lu, Y. C. Zhong, K. S. Wong, H. S. Kwok and B. Z. Tang, *Chem. Commun.*, **2010**, *46*, 2221.

11.   a) D. W. Domaille, E. L. Que and C. J. Chang, *Nat. Chem. Biol.*, **2008**, *4*, 168; b) M. H. Lim and S. J. Lippard, *Acc. Chem. Res.*, **2007**, *40*, 41.

12.   a) Y. Dong, J. W. Y. Lam, A. Qin, J. Liu, Z. Li, B. Z. Tang, J. Sun and H. S. Kwok, *Appl. Phys. Lett.*, **2007**, *91*, 111; b) L. Liu, G. Zhang, J. Xiang, D. Zhang and D. Zhu, *Org. Lett.*, **2008**, *10*, 4581.

13.   a) M. R. Bryce, *Adv. Mater.*, **1999**, *11*, 11; b) Z. R. Grabowski and K. Rotkiewicz, *Chem. Rev.* **2003**, *103*, 3899.

14.   a) W. Z. Yuan, Y. Gong, S. Chen, X. Yuan Shen, J. W. Y. Lam, P. Lu, Y. Lu, Z. Wang, R. Hu, N. Xie, H. S. Kwok, Y. Zhang, J. Zhi Sun, and B. Z. Tang, *Chem. Mater.* **2012**, *24*, 1518; b) M. R. Bryce, *Adv. Mater.*,**1999**, *11*, 11.

15.   E. L. Que, D. W. Domaille, and C. J. Chang , *Chem. Rev.*, **2008**, *108*, 1517.

16.   a) X. H. Gao, Y. Y. Cui, R. M. Levenson, L. W. K. Chung and S. M. Nie, *Nat. Biotechnol.*, **2004**, *22*, 969; b) C. Li, J. S. Xia, X. B. Wei, H. H. Yan, Z. Si, S. H. Ju, *Adv. Funct. Mater.*, **2010**, *20*, 2222.

17.   C. K. Lim, S. Kim, I. C. Kwon, C. H. Ahn and S. Y. Park, *Chem. Mater.*, **2009**, *21*, 5819; b) B. Law and C. H. Tung, *Bioconjugate Chem.* **2009**, *20*, 1683; c) K. Y. Pu, K. Li and B. Liu, *Adv. Funct. Mater.*, **2010**, *20*, 2770; d) D. Ding, K. Li, Z. S. Zhu, K. Y. Pu, Y. Hu, X. Q. Jiang and B. Liu, *Nanoscale,* **2011**, *3*, 1997.

18.   K. Yang , S. Zhang, G. X. Zhang, X. M. Sun, S. T. Lee and Z. Liu, *Nano Lett.*, **2010**, *10* ,3318.

19.   X. K. Shu, A. Royant, M. Z. Lin, T. A. Aguilera, V. L. Ram, P. A. Steinbach and R. Y. Tsien, *Science*, **2009**, *324*, 804.

20.   a) U. R. Genger, M. Grabolle, S. C. Jaricot, R. Nitschke and T. Nann, *Nat. Methods*., **2008**, *5*, 763; b) K. Li , J. Pan, S. S. Feng, A. W. Wu, K. Y. Pu, Y. T. Liu and B. Liu, *Adv. Funct. Mater*., **2009**, *19*, 3535.

21.   a) A. M. Derfus, W. C. W. Chan and S. N. Bhatia, *Nano Lett*., **2004**, *4*, 11; b) A. M. Smith, H. Duan, A. M. Mohs and S. Nie, *Adv. Drug Delivery Rev*., **2008**, *60*, 1226.

22.   a) C. A. Bertolino, G. Caputo, C. Barolo, G. Viscardi and S. Coluccia, *J. Fluoresc*., **2006**, *16*, 221.

23.   R. Varghese, V. K. Praveen, S. Mahesh and A. Ajayaghosh, *Angew. Chem*., *Int. Ed.,* **2006**, *45*, 3261.

LIST OF PUBLICATIONS

1. β-Cyclodextrin as a Photosensitizer Carrier: Effect on Photophysical Properties and Chemical Reactivity of Squaraine Dyes, K. T. Arun, **D. T. Jayaram**, R. R. Avirah, and D. Ramaiah, *J. Phys. Chem*. B, **2011**, *115*, 7122-7128.

2. Squaraine Dyes in PDT: From Basic Design to *In Vivo* Demonstration, R. R. Avirah, **D. T. Jayaram**, N. Adarsh and D. Ramaiah, *Org. Biomol. Chem*., **2012**, *10*, 911-920 *(Perspective Article and Listed in the Top 10 Most Cited Articles of the Journal)*.

3. Photomorphogenesis of γ-Globulin: Effect on Sequential Ordering and Knock Out of Gold Nanoparticles Array, **D. T. Jayaram**, B.H. Shankar and D. Ramaiah, *RSC Advances*, **2013**, *3*, 13463-13469.

4. A Reversible Dual Mode Chemodosimeter for the Detection of Cyanide Ions in Natural Source, B. H. Shankar, **D. T. Jayaram** and D. Ramaiah, *Chem. Asian J*., **2014**, *9*, 1636-1642.

5. Fluorescent Nanoparticles Based on TPE-Benzothiazole Conjugates as Efficient *In Vitro* Bioimaging Agents, **D. T. Jayaram**, S. Ramos, B. H. Shankar, C. Garrido, J. Blanco and D. Ramaiah, *J. Am. Chem. Soc*., **2014** (Communicated).

PAPERS PRESENTED IN CONFERENCES

6. Squaraine-based Protein PhotoScissors, **D. T. Jayaram**, R. Chowdhury, D.Ramaiah, and C. V. Kumar, A poster presented at the Indian Analytical Science Congress, Kanyakumari, Kerala, **2012**, February 26-27.

7. Photomorphogenesis of γ-Globulin: Effect on Sequential Ordering and Knock Out of Gold Nanoparticles Array, **D. T. Jayaram**, B. H. Shankar and D. Ramaiah, A poster presented at Indo-US Symposium on Molecular Materials, I.I.Sc., Banglore, Karnataka, **2013**, July 15-17.

8. Intriguing Fabrication of Array of Gold Nanoparticles: Effect of Self-Assembly of γ-Globulin on Sequential Ordering and Knock Out of Gold Nanoparticles Array, **D. T. Jayaram**, B. H. Shankar, M. Viji and D. Ramaiah, A poster presented at CRSI National Symposium in Chemistry, CSIR-NEIST, Jorhat, Assam, **2014**, July 10-12.

9. TPE-Benzothiazole Nanoconjugates: Photophysical, Self-Assembly and *In Vitro* Bio-Imaging Applications, **D. T. Jayaram**, B. H. Shankar, and D. Ramaiah, A poster presented at Asian Photochemistry International Symposium in Chemistry, Kovalam, Kerala, **2014**, November 10-13.